Josephson Junctions fabricated by Focused Ion Beam

Robert Hugh Hadfield

Trinity College

Cambridge

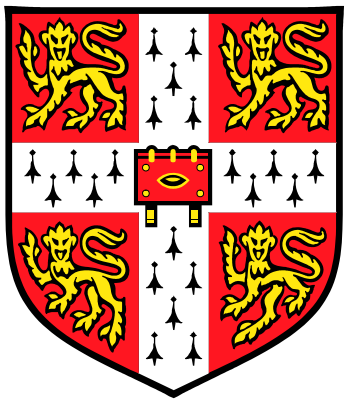

A Dissertation submitted for the Degree of

Doctor of Philosophy at the University of Cambridge

October 2002

Declaration

This dissertation is the result of my own work and includes nothing which is the outcome of work done in collaboration except where specifically indicated in the text. This work has been carried out in the Department of Materials Science and Metallurgy, University of Cambridge, U.K. since October 1999. No part of this dissertation has been submitted previously at Cambridge or any other university for a degree, diploma or other qualification. This dissertation does not exceed 60,000 words.

Robert Hadfield

21st October 2002

Foreword

This thesis gives an account of work I have carried out since October 1999 as a Ph.D. student in the Device Materials group at the Department of Materials Science and Metallurgy, University of Cambridge, U.K. I was first introduced to superconductivity as a final-year undergraduate in the Department of Physics in Cambridge. My final year project concerned 'the electromagnetic properties of grain boundary Josephson junctions in high temperature superconductors', supervised by Dr. Ed Tarte at the Interdisciplinary Research Centre in Superconductivity. After my graduation in June 1998 I was given the opportunity to spend a year in Germany as the holder of the Trinity College Exchange Studentship with the ‚Studienstiftung des deutschen Volkes'. I went to group of Professor Alex Braginski at Forschungszentrum Jülich, where I worked on the development of ramp-edge Josephson junctions in high temperature superconductors for Rapid Single Flux Quantum (RSFQ) logic applications. Although that particular project was not tremendously successful in terms of publishable results, it is largely as a result of experience gained during my time in Germany that I have been able to make good progress since my return to Cambridge.

I am very grateful to my supervisor, Mark Blamire, for his guidance and support - and for spurring me on to greater efforts. I am indebted to Wilfred Booij and Richard Moseley, who laid the foundations for this project. Throughout my Ph.D. research Gavin Burnell has been my main collaborator and source of practical assistance (without his programming skills the measurements presented here would scarcely have been possible). I am extremely grateful to him, and to Dae-Joon Kang, who has maintained the Focused Ion Beam system in the excellent condition required for high resolution work. My thanks also to Stephen Lloyd for his assistance in carrying out the very useful Transmission Electron Microscopy studies. I would like to thank Chris Bell for his enthusiasm and many stimulating discussions – and also Austen Lamacraft, who has been my main sparring partner (in physics) since my earliest years in Cambridge. I am very grateful indeed to Ed Tarte and Jan Evetts for indulging my tangential queries and allowing me access to their respective libraries. My research has benefited greatly from valuable discussions with a large number of other people in Cambridge and elsewhere (amongst others): Phil McBrien, James Ransley, David Moore, Ben Simons, Sam Benz, Paul Dresselhaus, Sasha Klushin, Alexey Ustinov, Simon Bending, Mac Beasley and John Martinis. The U.K. Engineering and Physical Sciences and Research Council (EPSRC) provided financial support for this project. I gratefully acknowledge additional support from the Trinity College Rouse Ball fund, EURESCO, the U.K. Institute of Physics and the Worshipful Company of Armourers and Braisers.

I thank the other members of the Device Materials group for contributing to a supportive working atmosphere and many memorable events over the past three years (in the face of stiff competition, I think Vassilka and Jose threw the best parties). My major source of recreation - and indeed inspiration - during my years as a research student has been Cambridge University Ultimate Frisbee Club ('Strange Blue' as the team is known). My Frisbee friends are too numerous to list and our deeds too glorious to do justice to here. Suffice it to say, when I was injured last winter (following my ill-advised overnight ascent of Mount Fuji), working successive weekends in the lab and supervising undergraduate physics wasn't any kind of substitute. Special thanks also to Andy and Alex for putting me up for the final month, when I had no place to live.

Finally I would like to thank to my parents Anne and Hugh, and my brothers Tom and Oliver for their love and support. I'd also like to thank Anna for making my last summer in Cambridge the happiest.

Robert Hadfield

Cambridge, October 2002

Abstract

This thesis details recent work on an innovative new approach to Josephson junction fabrication. These junctions are created in low T_C superconductor-normal metal bilayer tracks on a deep submicron scale using a Focused Ion Beam Microscope (FIB). The FIB is used to mill away a trench 50 nm wide in the upper layer of niobium superconductor (125 nm thick), weakening the superconducting coupling and resulting in a Josephson junction. With the aid of a newly developed *in situ* resistance measurement technique it is possible to determine the cut depth to a high degree of accuracy and hence gain insight into how this affects the resulting device parameters. Devices fabricated over a wide range of cut depths and copper normal metal layer thicknesses (0-175 nm) have been thoroughly characterized at 4.2 K in terms of current-voltage (*I-V*) characteristics, magnetic field- and microwave-response. In selected cases *I-V* characteristics have been studied over the full temperature range from T_C down to 300 mK. Devices with resistively-shunted (RSJ) *I-V* characteristics and I_CR_N products above 50 μV at 4.2 K have been fabricated reproducibly. This work has been complemented by Transmission Electron Microscopy (TEM) studies that have allowed the microstructure of the individual devices to be inspected and confirm the validity of the *in situ* resistance measurement.

The individual junction devices are promising candidates for use in the next generation of Josephson voltage standards. In collaboration with Dr. Sam Benz at the National Institute of Standards and Technology (NIST) in the U.S., series arrays of junctions have been fabricated and characterized. Phase-locking behaviour has been observed in arrays of 10 junctions of spacings 0.2 to 1.6 μm between 4.2 K and T_C in spite of the relatively large spread in individual critical currents. Strategies for minimizing junction parameter spread and producing large-scale arrays are discussed.

The opportunities offered by the FIB for the creation of novel device structures has not been overlooked. By milling a *circular* trench in the Nb Cu bilayer a Corbino geometry SNS junction is created. In this unique device the junction barrier is enclosed in a superconducting loop, implying that magnetic flux can only enter the barrier as quantized vorticies. This gives rise to a startling magnetic field response – with the entry of a vortex the critical current is suppressed from its maximum value to zero. Experimental results and theoretical modeling are reported. Possible future applications of this novel device geometry (which may be of relevance to Quantum Computing and to studies of Berry's phase effects) are considered.

Symbols and Abbreviations

Intended as a useful reference guide rather than an exhaustive list.

Physical Constants

Planck constant	$h = 6.626 \times 10^{-34}$ J s
Planck constant/2π	$\hbar = 1.055 \times 10^{-34}$
Electronic charge	$e = -1.602 \times 10^{-19}$ C
Permeability of free space	$\mu_0 = 4\pi \times 10^{-7}$ H m^{-1}
Magnetic flux quantum	$\Phi_0 = h/2e = 2.07 \times 10^{-17}$ Wb
Boltzmann Constant	$k_B = 1.381 \times 10^{-23}$ J K^{-1}

Superconductors:

T	temperature
T_C	transition temperature
$\underline{A}$	magnetic vector potential
$\underline{J}$	current density
Λ	London parameter
ξ	coherence length
ξ_{GL}	Ginzburg Landau coherence length
ξ_0	intrinsic coherence length
λ	magnetic penetration depth
λ_L	London penetration depth
λ_p	thin film penetration depth (perpendicular)
ρ	carrier density or resistivity
ψ	superconducting wavefunction
l	electronic mean free path
Δ	superconducting energy gap parameter
v_F	Fermi velocity
t	film thickness

Josephson Junctions:

I	current
V	voltage
φ	phase difference across Josephson junction
I_C	critical current
R_N	normal state resistance
$I_C R_N$	Characteristic voltage
J_n	n^{th} order Bessel function
d	trench width
L_{Eff}	effective junction barrier thickness
w	barrier width (transverse to current flow)
λ_J	Josephson penetration depth
ω_p	junction plasma frequency
Ω	reduced frequency

Abbreviations

BCS	Bardeen Cooper Schrieffer (theory)
FIB	focused ion beam
GBJ	grain boundary junction
HF	high frequency or hydrofluoric acid
NIST	National Institute of Standards and Technology (U.S.A.)
PSGE	perturbed sine-Gordon equation
RF	radio frequency
RIE	reactive ion etch
RSFQ	rapid single flux quantum (digital logic)
RSJ	resistively shunted junction
SEM	scanning electron microscope
SIS	superconductor-insulator-superconductor (junction)
SNS	superconductor-normal metal-superconductor (junction)
SQUID	superconducting quantum interference device
TDGL	time-dependant Ginzburg Landau (theory)
TEM	transmission electron microscopy
2DEG	two-dimensional electron gas
UHV	ultra high vacuum

Contents

Chapter 1: Introduction

The Josephson effect is the quantum mechanical tunneling of paired electrons between two regions of superconductor. So-called Josephson junctions exhibiting this striking phenomenon now form the basis of a number of technologies. For example, Superconducting Quantum Interference Devices (SQUIDs) are the world's most sensitive detectors of magnetic flux, capable of measuring the magnetic fields produced by a single living cell. Josephson junctions have formed the basis of the international standardization of the volt since the mid-1970's. In addition, Josephson junctions provide the active elements for ultrafast digital electronics and (potentially) for quantum computing. As in the case of conventional silicon-based (semiconductor) electronics, further miniaturization is a key research issue in superconducting electronics. Curious quantum-mechanical effects, which arise as we make the transition from microscopic (millionth of a metre) to nanoscale (thousand-millionth of a metre) components, present a further challenge - and motivation - to the researcher.

A reliable and versatile technique for the fabrication of nanoscale Josephson junctions in superconductor-normal metal bilayers has been developed. The fabrication technique depends on the use of a Focused Ion Beam microscope (FIB). This instrument is similar in operation to a Scanning Electron Microscope (SEM) in which a beam of high-energy electrons is focused onto the surface of a sample in vacuum. As the beam rasters back and forth across the surface, an image of nanoscale resolution can be built up using secondary electrons. In a FIB, in place of an electron beam, a beam of much more massive Gallium ions is used. In the first instance the sample can be imaged just as in the SEM. However, if the high-energy ion beam dwells on the sample for any appreciable time material is eroded (like nanoscale sandblasting). In the microelectronics industry the FIB has become an indispensable tool for sectioning and examining faulty microchips. The FIB our laboratory has been adapted for the manufacture of nanoscale electronic devices. In order to fabricate a superconductor-normal metal-superconductor (SNS) Josephson junction, a microscopic track is patterned by standard photolithography in a bilayer of niobium superconductor and copper normal metal. A narrow trench (50 nanometres wide) is milled in the upper superconducting layer. The result is a Josephson junction with a normal metal barrier. A specially constructed *in situ* resistance measurement stage allows the resistance of the track to be measured whilst the milling is taking place. With the use of a simple algorithm the resistance change can be converted to a milling depth, allowing the trench depth to be determined on the scale of nanometres (tens of atomic layers).

A thorough investigation has been carried out of the variation of junction properties with respect to trench depth and normal metal layer thickness. The resulting devices show considerable promise as the basis for the next generation of voltage standards arrays. In collaboration with U.S. National Institute of Standards and Technology (NIST), prototype series arrays of SNS junctions have been fabricated and characterized. The goal is to fabricate an array of closely spaced junctions with sufficiently small parameter spreads such that they respond to an applied microwave field in unison

This unique technology also allows novel device structures to be created and studied. Milling a circular trench in the superconductor-normal metal bilayer results in a Corbino geometry Josephson junction. This novel device can be measured by making an electrical contact to the central island. In the case of a Josephson junction, this geometry has some interesting implications that have not previously been explored in detail, either experimentally or theoretically. In thin film superconductors, magnetic flux can penetrate the superconducting state, but only as quantized vortices. In this geometry the Josephson junction is surrounded by a superconducting loop, so magnetic flux can only enter the junction in single quanta, leading to an abrupt suppression of the Josephson supercurrent. The study reported here opens up some intriguing future avenues of research.

The structure of this thesis can be summarized as follows: Chapter 2 provides an introduction to the field of superconductivity, with particular emphasis on aspects relevant to superconductor-normal metal-superconductor (SNS) junctions. There then follows in Chapter 3 a description of the device fabrication process and the measurement facilities used in this work. Chapter 4 contains a survey of previous approaches to junction fabrication in this geometry, followed by a discussion of the properties of the thin films used in device fabrication and finishing with the results of the TEM studies of device profiles. The measured properties of single SNS junctions are discussed in Chapter 5. The work on series arrays of nanofabricated SNS junctions carried out in collaboration with NIST is described in Chapter 6. The realization of a novel device geometry (the Corbino geometry SNS junction) is the subject of Chapter 7. Chapter 8 concludes the main body of the thesis. Extensions of the current work are also discussed. Finally there is a bibliography and two appendices; one listing scientific meetings attended by the author and the other purely theoretical. The majority of the work in this thesis has already been published (single junctions – Hadfield 2001; arrays – Hadfield 2002b; early Corbino junction results – Hadfield 2002a). The latest Corbino junction results have been submitted for publication in *Physical Review B* (Hadfield 2002b). Work contained in this thesis also features in a number of other publications to date (Burnell 2002a, 2002b).

Chapter 2: Weak Superconductivity

2.1 Introduction

The extraordinary phenomenon of superconductivity was discovered by Kammerlingh Onnes in 1911, shortly after he had succeeded in liquefying helium (Onnes 1911). The superconducting state is characterized not only by the disappearance of electrical resistivity below a critical temperature T_C, but also by the onset of perfect diamagnetism at this point - the Meissner effect (Meissner 1927). Superconductivity occurs in about half of the metals in the periodic table. The critical temperatures are all relatively low however – the highest T_C occurs in niobium at 9.25 K.

A number of recent historical reviews concerning the theoretical development of the subject are available (Schrieffer 1993, Schrieffer 1999, Ginzburg 2000). A robust phenomenological theory describing the basic effects of superconductivity was provided by the London brothers (London 1935, 1950). An important further contribution to the understanding of superconductivity was made by Ginzburg and Landau (Ginzburg 1950). However, a satisfactory microscopic theory was absent until that of Bardeen, Cooper and Schrieffer (BCS theory) was published in 1957 (Bardeen 1957). This paved the way for Josephson's 1962 prediction of tunneling between two weakly coupled superconductors (Josephson 1962) – the Josephson effect. The possibility of a Josephson junction-based computing technology spurred a major research effort in the 1960s and 1970s. This however was abandoned, largely due to the unparalleled success of competing silicon-based technologies (Keyes 1989).

Until the mid-1980's the record value of T_C stood at 23 K for Nb_3Ge (Gavaler 1973). The discovery of superconductivity at much higher temperatures in the cuprate materials by Bednorz and Müller in 1986 (Bednorz 1986) provoked great interest and has provided the stimulus for an immense research effort. At present a satisfactory theory encompassing all forms of superconductivity in the cuprates is lacking, and the formidable complexity of these materials has made it difficult to reap the predicted technological benefits of the higher critical temperature (present record: $HgBa_2Ca_2Cu_3O_{8+\delta}$, 134 K at atmospheric pressure (Schilling 1994); 164 K at high pressure (Gao 1994)). Due to the emergence of new Junction-based computing concepts such as Rapid-Single-Flux-Quantum Logic (RSFQ) (Likharev 1991) and Quantum Computing (Averin 1999, Nakamura 1999, Makhlin 2001) there is continued interest in viable junction technologies. In this area, as a result of ever improving refrigeration and nanofabrication techniques, low T_C junctions offer renewed promise.

2.2 The Superconducting State

This section gives overview of superconducting phenomenology and theoretical approaches that lead to the development of BCS theory, with particular emphasis on aspects relevant to this investigation.

2.2.1 The two-fluid model

Gorter and Casmir (Gorter 1934) first put forward the concept of a 'two-fluid model' of superconductivity in order to explain the second order phase transition occuring at T_C. They proposed that the total density of electrons ρ be divided into two components:

$$\rho = \rho_s + \rho_n , \tag{2.1}$$

where a fraction ρ_s/ρ of the electrons can be regarded as being condensed into a 'superfluid', which is primarily responsible for the remarkable properties of superconductors, whilst the remainder (the fraction ρ_n/ρ) form an interpenetrating 'normal' fluid , which carries entropy and is subject to scattering. The fraction ρ_s/ρ grows from zero at T_C to unity at T = 0 K, where all of the electrons have entered the superfluid condensate. This approach however offers no explanation of how the critical field of a superconductor (i.e. its diamagnetic response) changes with temperature.

2.2.2 The London theory

The London theory took perfect diamagnetism to be the most fundamental property of a superconductor, assuming some form of superfluid wavefunction that is rigid to the vorticity imparted by the magnetic field. Using Maxwell's equations and the two-fluid picture, dissipationless current flow followed directly, and the London brothers were able to show that magnetic flux must penetrate some distance into the bulk. The London penetration depth λ_L at T = 0 K is

$$\lambda_L(0) = \left(\frac{m_e}{\mu_0 \rho_s e^2} \right)^{1/2} \tag{2.2}$$

where m_e is the effective electron mass, μ_0 is the permeability of free space and e is the electronic charge. λ_L gives the *minimum* penetration depth that may be expected in practice (high frequency measurements typically give a superconducting penetration depth λ ~100 nm for a bulk metallic superconductor well below T_C).

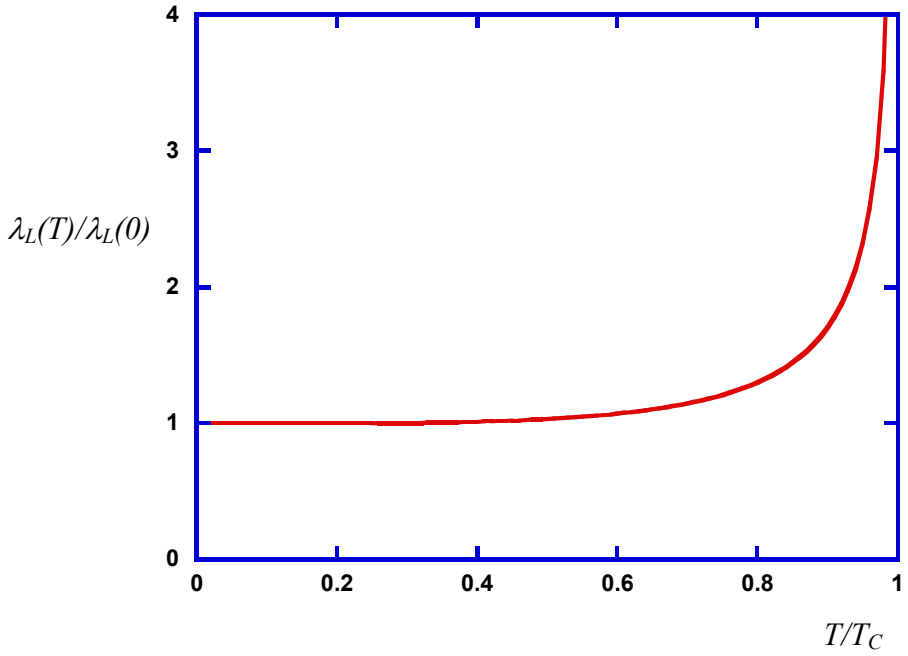

Figure 2.1: The temperature dependence of the London penetration depth λ_L according to (2.3).

The temperature dependence of λ_L is described by the formula

$$\lambda_L(T) = \lambda_L(0)\left[1-(T/T_C)^4\right]^{-1/2} \tag{2.3}$$

and is depicted in Figure 2.1. We see that λ_L is infinite at T_C , but differs from its $T = 0$ value $\lambda_L(0)$ by only a few percent at $T/T_C = 0.5$. This formula gives a good qualitative guide to the measured variation of λ with temperature.

In the London theory the phase of the wavefunction must be single-valued and this led to the prediction of *fluxoid quantization*. The fluxoid is the magnetic flux through an area *plus* a line integral around that area due to the superfluid velocity. In the case of a thick superconducting cylinder (much thicker than λ_L) this second term can be ignored and flux is also quantized. This effect was observed experimentally (Deaver 1961, Doll 1961), showing that quantization takes place in units of $\Phi_0 = h/2e = 2.07 \times 10^{-17}$ Wb. Hence the full expression for fluxoid quantization is

$$\oint\left(\underline{A}+\Lambda\underline{J}_S\right)\cdot d\underline{l} = \frac{h}{2e}n \tag{2.4}$$

where $\underline{A}$ is the magnetic vector potential, Λ is the London parameter and $\underline{J}_S$ is the screening current density. This provides strong evidence that the superfluid is comprised of *pairs* of

electrons. Direct evidence of fluxoid quantization was provided by the Little-Parks experiment (Little 1962, 1964), which was performed on a thin-walled superconducting cylinder.

As mentioned, in practice the measured penetration depth λ is greater than λ_L for materials with short electronic mean free paths. Pippard extended the London theory to include non-local electrodynamics (Pippard 1950). His key insight was to recognize that λ depends on the size of the electron mean free path l relative to an intrinsic coherence length ξ_0. The coherence length therefore determines the scale over which the wavefunction can 'feel' non-local electromagnetic fields. BCS microscopic theory (Section 2.2.4) gives the value

$$\xi_0 = 0.18\hbar v_F / k_B T_C \tag{2.5}$$

where v_F is the velocity of an electron at the Fermi surface. The numerical value is typically ~1 μm although v_F and T_C vary considerably in the various superconductors (van Duzer 1999). For a pure material with a large coherence length (l, $\xi_0 >> \lambda_L$ – the 'clean' limit)

$$\lambda = 0.65(\xi_0 / \lambda_L)^{1/3} \lambda_L \ . \tag{2.6}$$

In the 'dirty' limit ($l<\xi_0$)

$$\lambda \approx \lambda_L (\xi_0 / l)^{1/2} . \tag{2.7}$$

2.2.3 Ginzburg-Landau theory

Ginzburg and Landau (Ginzburg 1950) developed a theory to include a spatial variation of the superfluid density ρ_s. The Ginzburg-Landau theory was based on the Landau theory of second order phase transitions. A phenomenological Hamiltonian for the system can be written down, dependent only on the symmetries of the system, in terms of some order parameter. A form of the free energy of the system is used to find its generic behaviour near a transition. Applying this approach to the problem of superconductivity, they suggested that ρ_s / ρ be written in terms of a complex, position-dependent, condensate wavefunction $\psi(r)$, $\rho_s(r)/\rho = |\psi(r)|^2$. This wavefunction is used as the order parameter. The expression for the free energy f is then

$$f = f_n + \alpha |\psi|^2 + \beta |\psi|^4 + \varepsilon |(-i\hbar\nabla + e^* A)\psi|^2 , \tag{2.8}$$

where α, β and ε are phenomenological terms. Conventionally ε is taken as $1/2m_e$ and e^* is the effective charge (which turns out to be twice the electronic charge). Minimizing this over all space:

$$\frac{1}{2m_e}\left(-i\hbar\nabla + e^* A\right)^2 \psi + \left(\alpha + \beta|\psi|^2\right)\psi = 0\,. \tag{2.9}$$

With suitable boundary conditions the Ginzburg-Landau penetration depth (λ_{GL}) and coherence length (ξ_{GL}) can be derived:

$$\lambda_{GL} = \sqrt{m_e\beta / 4\mu_0 e^2|\alpha|} \tag{2.10}$$

$$\xi_{GL} = \sqrt{\hbar^2 / 2m_e|\alpha|} \tag{2.11}$$

The behaviour of f near T_C requires that α and β are temperature dependent. Now ξ_{GL} is not the same as the intrinsic coherence length ξ_0, but describes the length scale over which $\psi(r)$ varies. The ratio $\kappa = \lambda_{GL}(T)/\xi_{GL}(T)$ determines whether the material behaves as a Type I ($\kappa << 1/\sqrt{2}$) or Type II superconductor ($\kappa >> 1/\sqrt{2}$). Using the Ginzburg-Landau theory, Abrikosov showed that in the case of Type II superconductors, magnetic field entering the bulk at the critical field H_{C1} does so as quantized vortices (Abrikosov 1957). This is known as the *mixed state*. These vortices are characterized by a core of size ~ $\xi_{GL}(T)$ inside which the order parameter $\psi(r)$ and the superconducting properties are suppressed. This is surrounded by a circulating current which shields the flux line from the bulk, and extends a distance ~$\lambda_{GL}(T)$ from the centre of the core.

2.2.4 BCS theory

Bardeen, Cooper and Schrieffer succeeded in showing that the formation of a superfluid condensate of paired electrons is feasible (Bardeen 1957). The BCS model offers a microscopic description of the superconducting ground state, which has been applied with great success to low T_C materials. Below T_C the Coulomb repulsion between electrons at the Fermi surface is screened and a weak attraction sufficient to bind the pairs together arises due to interactions with vibrations of the atomic lattice (phonons). The resulting *Cooper pair* has zero net momentum and (in a conventional singlet s-wave superconductor) is comprised of electrons of opposite spins. A many-particle wavefunction was constructed to describe the superconducting state. From this it was shown that 2Δ is the energy required to split a Cooper

pair and that the size of a Cooper pair is given by the coherence length, ξ_0 (2.5). The BCS prediction for the temperature dependence of the gap parameter Δ is shown in Figure 2.2.

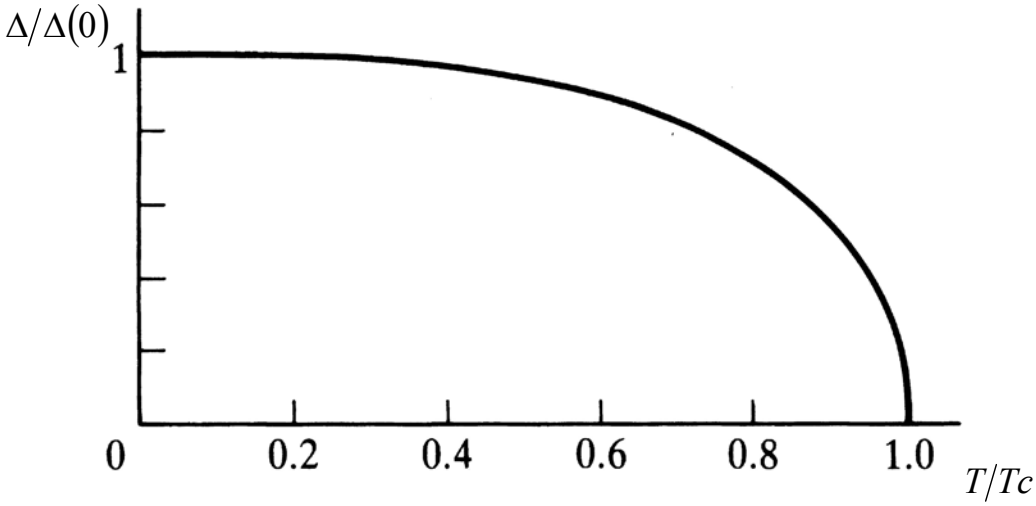

Figure 2.2: The BCS prediction of the temperature dependence of the gap parameter $\Delta(T)$ (Tinkham 1996).

Gor'kov (Gor'kov 1958) showed that the Ginzburg-Landau equations could be derived from BCS theory close to T_C and was thus able relate the wavefunction ψ to the gap parameter Δ. Hence a single wavefunction is associated with a macroscopic number of electrons which condense into the same quantum state forming Cooper pairs. Hence the superconducting state can be regarded as a macroscopic quantum state, described by a macroscopic wavefunction of the form

$$\psi = \sqrt{\rho_s}\, e^{i\theta}, \tag{2.12}$$

where θ is the phase common to all the Cooper pairs.

2.2.5 Flux penetration in superconducting thin films

If we consider the interface between a Type II superconductor and free space, it is well established experimentally that vortices experience a surface barrier impeding their entry into the bulk. Bean and Livingstone considered the penetration of straight flux lines through a perfectly flat surface (Bean 1964). This 'Bean-Livingstone' barrier arises due to the superposition of the attractive image force and the repulsive force on the vortex exerted by Meissner screening currents. Furthermore if a vortex trapped inside the superconductor approaches the edge, the screening current distribution is perturbed, thus affecting the

condition for flux quantization (2.4). This means that within the penetration depth λ vortices may carry less than one quantum of flux Φ_0 (Bardeen1961, Ginzburg 1962).

In thin films, due to demagnetizing effects, the effective superconducting penetration depth is much longer than the bulk value. Pearl (Pearl 1964) showed that for a thin film of thickness t with magnetic field applied perpendicular to the plane of the film the penetration depth is

$$\lambda_p \sim \lambda^2/t\,. \qquad (t<<\lambda) \qquad (2.13)$$

In the thin film case the problem of surface barriers is more difficult to treat (the method of images cannot be used). A recent review (Brandt 1995) lists *eight* theories explaining the surface barrier effect in thin films: flux entry may be hindered by divers mechanisms including geometric barriers, pinning within the film and interfacial roughness. Moreover in the thin film case non-quantized flux penetration effects are amplified. An important recent paper (Kogan 1994) suggests that the flux associated with vortex in a thin film is reduced below Φ_0 a large distance ($\sim 10\lambda_p$) from the edge.

2.3 The Josephson Effect

Josephson (Josephson 1962) first considered the case of two superconductors weakly coupled by a thin insulating barrier that allows quantum mechanical tunneling of Cooper pairs from one side to the other. He predicted the occurrence of some unusual phenomena in this situation – in particular a tunneling current at zero bias voltage, which is re-entrant under applied magnetic field. This was observed experimentally shortly afterwards and led to the award of the 1973 Nobel Prize to Josephson and Anderson. Structures exhibiting these phenomena (of which the tunnel junction described is the simplest example) are known as Josephson junctions or weak links. Weak links can also be created between regions of low T_C superconductor by means of a point contact (Zimmerman 1964) or constriction (Anderson 1964). A metallic or semiconducting barrier can also be used, either in a sandwich (Clarke 1969, 1971) or variable-thickness bridge (Gubankov 1973) configuration. Ion implantation usually has the effect of suppressing the T_C of a superconducting material, so a barrier can be created from a region of superconductor above its T_C (Arrington 1975). In high T_C materials the coherence length is extremely short and a junction is created merely by the presence of a grain boundary (Chaudari 1988). In the most anisotropic of these materials (e.g. Bi 2212) *intrinsic* Josephson tunneling occurs in the *c*-axis direction (Kleiner 1992). Josephson effects are predicted in any system with macroscopic phase coherence and have

recently been reported in superfluid ^{3}He (Giovanazzi 2000, Davis 2002) and Bose-Einstein condensates (Cataliotti 2001). The most common low T_C superconducor weak link configurations are shown in Figure 2.3.

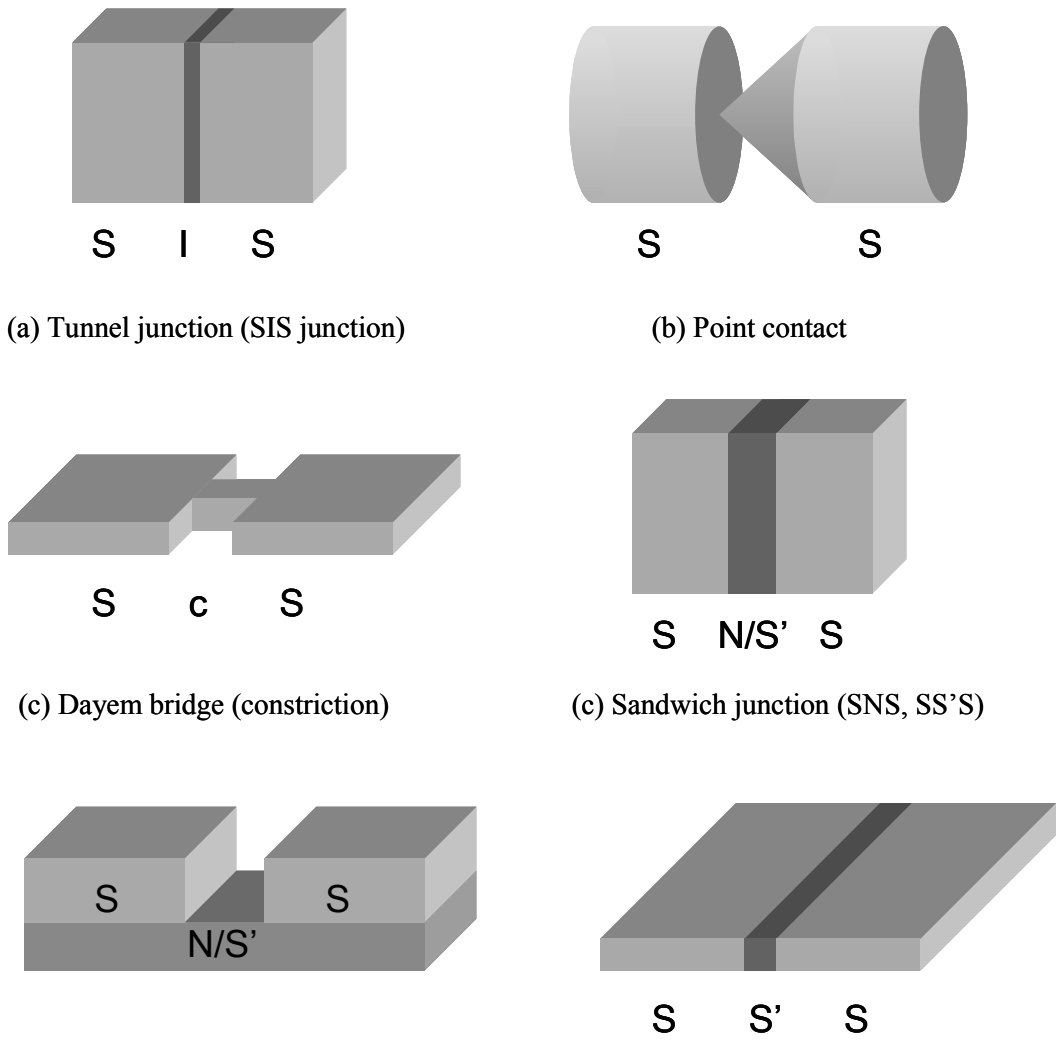

(a) Tunnel junction (SIS junction)

(b) Point contact

(c) Dayem bridge (constriction)

(c) Sandwich junction (SNS, SS'S)

(e) Variable thickness bridge (SNS, SS'S)

(f) Ion implanted bridge (SNS, SS'S)

Figure 2.3: Different types of weak links in low T_C superconductors. S stands for superconductor, S' for a superconductor above T_C, N for a normal metal, c for a constriction and I for an insulator. (N. B. N/S' means the barrier material is *either* N or S').

An elegant phenomenological derivation of the Josephson relations is given by Feynman (Feynman 1965). The probability amplitude of finding a Cooper pair on one side is given by ψ_1, and by ψ_2 on the other. In the superconducting state the wave function ψ_1 is the common wavefunction of all the pairs on one side and ψ_2 is the corresponding function on the other side.

In this simple symmetrical case the material on both sides is assumed the same and there is no magnetic field. The two amplitudes can then be related in the following way:

$$i\hbar \frac{\partial \psi_1}{\partial t} = U_1 \psi_1 + K \psi_2 \tag{2.14}$$

$$i\hbar \frac{\partial \psi_2}{\partial t} = U_2 \psi_2 + K \psi_1 \tag{2.15}$$

A finite value of the coupling amplitude K allows leakage from one side to the other. If the two sides were identical U_1 would equal U_2. However, if a voltage bias is applied across the junction $U_1 - U_2 = 2eV$. Defining the zero of energy halfway in between the two equations become:

$$i\hbar \frac{\partial \psi_1}{\partial t} = eV \psi_1 + K \psi_2 \tag{2.16}$$

$$i\hbar \frac{\partial \psi_2}{\partial t} = -eV \psi_2 + K \psi_1 \tag{2.17}$$

i.e. the standard equations for two coupled quantum mechanical states. After (2.12), for the wavefunctions of the individual superconductors we can now write:

$$\psi_1 = \sqrt{\rho_1} e^{i\theta_1} \qquad \psi_2 = \sqrt{\rho_2} e^{i\theta_2} \tag{2.18,2.19}$$

where θ_1 and θ_2 are the phases on the two sides of the junction and ρ_1 and ρ_2 are the respective pair densities. Substituting into (2.16) and (2.17) and equating real and imaginary parts, four equations are obtained. Letting $\varphi = \theta_2 - \theta_1$ the result is:

$$\dot{\rho}_1 = \frac{K}{\hbar} \sqrt{\rho_1 \rho_2} \sin \varphi \tag{2.20}$$

$$\dot{\rho}_2 = -\frac{K}{\hbar} \sqrt{\rho_1 \rho_2} \sin \varphi \tag{2.21}$$

$$\dot{\theta}_1 = \frac{K}{\hbar}\sqrt{\frac{\rho_2}{\rho_1}}\cos\varphi - \frac{eV}{\hbar} \tag{2.22}$$

$$\dot{\theta}_2 = \frac{K}{\hbar}\sqrt{\frac{\rho_1}{\rho_2}}\cos\varphi + \frac{eV}{\hbar} \tag{2.23}$$

With equivalent superconductors on either side of the junction we can set $\rho_1=\rho_2=\rho_0$. Furthermore the electron density is assumed not to vary significantly from the equilibrium value ρ_0 with time as a result of the interaction. The current following from side 1 to side 2 would just be $\dot{\rho}_1$ (or - $\dot{\rho}_2$) or

$$I = I_C \sin\varphi\,, \tag{2.24}$$

where the critical current $I_C = 2K\rho_0/\hbar$ is the maximum current the structure can support without dissipation. This is known as the dc Josephson equation. From the second pair of equations we then obtain

$$\dot{\varphi} = \dot{\theta}_2 - \dot{\theta}_1 = \frac{2eV}{\hbar}\,. \tag{2.25}$$

This result is known as the ac Josephson relation; frequency ($\dot{\varphi}$) and voltage (V) are related by the fundamental ratio $2e/h$ = 485,597.9 GHz/V. The most accurate experimental study to date (Jain 1987) found the voltage difference between two separate Josephson devices driven by the same signal to be less than 3 parts in 10^{19}.

2.4 Josephson Junctions at Zero Voltage

The stationary properties of Josephson Junctions (I_C, I_CR_N) vary considerably with temperature depending on the nature of the barrier material. Hence considerable insight can be gained from studying I_C (T) and I_CR_N (T) data. This discussion draws heavily on the excellent review articles of Likharev (Likharev 1979) and Delin and Kleinsasser (Delin 1996).

2.4.1 Tunnel junctions and point contacts

The temperature dependent behaviour of these classic Josephson devices is well described by the theory of Ambergaokar and Baratoff (Ambergaokar 1963). This theory predicts for the critical current I_C of a tunnel junction at temperature T:

$$I_C = \frac{\pi}{2}\frac{\Delta(T)}{eR_N}\tanh\left(\frac{\Delta(T)}{2k_BT}\right), \tag{2.26}$$

where R_N is the normal state resistance of the junction (temperature independent in low T_C devices) and Δ is the energy gap of the (identical) superconducting electrodes. BCS theory predicts $2\Delta(0) = 3.53k_BT_C$ from which the curve (a) in Figure 2.4 is calculated. This equation is well established experimentally for low T_C materials (Fiske 1964). Critical currents and conductance of tunnel junctions decrease exponentially with barrier thickness – typical useful barriers are of the order 1 nm thick.

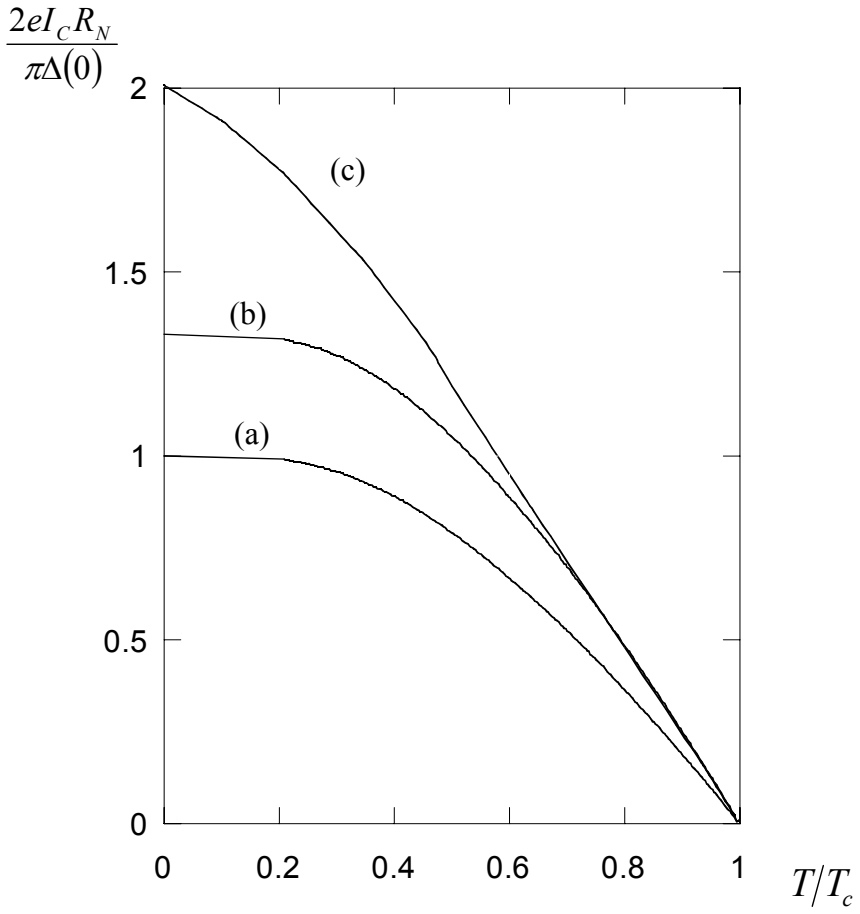

Figure 2.4: Predicted behaviour of $I_CR_N(T)$ for (a) a tunnel junctions (Ambergaokar and Baratoff) (b) a dirty point contact and (c) a clean point contact (Kulik and Omel'yanchuk**).**

In a point contact weak coupling is achieved by connecting two massive superconducting banks by a tiny bridge of superconducting material. Kulik and Omel'yanchuk (Kulik 1975, 1978) derived expressions for superconducting electrodes separated by a tiny orifice of radius a in an otherwise opaque interface, with $a << \xi_S$ the coherence length in the superconducting electrodes. For a 'dirty' contact (mean free path in the superconducting electrodes $l_S << a$) an analytic expression is obtained (the temperature dependence of which is shown in Figure 2.4 (b)). The temperature dependence for the 'clean' point contact ($a << l_S$) is shown in Figure 2.4 (c). All expressions yield convex $I_C R_N(T)$ curves: $I_C R_N$ rises sharply below T_C, flattening as T tends to zero. Note that point contacts have larger predicted $I_C R_N$ products than tunnel junctions for a given material: $eI_C R_N/\Delta(0) = \pi/2$, 0.66π and π for tunnel junctions, dirty point contacts and clean point contacts respectively.

2.4.2 Superconductor-normal metal-superconductor junctions

The physical basis for superconductor-normal metal-superconductor (SNS) is the proximity effect, the leakage of Cooper pairs out of the superconductor and into the normal metal near the SN interface. The mechanism by which this occurs is known as *Andreev reflection* (Andreev 1964). In the simplest approximation (Delin 1996), the critical current of a SNS junction decays exponentially with increasing electrode separation, L, as

$$I_C = I_{C0} \exp(-L/L_0) \qquad (L >> L_0). \qquad (2.27)$$

The characteristic decay length L is typically equal to ξ_n, the coherence length in N, which is usually much longer than typical tunnel barrier thicknesses. The temperature dependence of I_C is dominated by the exponential factor, resulting in an exponential increase in I_C below T_C - i. e. with upward concavity, in contrast to the tunnel junction and point contact curves.

The coherence length ξ_n reflects the size of the Cooper pair in the N material. Consider a normal metal with $T_C = 0$ and mean free path l_n as the largest relevant length scale. In the clean limit ($l_c >> \xi_{nc}$), electronic transport is ballistic and the coherence length is given by

$$\xi_{nc} = \tau_T v_F \qquad (2.28)$$

where $\tau_T = \hbar/(2\pi k_B T)$ =(1.22 ps-K)/T and v_F is the Fermi velocity (Deutscher 1969).

In the dirty limit electronic transport is diffusive and the usual random walk argument leads to an expression for ξ_{nd}:

$$\xi_{nd} = (\xi_{nc} l_n / \delta)^{1/2} = (\tau_T D_n)^{1/2} \tag{2.29}$$

where D_n is the carrier diffusion constant in N and δ is the dimensionality ($D_n = v_F l_n / \delta$). The subscripts n, c and δ refer to the normal metal layer, the clean and dirty limits respectively. In the context of SNS junctions, 'clean' and 'dirty' refer to the ratio l_n / ξ_{nc}, not the ratio of l_n to the contact dimensions. These equations represent the upper limit of ξ_n. For typical noble metals, v_F = 1-2 × 10^6 ms^{-1} so ξ_{nc} = 300-600 nm at 4.2 K. However for thin films the mean free path is limited by the film thickness. So if l_n < 100 nm, ξ_{nd} < 100-140 nm at 4.2K and the dirty limit prevails. In semiconductor N layers v_F is an order of magnitude lower, reducing ξ_{nc} accordingly and leading to extreme dirty limit junctions. In state-of–the-art two-dimensional electron gas (2DEG) systems l_n can be of the order of microns, allowing ballistic (clean limit) SNS structures to be created (van Wees 1996) which are of great interest in the field of mesoscopic physics.

2.4.3 De Gennes dirty limit theory

De Gennes (de Gennes 1964) produced one of the first systematic theoretical investigations of the proximity effect. The basic validity of this theory was confirmed by pioneering experimental studies on SN bilayers (Hauser 1966) and SNS sandwich junctions (Clarke 1969). This early work provides an intuitive basis for understanding the proximity effect and the behaviour of SNS junctions and agrees with the limiting cases of subsequent more general theories. The basis of the theory was the self-consistent expression for the spatially varying pair potential obtained by Gor'kov from microscopic BCS theory (Gor'kov 1960). Junction critical currents are then calculated using the phenomenological Ginzburg-Landau theory, which applies at temperatures down to $0.3T_C$.

The spatially varying pair potential $\Delta(\underline{r})$ is defined as

$$\Delta(\underline{r}) = V(\underline{r}) F(\underline{r}) \tag{2.30}$$

where $V(\underline{r})$ effective electron-electron interaction and $F(\underline{r}) = \langle \psi_\uparrow(\underline{r}) \psi_\downarrow(\underline{r}) \rangle$ is the pair condensation amplitude.

Considering an SN interface, where N is a dirty metal, de Gennes calculated that on the N side, the superconducting order parameter (or wavefunction) decays exponentially over the

coherence length, ξ_{nd}. On the S side the order parameter relaxes into the bulk from the interface value Δ_i with a characteristic length ξ_s (which is the same as Ginzburg-Landau coherence length for the superconductor ξ_{GL}). ξ_s is calculated in the same way as ξ_{nd} , but using the values of the mean free path and Fermi velocity of the superconductor. The results were obtained using the so-called single-frequency approximation, in which the only the lowest Matsubara frequency in the Fourier expansion of the Fermi-Dirac distribution is used. This simplifies the analysis, yielding analytic expressions, but these are only valid for long junctions (junction length $L >> \xi_{nd}$). A SNS junction can then be viewed as two back-to-back SN contacts (schematics shown in Figure 2.5). I_C can then be calculated as the extent of the overlap of the wavefunctions of the two superconducting electrodes.

$$I_C(T;L) = \frac{\pi}{4eR_N}\frac{|\Delta_i|^2}{k_B T_C}\frac{L/\xi_{nd}}{\sinh(L/\xi_{nd})}$$

$$\cong \frac{\pi}{2eR_N}\frac{|\Delta_i|^2}{k_B T_C}\frac{L}{\xi_{nd}}\exp(-L/\xi_{nd}). \qquad (2.31)$$

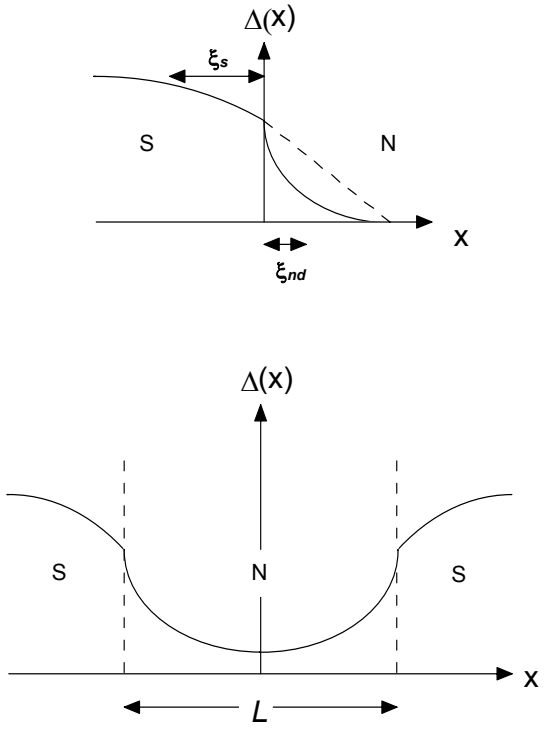

Figure 2.5: Δ(x) for SN and SNS structures in the de Gennes theory.

2.4.4 Microscopic SNS theory

To deal with arbitrary bridge length and temperature a more general theoretical approach is required. This was achieved by expressing the highly complicated general equations of stationary superconductivity (Gor'kov 1958b, 1960) in a more tractable form (Eilenberger 1968). The Usadel Equations (Usadel 1970) were derived from the Eilenberger theory in the dirty limit. These can be used to describe the behaviour of SNS junctions of arbitrary length (by abandoning the single-frequency approximation) and unlike the Ginzburg-Landau relations, are valid over the entire temperature range. Likharev (Likharev 1976) dealt with the basic case of a one-dimensional junction with rigid boundary conditions. A schematic of the variation of order parameter across the junction is shown in Figure 2.6.

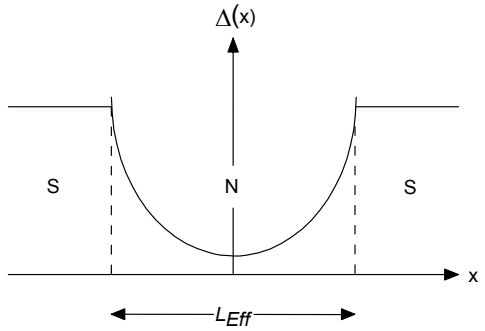

Figure 2.6: Schematic of the rigid-boundary condition model variation of the variation of Δ(x) across a SNS structure used by Likharev.

General results are obtained from the Usadel equations by numerical calculations but the limiting cases may be derived analytically. The predicted dependence of $I_C R_N(T)$ for various reduced junction lengths (L_{Eff}/ξ_n) is shown in Figure 2.6. For the case of a short SNS junction ($L_{Eff}/\xi_{nd}(T_c) = 0$) the Kulik-Omel'yanchuk expression for a dirty point contact is obtained. For a long junction under rigid boundary conditions not too far below T_C :

$$I_C(T;L) = \frac{2}{\pi e R_N}\frac{|\Delta_\infty|^2}{k_B T_C}\frac{L_{Eff}/\xi_{nd}}{\sinh(L_{Eff}/\xi_{nd})}$$

$$\cong \frac{4}{\pi e R_N}\frac{|\Delta_\infty|^2}{k_B T_C}\frac{L}{\xi_{nd}}\exp(-L_{Eff}/\xi_{nd}) \qquad (0.3\ T_C < T < T_C). \qquad (2.32)$$

which differs only by a factor of order unity from the de Gennes expression.

This theoretical approach was extended by Kuprianov and co-workers (Kurprianov 1981). They dealt with the effect of the proximity effect on the superconductor, the effects of interfacial barriers, finite electron-electron effects in the N interlayer (i.e. a 'normal' layer with finite T_C) and depairing effects due to large currents in the S electrodes.

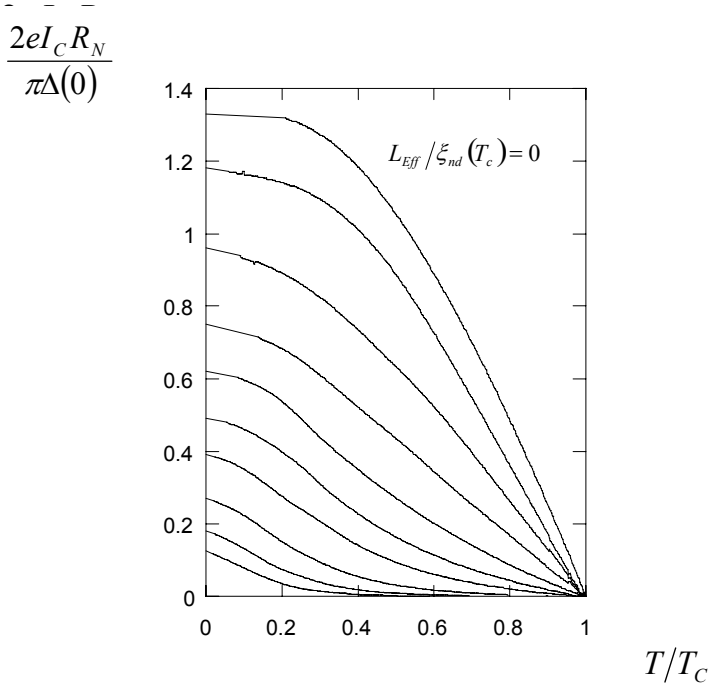

Figure 2.7: Behaviour of $I_CR_N(T)$ predicted by Likharev for $L_{Eff}/\xi_{nd}(T_c)$ = 0, 1, 2, 3, 4, 5, 6, 8, 10 and 12 (top to bottom).

2.4.5 Magnetic field response in the absence of self-field effects – short junction limit

An external magnetic field gives rise to a modulation of the critical current of the junction. The simplest case to consider is that of a short junction, where the redistribution of the current in the junction under the influence of its own self-field can be neglected. In zero applied magnetic field the phase difference between the electrodes is uniform and the dc Josephson relation holds; the current distribution across the length of the junction is uniform. When an external field H_z is applied in the plane of the barrier it penetrates not only the barrier (thickness L), but also the electrodes up to the London penetration depth λ_L. The phase difference then varies linearly with distance along the junction:

$$\frac{\partial\varphi}{\partial x}=\frac{2e\mu_0 d'H_z}{\hbar} \qquad \text{where} \qquad d'=L+2\lambda_L \qquad (2.33)$$

This equation can now be integrated and inserted into the dc Josephson relation. Integrating over the junction area gives the current I. The critical current I_C is then obtained by

maximizing I with respect to the constant of integration φ_0. For a uniform critical current density J_0 the junction

$$I_C(\Phi) = I_0 \left| \frac{\sin\left(\frac{\pi\Phi}{\Phi_0}\right)}{\frac{\pi\Phi}{\Phi_0}} \right| \tag{2.34}$$

where $\Phi = \mu_0 H_z w d' = B_z w d'$ and w is the junction width. Thus the critical current varies as the modulus of a sinc function – this is analogous to the case of Fraunhofer diffraction of light though a single slit. This is shown in Figure 2.8. Minima in I_C occur where an integer number of flux quanta are introduced into the barrier. Deviations from this ideal behaviour can result from an inhomogeneous current distribution across the junction – arising for example from inhomogeneities in the barrier. I_C becomes the Fourier transform of the current density distribution *J(x,y)*. Hence *J(x,y)* can be deduced from $I_C(\Phi)$. Numerous calculated examples for differing current distributions are given in (Barone 1982). Close to ideal behaviour is obtained in low T_C tunnel junctions with thick electrodes, whereas high T_C junctions with artificial barriers in general give poor correspondence due extreme barrier roughness and susceptibility to flux trapping.

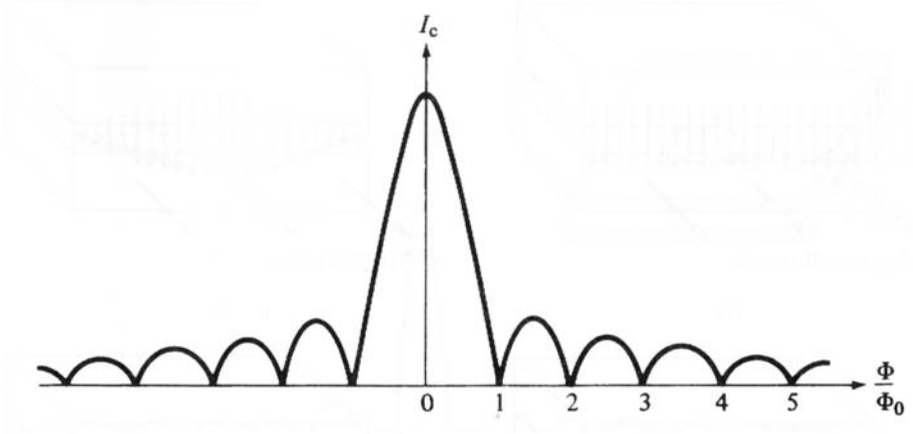

Figure 2.8: Modulation of critical current with magnetic flux in a short Josephson junction (Tinkham 1996).

2.4.6 Magnetic field response with self-field effects – long junction limit

The length scale over which self-field effects arise is the Josephson penetration depth, λ_J :

$$\lambda_J = \sqrt{\frac{\Phi_0}{2\pi\mu_0 d' j_c}}. \qquad (2.35)$$

Junctions of width $w >> \lambda_J$ are termed long junctions (λ_J is temperature dependent so a junction can change from short to long with decreasing temperature). The critical current is no longer proportional to the junction area as current flow becomes confined to the edges of the junction. At a given value of applied magnetic field there may be several possible solutions for the critical current, corresponding to different numbers of flux vortices trapped in the junction. This leads to a triangular $I_C(\Phi)$ pattern with incomplete suppression of critical current at the minima and irregular period, as shown in Figure 2.9 (Waldram 1996). When self-field effects come in to play, the geometry of the current input also becomes a significant factor in determining the overall shape of $I_C(\Phi)$.

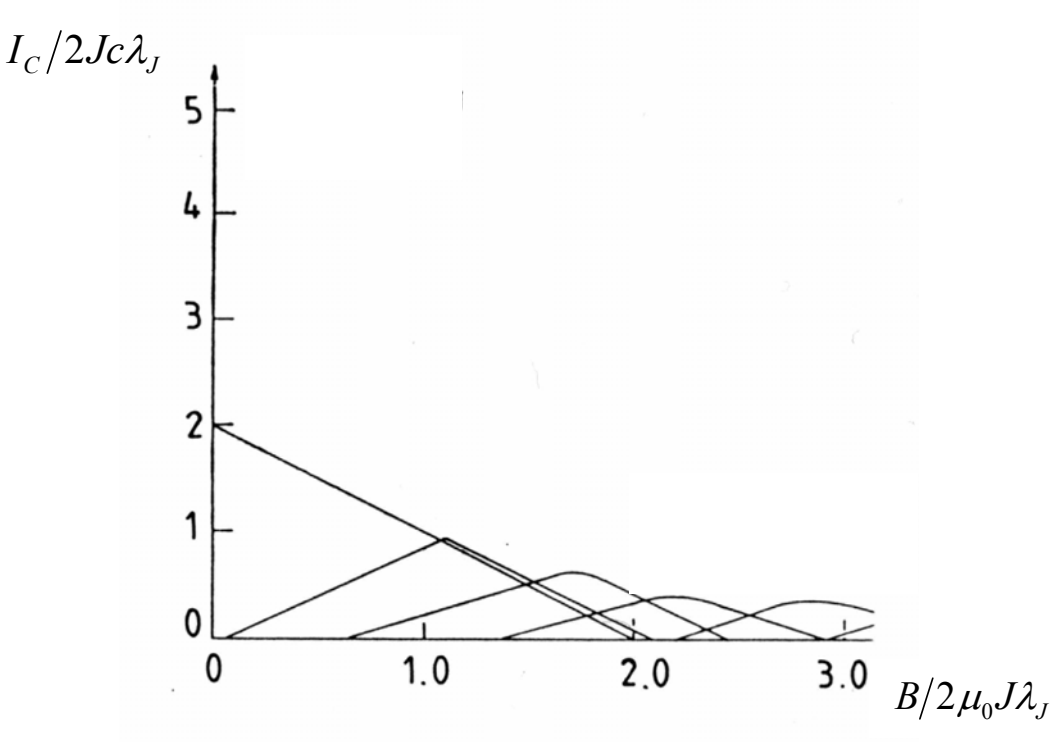

Figure 2.9: Simulated magnetic field response of a junction in the long limit with width $w = 10\lambda_J$. The overlapping modes correspond to different numbers of flux lines trapped in the junction (Owen and Scalapino 1967).

The evolution of the phase difference with respect to time (t) and position (x) in a one-dimensional long junction is governed by the time-dependent sine-Gordon equation (SGE) (Tinkham 1996):

$$\left[\nabla^2 - \frac{1}{\bar{c}^2}\frac{\partial}{\partial t^2}\right]\varphi(x,t) - \frac{1}{\lambda_J(x)}\sin\varphi(x,t) = 0 \qquad (2.36)$$

where $\bar{c}$ is the Swihart velocity (the speed of electromagnetic radiation in the barrier). The bias current is introduced via its self-field in the boundary condition (2.33). This equation describes the propagation of waves in a nonlinear dispersive medium. Solutions of the equation are solitons – particle-like excitations that propagate without dispersion along the junction barrier, which acts as a Josephson transmission line bounded by the superconducting electrodes. These solitions are known as fluxons or Josephson vortices. The flux Φ_0 associated with such a Josephson vortex is confined on the length scale of λ_J.

In a real Josephson junction dissipative losses must be taken account. Hence it is more appropriate to use the perturbed sine-Gordon equation (PSGE) (McLaughlin 1978, Barone 1982, Ustinov 1998). For a one-dimensional junction this is:

$$\varphi_{xx} - \varphi_{tt} - \sin\varphi = \alpha\varphi_t - \beta\varphi_{xxt} - \Gamma \qquad (2.37)$$

where the spatial co-ordinate is normalized to λ_J and time to the plasma frequency ω_p of the junction ($\omega_p \equiv \bar{c}/\lambda_J$). The indices denote partial derivatives. The loss terms $\alpha\varphi_t$ and $\beta\varphi_{xxt}$ represent the quasiparticle tunneling current and surface losses respectively; Γ is the bias current normalized to the critical current of the junction. In the steady state, the bias current supplied by the external circuit compensates for the dissipation.

There are no analytic solutions to the PSGE. In the case of weak boundary conditions perturbation theory yields propagating solutions (fluxons). Fluxon modes can be excited in the absence of an external magnetic field, giving rise to resonances in the current-voltage (I-V) characteristic of a junction (Fulton 1973). Fluxons traverse the width of the junction under the action of the bias current. A fluxon arriving at the junction boundary undergoes reflection into an anti-fluxon, which is then driven back into the junction. The electromagnetic properties of highly anisotropic high T_C superconductors such as bismuth 2212 are dominated by fluxon motion within the Josephson superlattice (Kleiner 1992, 1994). The weak boundary condition case is most elegantly realized in annular SIS junctions where the barrier is effectively infinite - Section 2.6 (Davidson 1985). With strong boundary

conditions solutions are obtained numerically. The non-linear interaction of the Josephson current with the cavity modes of the Josephson transmission line gives rise to steps in the *I-V* characteristic. The amplitude of these 'Fiske resonances' (Fiske 1964) depends on the external magnetic field.

2.5 Josephson Junctions at Finite Voltages

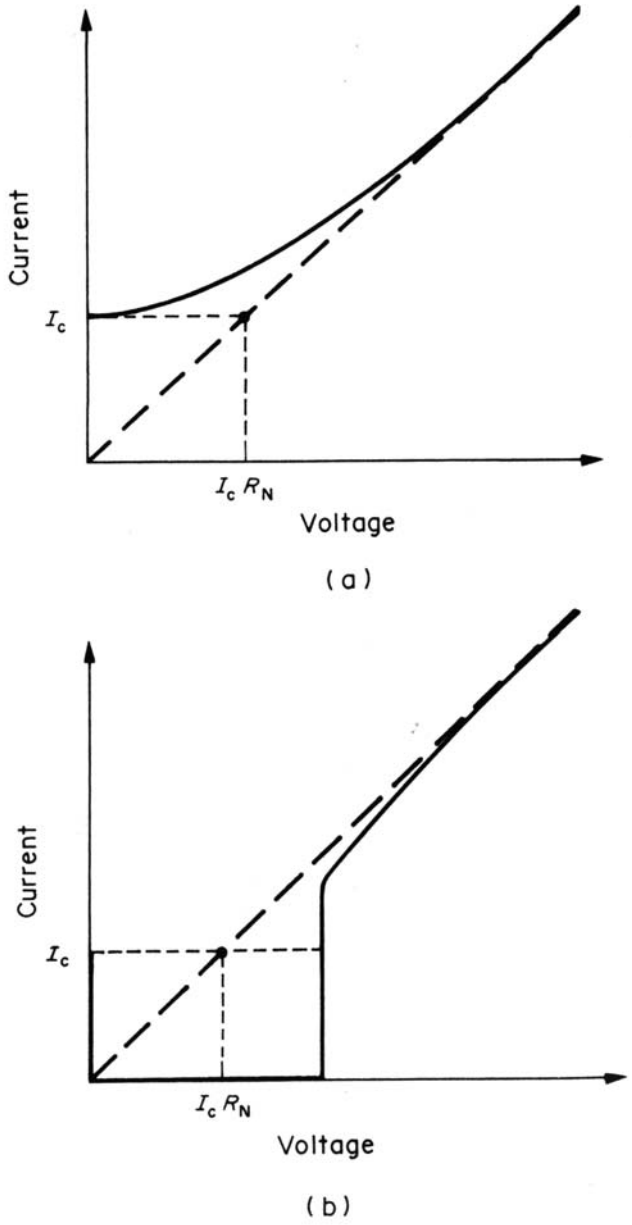

Figure 2.10: Josephson junction current-voltage *(I-V)* characteristics (Rowell 1992).
(a) SNS junction (b) SIS junction.

At finite voltage bias the barrier is crossed by, not only an ac supercurrent, but also by a current of unpaired charge carriers (quasiparticles). The mode of quasiparticle transport across the barrier depends on the nature of the barrier material: with an insulating barrier the mechanism is tunneling; with metallic barriers the transport mechanism can be either ballistic (clean metal) or diffusive (dirty metal). The difference in the resulting *I-V* characteristics is illustrated in Figure 2.10.

With a metallic barrier (a) the *I-V* characteristic takes the form of a hyperbola as the quasiparticles crossing the barrier at finite voltage encounter an ohmic resistance. In the case of an insulating barrier (b) quasiparticle tunneling first occurs at a voltage Δ/e, where Δ is the energy gap of the (identical) superconducting electrodes. In practice this results in a current voltage characteristic with large hysteresis. For technological applications such as Rapid Single Flux Quantum Logic (RSFQ – Likharev 1991) non-hysteretic *I-V* characteristics are desired. Hence although in most current commercial applications Nb-AlO_3-Nb SIS junctions (Geerk 1982) are employed, these have to be shunted with external resistors. This is an obstacle to future improvements in integration densities in large-scale superconducting circuits (Likharev 1999).

2.5.1 The resistively shunted junction model

In the first approximation metallic barriers result in an ohmic quasiparticle current. Hence the Josephson junction can be modeled phenomenologically as a lumped circuit consisting of a Josephson element in parallel with a resistor – the Resistively Shunted Junction (RSJ) model (Stewart 1968, McCumber 1968). In practice electrical transport across a Josephson junction is measured by dc current biasing, as the output impedance of a bias source is usually much greater than R_N. The total current in the absence of noise is

$$I = \frac{V}{R_N} + I_C \sin\varphi = \frac{\hbar}{2eR_N}\dot{\varphi} + I_C \sin\varphi\,, \tag{2.38}$$

using both the ac and dc Josephson relations (Equations 2.24 and 2.25). The time dependant voltage $V(t)$ is obtained by integrating using the method of separation of variables:

$$V(t) = I_C R_N \frac{\left(I/I_C\right)^2 - 1}{I/I_C + \sin\left(I_C R_N \frac{2e}{\hbar}\sqrt{\left(I/I_C\right)^2 - 1}\cdot t + \varphi_0 \right)}. \tag{2.39}$$

This expression shows the key importance of the $I_C R_N$ product of a Josephson junction – this factor, virtually independent of junction geometry, determines the maximum ac voltage amplitude obtainable at a given operating frequency. Hence to achieve optimum performance in electronic circuits based on Josephson junctions, the $I_C R_N$ product should be tailored as far as device constraints allow. Identifying the prefactor to *t* as an angular frequency and substituting in the ac Josephson relation we obtain the averaged dc voltage

$$\overline{V} = 0 \qquad \text{when} \qquad I \le I_C$$

$$\overline{V} = I_C R_N \sqrt{(I/I_C)^2 - 1} \qquad \text{when} \qquad I > I_C . \qquad (2.40)$$

This expression gives rise to a curve identical to that in Figure 2.10 (a) (although the voltage is strictly oscillating, this takes place at a such a high frequency as to be impossible to observe directly in normal dc measurements).

The RSJ model can be extended to take into account finite junction capacitance – a second order term is introduced into (2.38) yielding an equation of sine-Gordon type (2.36). The effect of significant capacitance is to produce a hysteretic *I-V* characteristic. Furthermore, the effects of thermal noise, which leads to rounding of the *I-V* characteristics at finite temperatures, can be incorporated in the model. Noise is characterized by a dimensionless parameter γ (Ambergaokar 1969):

$$\gamma = \frac{\hbar I_C(T)}{e k_B T} . \qquad (2.41)$$

When γ is large the rounding of the *I-V* characterstic is negligible; as γ tends to zero the *I-V* characteristic becomes ohmic (Barone 1982).

In spite of its crude basic assumptions and the appearance of more sophisticated theories (e.g. Time Dependant Ginzburg-Landau theory (Gor'kov and Eliashberg 1968)), the RSJ model remains popular. It gives a reasonable approximation to the measured *I-V* characteristics of Josephson junctions and it also is easy to implement in models of electronic circuits consisting of large numbers of Josephson junctions (Likharev 1986).

2.5.2 Microwave properties of Josephson junctions

Let us now consider the dc and ac Josephson relations once more ((2.24) and (2.25)). Substitution of the ac relation into the dc relation leads to:

$$J = J_0 \sin\left(\frac{2eV}{\hbar}\cdot t + \varphi_0\right), \tag{2.42}$$

which illustrates that the application of a dc bias voltage across the junction gives rise to an ac supercurrent with an angular frequency (f_J), related to applied voltage (V) by $f_J = 2eV/h$. This *Josephson frequency,* f_J, is voltage dependent and lies typically in the microwave region: for a voltage of 10 μV f_J *is* 4.8 GHz. This unique fundamental relationship between frequency and voltage is now exploited in the international standardization of the volt (Kose 1976).

In a junction under dc bias these Josephson oscillations can be synchronized ('phase locked') with an applied microwave (HF) signal. This leads to the appearance of *Shapiro steps* in the junction *I-V* characteristic at discrete voltages V_n:

$$V_n = n\frac{h}{2e}f_{HF}, \tag{2.43}$$

where n is an integer (Shapiro 1963). At the n^{th} step, Josephson oscillations of frequency beat with the n^{th} harmonic of the HF signal, which is generated due to the non-linearity of the junction. It is useful to note that the I_CR_N product can also be used to define a characteristic frequency f_C:

$$f_C = \frac{2e}{h}I_CR_N, \tag{2.44}$$

and hence a reduced frequency Ω:

$$\Omega = \frac{hf_{HF}}{2eI_CR_N} = \frac{f_{HF}}{f_C}. \tag{2.45}$$

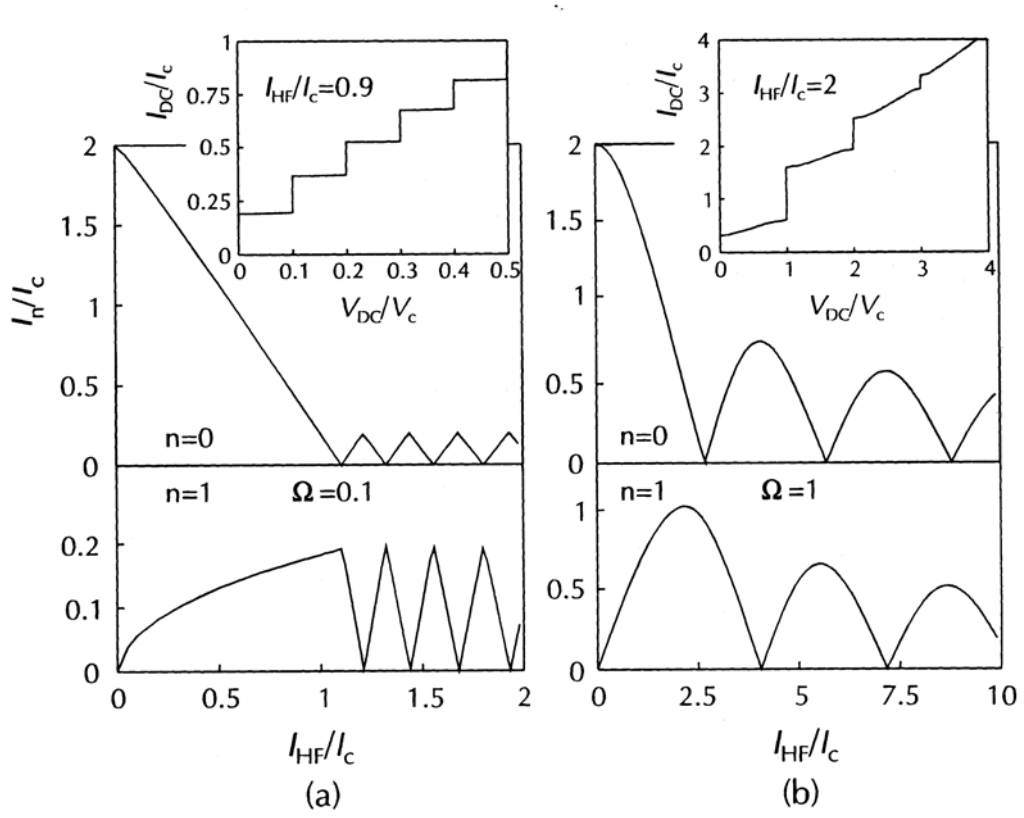

Figure 2.11: Dependencies of the amplitudes of the zero voltage step (n=0) and first Shapiro step (n=1) on the applied HF current for (a) Ω = 0.1 and (b) Ω = 1. The insets show example current-voltage characteristics for these frequency values at the indicated I_{HF} values (Terpstra 1994).

If an HF *voltage* source is used the locking range ('step amplitude') I_n of the n^{th} Shapiro step is found to depend on the HF voltage amplitude in the following way:

$$I_n = 2I_C \left| J_n\left(\frac{2eV_{HF}}{hf_{HF}}\right)\right|, \tag{2.46}$$

where J_n is the n^{th} order Bessel function of the first kind. If the junction is both dc and HF current biased (the situation in the experiments in this investigation) then the RSJ equation (2.38) must be integrated numerically to obtain the excited *I-V* characteristics. The shape of the steps and their amplitudes are determined by the reduced frequency Ω. The dependence of the amplitudes of the zero voltage (n = 0) and first (n = 1) Shapiro step on the HF current are shown for different values Ω of in Figure 2.11. Qualitatively Ω may be regarded as a measure of the ratio of the fractions of the HF current passing through the shunt resistance and the Josephson element.

For low frequencies ($\Omega<<1$, Figure 2.11 (a)) the main part of the HF current I_{HF} passes through the Josephson element and the junction is truly HF current biased. This differs strongly from the HF voltage biased case in that the steps heights are much smaller than those predicted by (2.45) and the intervals between the steps are almost horizontal. With $\Omega=1$ (Figure 2.11 (b)) most of the HF current flows through the resistor and the junction becomes effectively HF voltage biased. In all cases, however, the period of the oscillations in step height is determined by Ω. Hence the period can be used in experiments as a precise measure of $I_C R_N$ for an excited junction.

2.6 Josephson Junctions with Circular Barriers

This final section concerns the dynamics of circular (infinite) barrier Josephson junctions. The unique properties of infinite (circular) barrier Josephson junctions have long been recognized (Tilley 1966, Cheishvili 1969, Sherrill 1979). The most striking property of a junction with a cylindrical barrier is that flux will be trapped in the barrier as quanta leading to an abrupt suppression of the critical current I_C. Early attempts were made to fabricate cylindrical superconductor-insulator-superconductor (SIS) junctions in the ideal geometry (Figure 2.12 (a)) by thin-film deposition on the surface of a wire (Kuwada 1983, Sherrill 1981). A new approach to realizing junctions in this geometry is explored in Chapter 7.

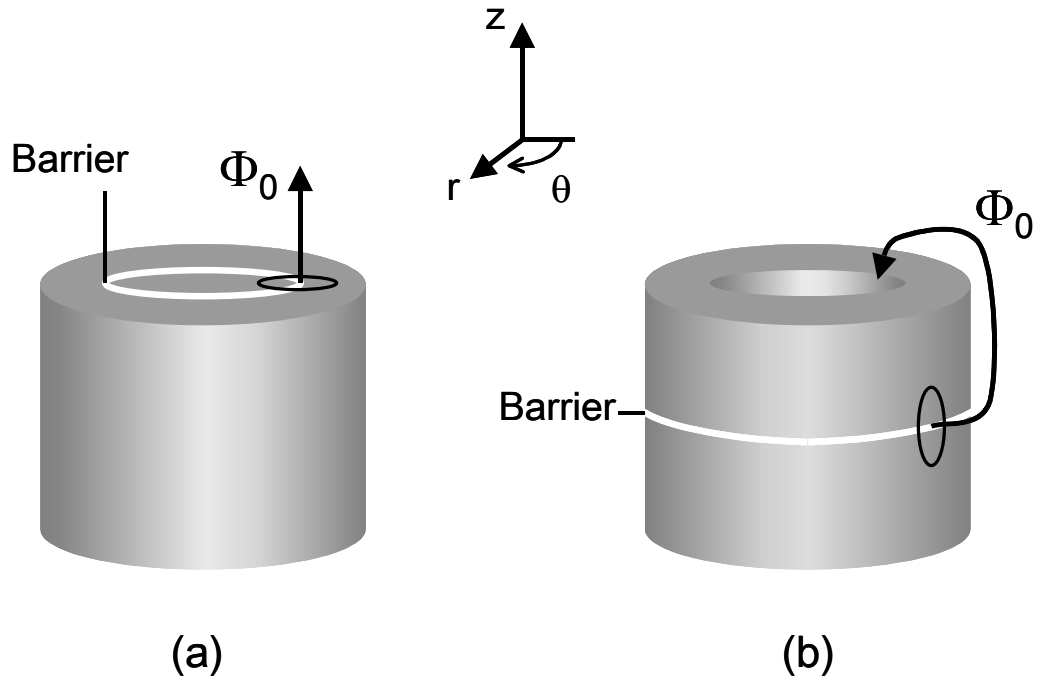

Figure 2.12: Circular junction geometries in the long junction limit (a) the ideal 'Corbino' geometry. The barrier is in the same plane as the electrodes and current can be passed radially through the device. (b) the 'Lyngby' annular junction geometry. This device is patterned from a conventional SIS trilayer. Current flow is in the z-direction. A trapped fluxon is wrapped around one of the electrodes. The total flux linking the junction can be altered by applying an external field in the (r,θ) plane.

2.6.1 Annular Josephson junctions

Recent experimental work has focused on non-ideal geometries that can be realized to a high degree of accuracy using conventional microfabrication techniques. An annular SIS junction (Figure 2.12 (b)) is formed by patterning a SIS tunnel junction into a ring, yielding a high quality circular barrier of carefully controlled dimensions (Davidson 1985). The geometry is non-ideal insofar as the junction is not in the same plane as the electrodes. Fluxons can be trapped in the barrier by applying a field or a bias current during cooling (Ustinov 2002) – in the optimal case flux will be wrapped around one of the electrodes as illustrated.

The annular geometry provides an ideal opportunity to study the Sine-Gordon dynamics of fluxons (Section 2.4.6). For a long SIS junction in this geometry, the underdamped conditions and the lack of edge reflections, fluxon motion up to superluminal velocities can be achieved (leading to Lorentz contraction of fluxons (Laub 1995) and, in stacked annular junctions, the emission of Cherenkov radiation (Goldobin 1998)). By tuning the inner and outer radius of the annulus 'whispering gallery' fluxon modes can be created (Wallraff 2000a). Quantum tunneling of vortices between the lobes of a heart-shaped annular junction may provide the future basis of a quantum computer (Wallraff 2000b, 2001). If a vortex is trapped in the annular junction during cooling through the superconducting transition it cannot escape – below T_C the multiply connected topology permits only creation or annihilation of fluxon-antifluxon pairs. The stability of the trapped fluxon can be exploited in X-ray detector applications, where an SIS junction operates in the subgap regime and the dc Josephson current must be suppressed (Nappi 1997). Furthermore this property of annular junctions is believed to shed light on cosmological theories (Kanvoussanaki 2000, Nappi 2002): the 'Kibble-Zurek' scenario describes analogous symmetry breaking processes during second order phase transitions in the aftermath of the Big Bang (Zurek 1996). There remain however some other interesting properties predicted for circular junctions, which cannot be observed in the annular geometry.

2.6.2 Berry's phase and the Magnus force

The discrepancy between the behaviour of quantized vorticies in superconductors and superfluid ^{4}He has long puzzled physicists (Vinen 1969, Tilley 1990). In superfluid ^{4}He the force on a vortex best described in terms of the Magnus effect (Vinen 1961) that is to say, a vortex moving through the superfluid experiences a transverse force, in much the same way as a rotating ball traveling through the air. In a superconductor, the metallic lattice provides a fixed frame of reference, so the transformation used to derive the Magnus force in superfluid ^{4}He cannot be applied. Furthermore, in a superconductor the superfluid is *charged*, hence a

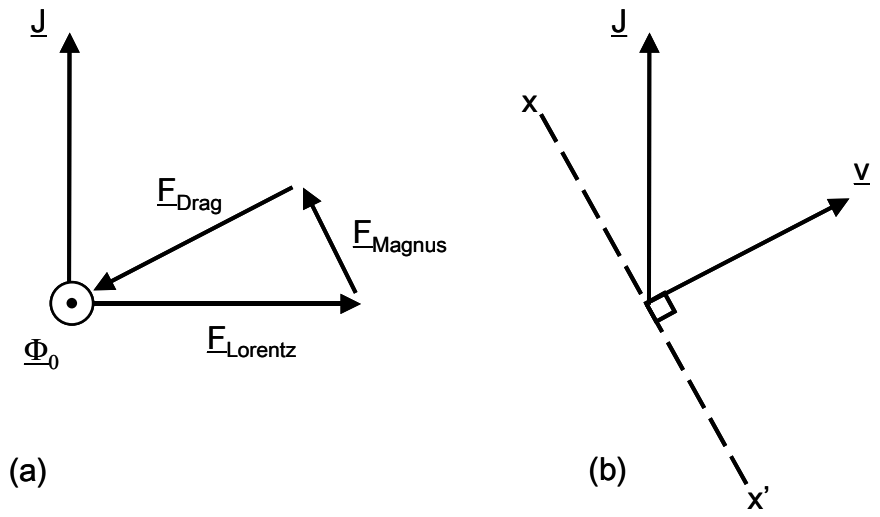

Figure 2.13: (a) The forces acting on a vortex in a superconductor with current density $\underline{J}$ in the most general case (b) the resultant direction of vortex motion $\underline{v}$.

Lorentz force is liable to arise between the flux lines and the electric current. Recently the existence of a Magnus force on a vortex in the superconducting case has been justified in terms of microscopic BCS theory by invoking Berry's geometric phase (Ao and Thouless 1993, Gaitan 1995). Berry (Berry 1984) recognized the very general result that a quantum system's wavefunction may not return its original phase after its parameters cycle slowly (adiabatically) around a circuit. This result applies to an astonishingly wide variety of physical systems* (Shapere 1990).

The steady state motion of an isolated vortex $\underline{\Phi}_0$ in a region of constant current density $\underline{J}$ is governed by the equation

$$\underline{J} \times \underline{\Phi}_0 - \alpha\left(\underline{v} \times \underline{\Phi}_0\right) - \beta \underline{v} = 0 \qquad (2.46)$$

The first term represents the Lorentz force $\underline{F}_{Lorentz}$, the second term the Magnus force $\underline{F}_{Magnus}$ and the final term the viscous drag $\underline{F}_{Drag}$ contributed by the movement of the normal core of the vortex (Poole 2000). Flux flow occurs with direction and velocity $\underline{v}$. This generates a transverse electric field and hence a voltage drop along the direction x-x'. If the dominant force is the Magnus force, vortex flow will occur in the direction of current flow, giving rise to a transverse (Hall) voltage. If the Lorentz force dominates, vortex motion is perpendicular to the current and the voltage is longitudinal. In experiments the latter effect is much stronger. In measurements on bulk superconductors a secondary Magnus force is hard to detect, as vortex motion is also influenced by lattice defects in the sample.

* 'The phase that launched a thousand scripts' (Berry 1990 - after Homer)

It has recently been proposed (Gaitan 1996, Gaitan 2001) that a Josephson junction in the ideal 'Corbino' geometry of Figure 2.12 (a) presents an opportunity to measure the Berry's phase-induced Magnus force on a vortex trapped in the barrier (conventional junction geometries, including the annular junction of Figure 2.12 (b) are unsuitable for this experiment, as the direction of vortex motion is always perpendicular to the tunneling current, causing the Magnus force to vanish). A Magnus force term acts in addition to the usual current bias driving force term Γ (2.37). This force $\delta\Gamma$ varies with time and position. Numerical simulations (Plerou 2001) predict shifts in the *I-V* characteristic of the junction due to this effect. The junction can be of SIS or SNS type with a clean barrier. Above a cutoff temperature (crudely estimated at under 1 mK) the Berry's phase effect will be masked by spectral flow of quasiparticle states within the vortex core (Makhlin 1995).

Chapter 3: Experimental Methods

3.1 Summary

This Chapter details the techniques used to fabricate and measure the devices under investigation in this thesis. The basic device fabrication method (used to produce the devices described in Chapters 5 and 6) can be summarized in the following steps:

- Substrate preparation and cleaning.
- Photolithography.
- Film deposition by dc magnetron sputtering.
- Lift-off and edge bead removal.
- Device fabrication using the focused ion beam microscope (FIB).

The multilayer devices of Chapter 7 required the use of additional techniques:

- Sputtering of insulating layers.
- Argon ion milling.

There then follows a review of the measurement facilities used in this investigation:

- Devices Rig: Measurement of *I-V* characteristics at different temperatures, magnetic fields, under microwave irradiation. Adaptation of electronics for low-noise measurement with the aid of a lock-in amplifier.
- Heliox^{TM} ^{3}He cryostat.

3.2 Fabrication

3.2.1 Substrate preparation and cleaning

The 5 mm × 10 mm substrates used for the fabrication of the devices used in this investigation were cut from an oxidized silicon wafer using a dicing saw. Oxidized silicon was chosen as a substrate as it is robust and a reliable insulator. The following steps were taken to clean the freshly–cut substrates

- Heating followed by immersion in acetone to melt and remove remaining wax from the dicing process. Soaking in chloroform overnight.
- Placing in an ultrasound bath in a beaker of chloroform for 30 minutes.
- Wiping with a cotton bud soaked in acetone and airbrushing with acetone.
- Rinsing with isopropanol.
- Drying with filtered compressed air.

The substrates were then examined under an optical microscope and cleaned further if necessary.

3.2.2 Photolithography

Photolithography was carried out in the device materials group class 100 clean room. The typical procedure for photolithographic patterning in preparation for lift-off was as follows:

- The substrate was airbrushed with acetone and dried with filtered compressed air to remove dust.
- The substrate was placed on 100°C hotplate for ~1 minute to remove any remaining solvent residues.
- The substrate was placed on the resist spinner and covered with 4-5 drops of Hoechst AZ1529 photoresist using a pipette.
- The spinner was rotated at 6000 rpm for 30 s giving a 2.37 μm layer of resist.
- The sample was removed from the spinner chuck and baked to harden the photoresist on the 100°C hotplate for 1 minute.
- The edges of the sample exposed with UV light in the Karl Suess mask aligner for 30 seconds using a rectangular edge-bead removal mask.
- The exposed resist was developed away in a 4:1 solution of AZ developer to distilled water (development time ~10 s). The sample was then rinsed in distilled water and dried with compressed air, then inspected under green light in an optical microscope: total removal of the edge-beads is necessary to ensure good contact in the second exposure – the sample was returned to the developer until this was achieved.

- The second exposure (~10 s) was carried out using the CAM25 negative mask in the Karl Suess mask aligner, vacuum contact being required to define 2 μm width tracks

- To ensure sharp edges after lift-off samples were often treated in Chlorobenzene for 2 mins before developing.

- The sample was developed in a 3:2 distilled water: developer solution for 30 s. The sample was rinsed, dried and inspected with green light as before.

- If the results were unsatisfactory the resist was removed with acetone and the process repeated.

3.2.3 Deposition of metallic films

3.2.3.1 The principle of dc magnetron sputtering

In dc magnetron sputtering the cathode (to which the target material is attached) is held at a large negative voltage relative to the substrate and walls of the chamber. An argon plasma is ignited in the chamber by field emission of electrons from the cathode. The magnetron (a configuration of magnets situated underneath the target) serves to confine electrons close to the target surface, thereby increasing ionization in this region (Figure 3.1). Positively-charged Ar ions are then accelerated towards the cathode, dislodging atoms from the target and leading to the build up of a thin film on the substrate (Figure 3.2).

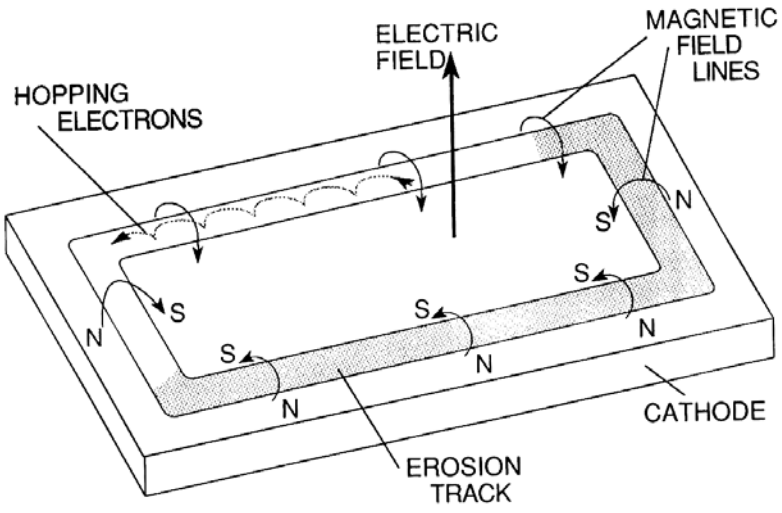

Figure 3.1: Applied fields and electron motion in the planar magnetron (Ohring 1992)

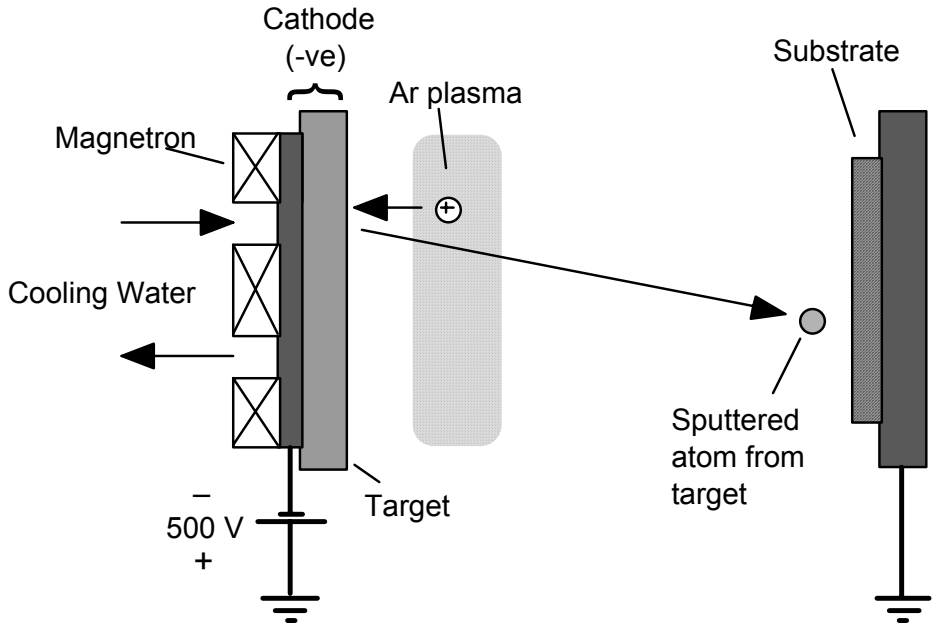

Figure 3.2: Schematic of the dc magnetron sputtering process.

3.2.3.2 Description of the Mark VII deposition system

Film deposition was carried out by Dr. Gavin Burnell in an Ultra-High Vacuum (UHV) magnetron sputtering system (the *Cambridge Device Materials Mark VII*). A schematic and picture of the system is shown in Figure 3.3. The system is fully described elsewhere (Blamire 1988). The system consists of an outer and inner chamber. The latter is surrounded by a liquid N_2 jacket, which serves to trap contaminating gases. The chamber is roughed by use of a rotary pump, and then pumped to high vacuum by a Turbo Molecular Pump, which is backed by the rotary pump. In this manner pressures as low as 2×10^{-7} Pa can be attained routinely.

The magnetrons and substrate stage are mounted on a single flange, which is then mounted on top of the chamber. In this way multilayer films can be deposited without breaking the vacuum. During the deposition the substrate holder is rotated. Under conditions of constant power, gas pressure and distance from the target, the deposition rate is determined by the rate of rotation. A computer controlled stepper motor mounted on the axle affords precise control of the rotational speed. Blanking of the substrates is achieved by rotating the stage away from the active magnetron.

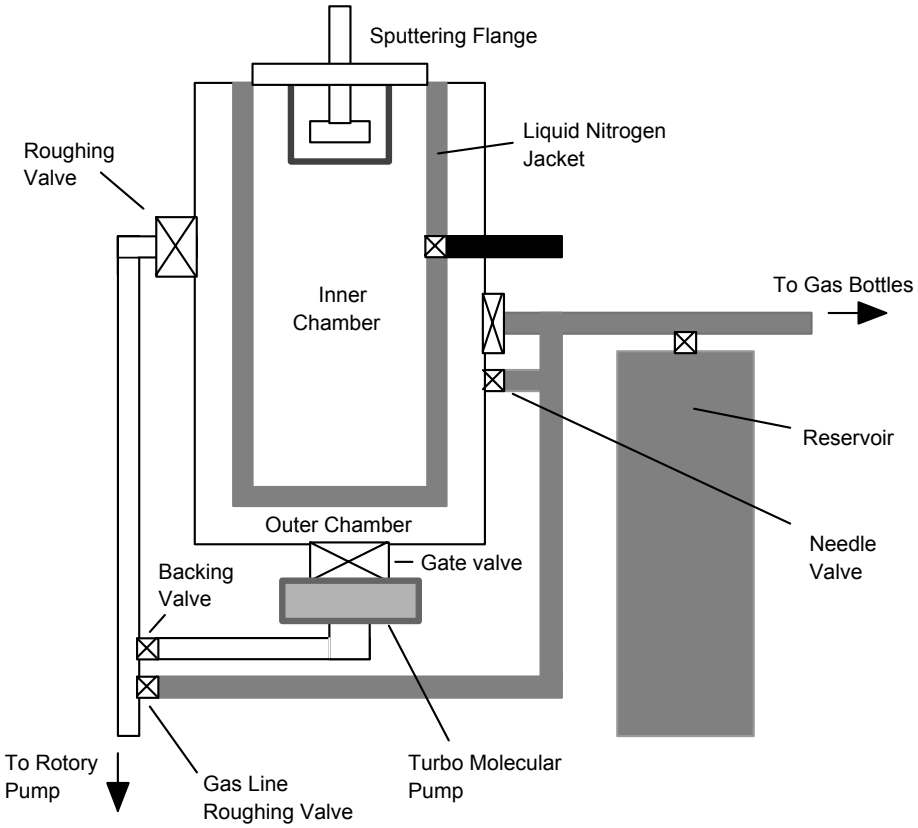

Figure 3.3: Schematic of UHV magnetron sputtering system (after Burnell 1998).

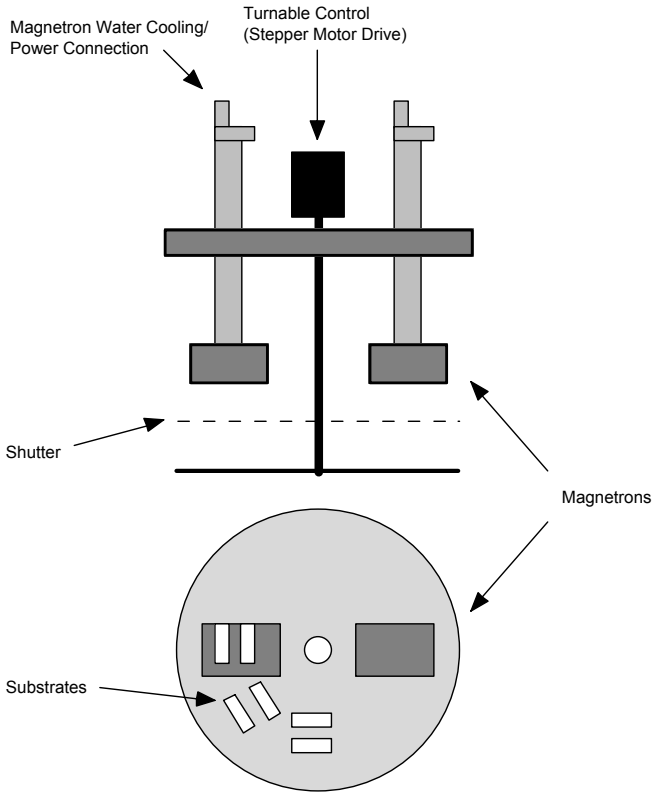

Figure 3.4: Sputtering flange (after Burnell 1998).

3.2.3.3 Deposition procedure

Firstly the system is allowed to pump overnight (9 hours minimum) during which time it is heated to approximately 120° C for four hours. This 'bake out' procedure encourages evaporation and removal of contaminants from the chamber walls. After base pressure is attained, sputtering is carried out using Ar gas (>99.9999 % purity) at pressures between 0.5 and 2 Pa depending on the material being sputtered. For this investigation mainly Nb-only layers and Nb-Cu bilayers were deposited (Au, W, Pd and Al also have been tried as substitutes for Cu). With the current flange the samples are below room temperature (no direct heating or cooling is available) so the resulting films are polycrystalline. The low deposition temperature has the advantages however that the films are smooth and migration of atoms between the different metallic layers is discouraged so the interfaces are sharp.

3.2.4 Lift-off and edge-bead removal

Lift-off is best performed directly after removal of the samples from the deposition system. The principle of lift-off is illustrated in Figure 3.5. The samples are immersed in a beaker of acetone and squirted gently with a pipette under the surface. In 5-10 minutes the areas where metal has been deposited on photoresist come free, leaving behind the desired pattern of metallization on the substrate. The samples are then rinsed with acetone and dried with compressed air.

(a) Photoresist is spun onto substrate.

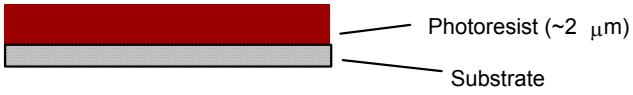

(b) After edge bead removal, sample is exposed with UV under negative mask, then developed (a chlorobenzene treatment prior to developing leads to overhanging resist edges).

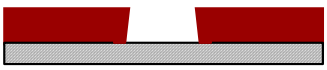

(c) Thin metal film is deposited on top of sample.

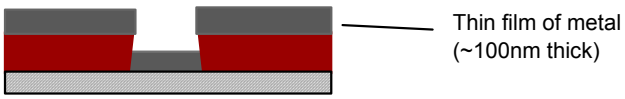

(d) Lift-off: immersion in acetone leads to removal of areas where photoresist adheres to substrate, leaving desired pattern of tracks behind.

Figure 3.5: The prinicple of lift-off.

For the edge bead removal a layer of photoresist is spun on the samples as in the first stage of photolithography. The rectangular edge-bead removal mask is used in the Karl Suess mask aligner to expose the resist over the metal around the edge of the contact pads. Typically two exposures of ~25 s are carried out. The samples are then developed in a 4:1 developer to distilled water for ~10 s. The metallization around the edge of the contact pads is then removed by immersion for 5-10 s in a solution of Hydrofluoric Acid (HF: HNO_3: H_2O 1:7:6). Extreme caution is exercised at this point, as HF solution is potentially lethal. The samples are inspected under an optical microscope and the redundant resist removed with acetone.

3.2.5 Patterning in the focused ion beam instrument

Submicron scale trenches are milled into the ~2 μm wide metal bilayer tracks using the Focused Ion Beam microscope (FIB). The depth of the cuts is accurately determined to ±5 nm with the aid of an *in situ* resistance measurement.

3.2.5.1 The FIB

Since its introduction in the late 1980s the FIB has become an essential tool in the microelectronics industry (Melngailis 1987, Young 1993). The principle of operation is similar to a Scanning Electron Microscope (SEM). The major difference is that in place of an electron source a gallium liquid metal source is used to emit a beam of positively charged Ga ions. This enables both imaging and milling of the sample. In addition, localized deposition of extra material (Pt) can be achieved by ion beam-induced decomposition of an organo-metallic gas. Hence this versatile instrument allows faulty circuits to be both inspected and modified. Recent reviews of FIB applications are available (Phaneuf 1999, Reyntjens 2001).

In this investigation we have exploited the ability of this instrument to create sub-micron scale features without resorting to complex and time-consuming techniques such as electron beam lithography. Other research uses of the instrument in our laboratory include the manufacture of masks for ion beam implantation (Kang 2001), site-specific sample preparation for Transmission Electron Microscopy (TEM - see Section 4.4), tip preparation for Scanning Near Field Optical Microscopy (SNOM - Milner 2002), microelectromechanical systems (MEMS –Daniel 1999) and patterning of mesa structures for intrinsic tunneling studies in high T_C superconductors (Winkler 1999).

3.2.5.2 Operation of FEI Inc. FIB 200

Full details of operation are given in the FEI 'Focused Ion Beam Workstation User's Guide' 7451 N. E. Evergreen Parking, Hillsboro, OR, USA, FEI Company. A simplified version is outlined here.

Figure 3.6 (right): Schematic of the FIB.

Figure 3.7 (below): Photo of the FIB (courtesy of A. Latif).

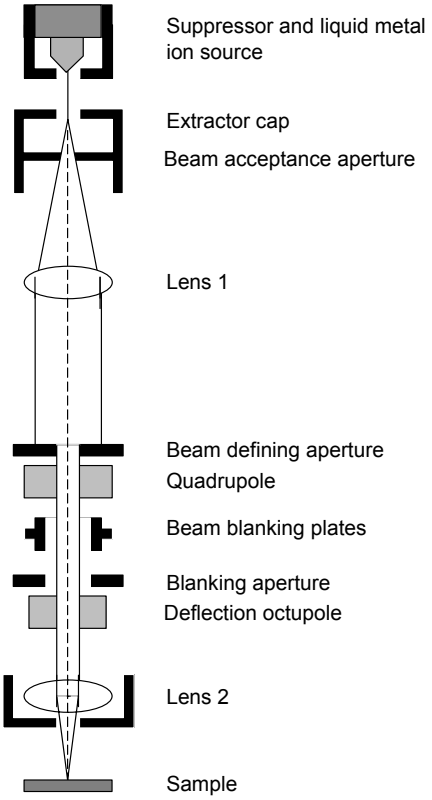

The heart of the FIB is the focusing column, which directs a beam of ions onto the sample. A high vacuum ($<5\times10^{-5}$ Pa) environment is maintained in the column to avoid beam interference with gas molecules. A strong electric field is applied to the liquid metal Ga source at the top of the column. The source self-assembles into a tip and emits positively charged Ga ions – the usual extraction current being 2.2 μA. Two electrostatic lenses, a steering quadrupole and an octopole focus the ion beam deflector in its passage down the column. The ion beam then passes through a small opening into the sample chamber (base pressure $<5\times10^{-4}$ Pa) where it strikes the sample. To minimize the beam diameter it is necessary to use the highest beam voltage and the smallest possible working distance. The column voltage is 30 kV and the working distance is between 15 and 75 mm. The beam current is the rate at which ions strike the sample and is controlled by the variable aperture. This can be set in the range from 1 pA to 1 nA. Due to the energy spread in the ion beam (~5 eV) the beam diameter increases with larger apertures and hence with increased beam current. This chromatic aberration limits the spatial resolution of the FIB instrument (whereas spherical aberration is the limiting factor in most SEMs). In this work a beam current of 4 pA was used as this was the minimum stable beam current obtainable, giving a spot size of 15 nm.

Secondary electrons and ions detected when the beam rasters across the surface of the sample are used to image the sample (the ion detection system allows the imaging of insulating as well as conducting samples). The beam is guided by the quadrupole steering plates and the octopole stigmator/deflection assembly provides scan and shift for fine field of view movement, as well as beam astigmatism correction. The milling of specified patterns into the sample is achieved with the aid of a scan control system.

Prolonged imaging at high magnifications leads to Ga implantation of the sample. This may lead to the alteration of sample properties. There is a beam blanking system in the focusing column which, when activated, diverts the beam away from the blanking aperture and into a Faraday cup. This blanking system also allows the beam current to be measured.

3.2.5.3 Device fabrication with the aid of an *in situ* resistance measurement

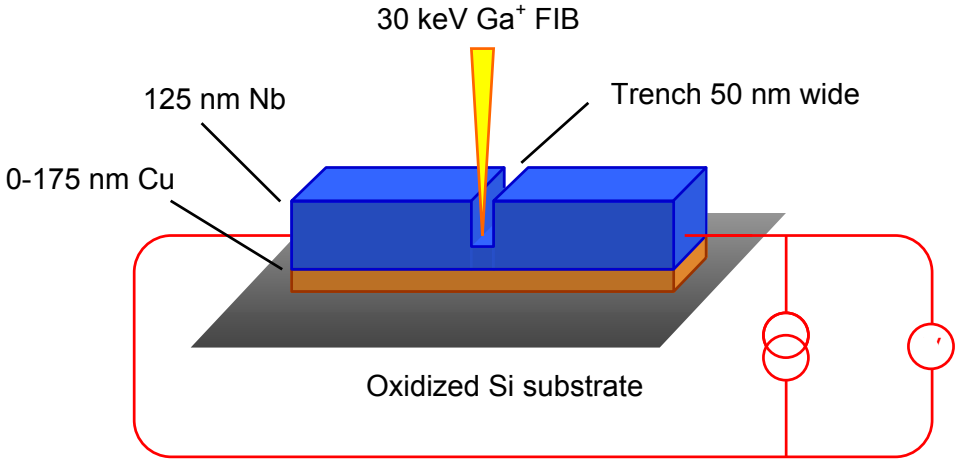

Figure 3.8: Schematic of *in situ* resistance measurement

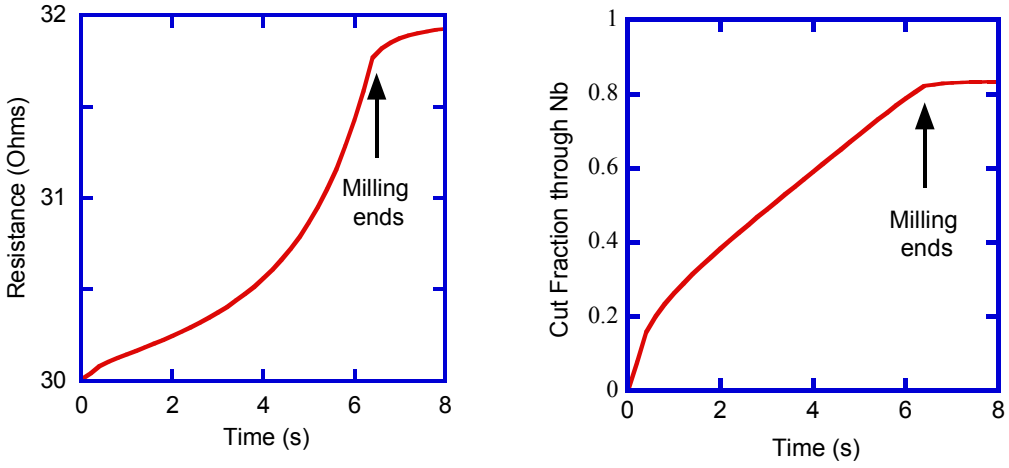

Figure 3.9: Graphs of resistance versus time and cutting depth versus time (mill time: 6.6 s)

Josephson junctions are created in the Nb-Cu tracks by milling narrow trenches down through the upper Nb layer to weaken the coupling (an area 50 nm × 2.5 μm would be milled for a given length of time). Previously cut depths were determined by scaling down the large area mill rates determined from the FIB end-point detection feature (Moseley 2000). This method proved unsatisfactory as the mill rate was found to be strongly dependant on the aspect-ratio of the cut being milled. To solve this problem Dr. Wilfred Booij and Dr. Adnan Latif developed an *in situ* resistance measurement technique. The sample is wire bonded to a specially designed chip-carrier linked to the outside of the chamber by an electrical feed through. Direct current was supplied and voltage signals were measured using a Keithley 2000 voltmeter; these instruments were read by LabVIEW software running on the FIB control computer. Hence a resistance measurement can be carried out on a track as it is being milled. This allows the depth of the trench (± 5 nm) to be extracted from the cutting data (Figure 3.9). The calculation is easiest for a cut into Nb only, so cutting depth would be calibrated with respect to cutting time on a Nb-only chip and then a Nb-Cu chip would be loaded without turning the beam off and cuts of identical time (and depth) made.

3.2.6 RF sputtering of insulating layers

For the devices discussed in Chapter 7 a second wiring layer was required. In order to isolate this from the bottom electrode a layer of insulating silica (SiO_2) was deposited over the structures.

3.2.6.1 The principle of RF sputtering

In order to achieve dc sputtering of insulating materials such as quartz ($\rho = 10^6$ Ωcm), unfeasibly high voltages would be required. The deposition of insulating thin films is commonly achieved by applying an ac signal to the electrodes at radio frequency (RF) – this is known as RF sputtering. Capacitive coupling of the RF generator to the insulating target ensures that only the target material is sputtered.

3.2.6.2 The Device Materials Group silica system

This deposition system is located in the Device Materials Group clean room. A schematic of the system is shown in Figure 3.10. A lift-off patterned sample is placed beneath the quartz target. The base pressure of 5 x 10^{-5} mbar is reached in 30 minutes. The Ar plasma is ignited at 8 Pa. When impedence matching of the RF source to the target is achieved (reflected power minimized; transmitted power = 50 W) the shutter is opened and deposition commences. After 30 seconds of sputtering at low pressure (2.7 Pa) for maximum adhesion,

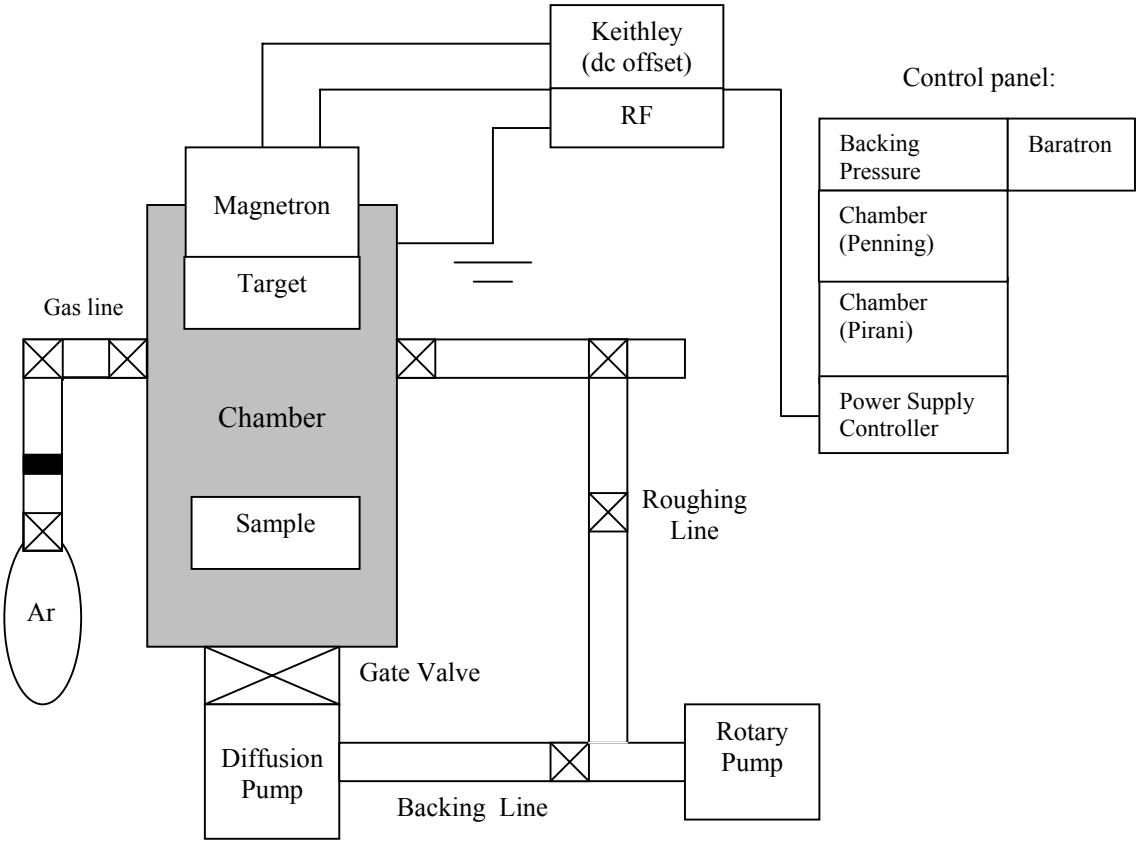

Figure 3.10: Schematic of the Device Materials Group Silica System.

the pressure is stabilized at 3.2 Pa. Sputtering is interrupted after 15 minutes to prevent baking of photoresist (there is no sample cooling in the system). The sputtering rate was typically 200 nm per 15 minutes.

3.2.7 Deposition of upper wiring layer

Via holes were milled in the insulating layer using the FIB as described in detail in Chapter 7. In order to deposit a top electrode without contact resistance the lift-off patterned sample is placed in the device materials group 'New-OAR' combined argon ion milling and dc magnetron sputtering system.

3.2.7.1 Ion milling

Ion milling is a purely physical milling process. The physics of the process is analogous to sputtering (material is sputtered *from* the sample surface by a directional ion beam). The most popular source for ion milling is the Kaufman source. A confined plasma (typically Ar) is used to generate ions. The ions are accelerated through a high potential (~500 V) to create a collimated beam, which bombards the sample. This kind of etch process is not selective and as the products are not volatile, redeposition effects may occur.

3.2.7.1 The New-OAR milling/deposition system

This system, located in the device materials group clean room, is invaluable for multilayer device processing. The lift-off patterned sample is mounted with vacuum grease or conducting silver paint on a cooled sample stage. This stage can be rotated to face either the ion gun or a variety of dc magnetron sputtering targets (available materials include Nb, Au, Ag and Al). Hence the surface of a sample can be cleaned by Ar ion milling before a metal layer is deposited. For the deposition of a high-quality wiring layer a typical procedure is as follows: The system is pumped overnight and liquid N_2 used to condense the chamber gases, allowing a base pressure of 4×10^{-6} mbar to be achieved. Milling in an Ar-only atmosphere proceeds at 2×10^{-3} mbar. Nb and Au metallization layers were deposited at $\sim 10^{-2}$ mbar.

3.3 Measurement Apparatus

3.3.1 Devices rig

This setup, constructed by Dr. Wilfred Booij and Dr. Gavin Burnell, contained most of the room temperature electronics needed by the various cryogenic probes used. The electronics were computer controlled, along with data acquisition and processing. Device measurements were made using an integrated dual current and low noise amplifier set. The resulting current monitor signal and amplified voltage response was digitized using a National Instruments Lab PC-1200 12 bit A/D converter board and the data processed by a LabVIEW™ program running on a Dell OptiPlex GXa PC. The 'Dualscope' software program written by Dr. Gavin Burnell allows simultaneous recording of up to 4 channels of data whilst controlling a separate magnetic coil power supply and/or providing a controlled current to the device.

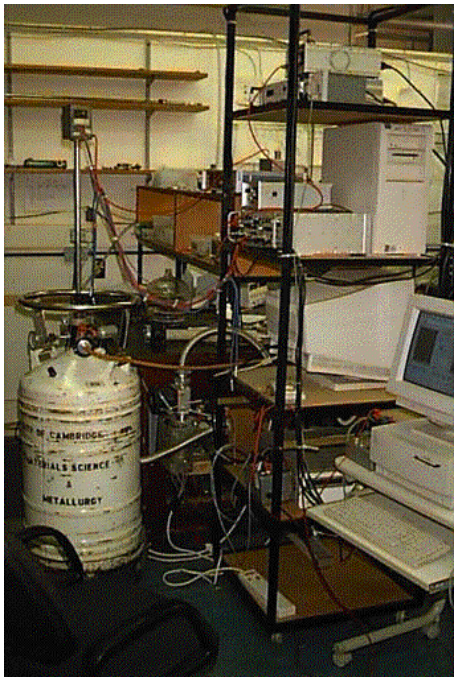

Figure 3.11: Photo of devices rig (courtesy of M. Blamire).

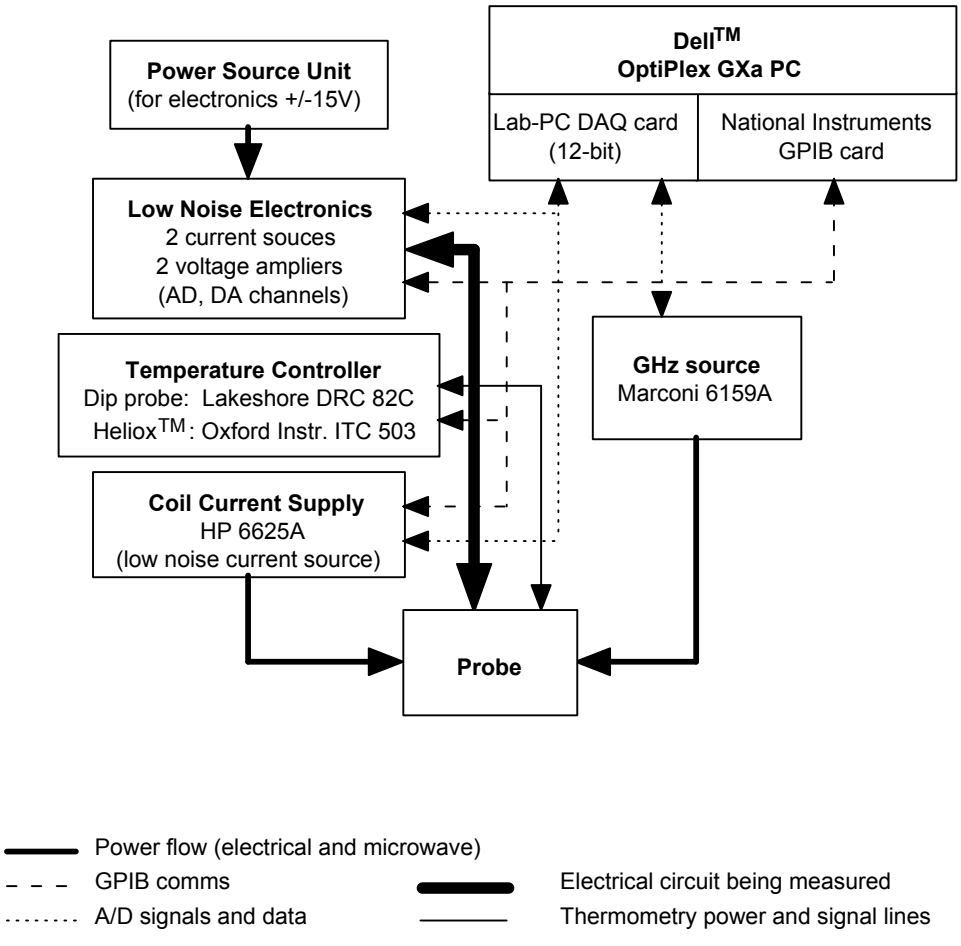

Figure 3.12: Schematic of the devices rig measurement setup (after Moseley 2000).

3.3.2 Dip probe

For the majority of the measurements in this investigation a dip probe constructed by Dr. Wilfred Booij was used. It fits into a standard helium dewar and is of low thermal mass, allowing measurements at 4.2 K and above to be taken quickly and easily. The bottom end of the probe consists of a Cu block to which a resistive wire cartridge heater is attached. Temperature is measured using a Si diode temperature sensor and stabilized using a Lakeshore 82C Temperature controller. The sample chip was mounted using silver dag or nail varnish on a custom designed chip carrier that was attached to the probe by a 19-way D-connector. Electrical connections between the sample chip and the chip carrier were put in place by ultrasonic bonding with 30 μm Al wire. A dipole antenna situated directly above the sample allowed microwave radiation from a Marconi Instuments 6159A source in the range 10-20 GHz to be applied. The output power of the source was calibrated by means of a Schottky diode. A cylinder containing two pairs of Helmholtz coils was placed over the sample on the Cu block. This allowed a magnetic field of up to ~30 mT to be applied either in-plane (*x*-*y* coils) or perpendicular to the plane (*z*-coils). The coils were calibrated at room temperature using a Hall Probe. A mumetal sheath was fitted over the whole assembly, which reduced the ambient field to less that 320 nT at room temperature.

Hence using this probe in conjunction with the 'Dualscope' program and measurement electronics, measurements could be made on devices under controlled conditions of temperature, magnetic field and microwave irradiation.

3.3.3 Adaptation for low-noise measurement

In order to perform low-noise microwave measurements the dip probe with microwave antenna was used with a different set of electronics. A schematic of the measurement setup is shown in Figure 3.13.

The basic setup is similar to that described in Section 3.3.2. The devices are current biased and the voltage and current are measured by standard four-point measurement technique. The low noise current source and voltage amplifiers were designed by Dr. Wilfred Booij. A Dell PC controlled the electronics via a 16 bit National Instruments analogue to digital I/O card. Current-voltage characteristics were measured with LabVIEW software. The software also controlled the temperature controller, lock-in amplifier and voltage source. The computer generated a 30 Hz sinusoidal voltage, which was used to drive the current source. A second current source could be used to drive the magnetic field coils. The output power and frequency of microwave source (Marconi 6159A) was controlled manually.

The EG&G 5302 lock-in amplifier enabled the direct measurement of the differential resistance (or dynamic resistance) versus voltage curves. A 1 kHz voltage with 5 mV amplitude was generated by the lock-in amplifier. This signal was added to a slowly varying voltage ramp generated by the current source power supply by means of an adder box constructed by Dr. Phillip McBrien. The amplitude of the 1 kHz current applied to the device would therefore change depending on the range of the current source. The lock-in measured the amplitude of the voltage across the device at 1 kHz. The differential resistance could then be then be calculated with the knowledge of the current source range and the voltage amplifier gain. Variation of the current source range and voltage amplifier gain were found not to affect the differential resistance measurement. The differential resistance measurement was also not affected by changes in the frequency of the lock-in signal up to ~7 kHz. Above 7 kHz the amplitude of the voltage signal measured by the lock-in was reduced by passive RC low pass filters in the probe.

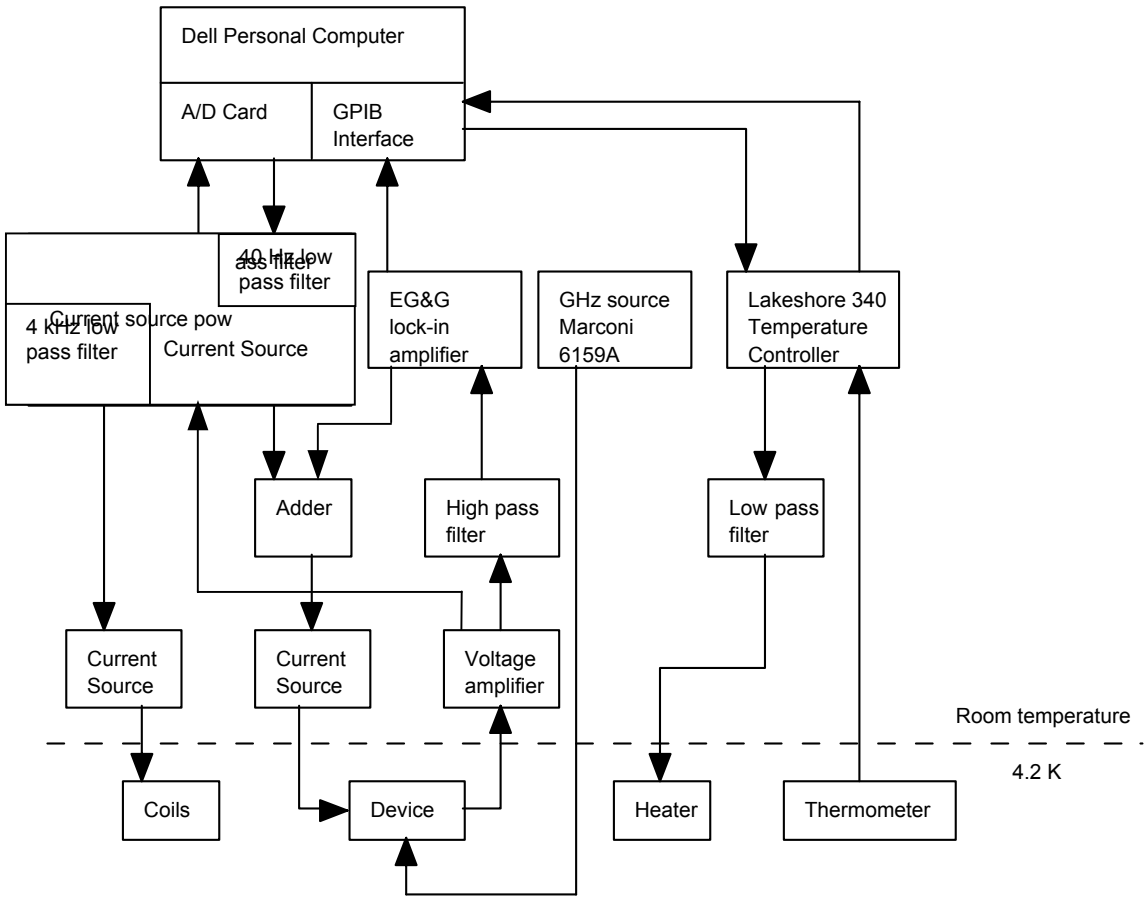

Figure 3.13: Schematic of low-noise measurement setup (after McBrien 2000).

The temperature of the sample was measured with a silicon diode temperature sensor with a Lakeshore 340 temperature controller. The Lakeshore temperature controller and the lock-in amplifier were connected to the computer with a GPIB card.

The peak-to-peak voltage noise of the system was under 1 μV. The following steps were taken to minimize the voltage noise. The current source and voltage amplifier power supply contained active low-pass filters to minimize the voltage noise. The current source and voltage amplifier were fixed to the top of the probe itself. This minimized the length of cable through which low-level signals travelled and thus reduced electromagnetic interference.

3.3.4 Oxford Instruments Heliox^{TM} ^{3}He cryostat

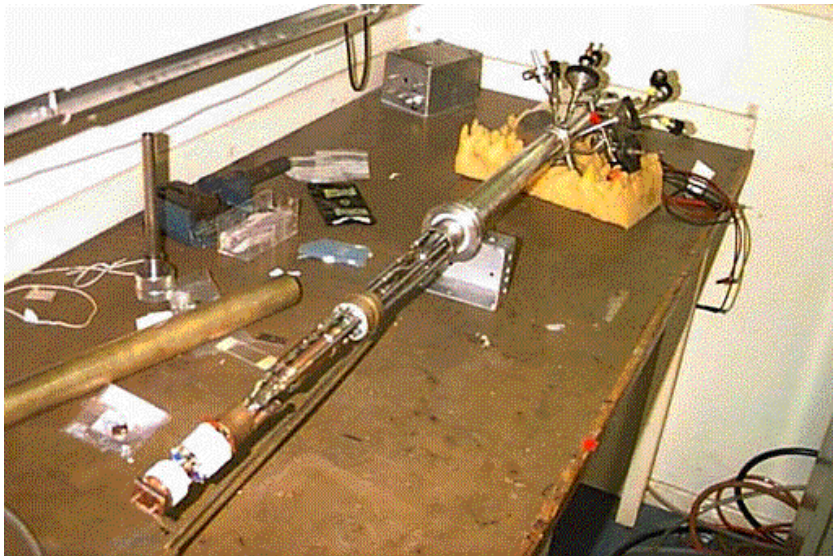

Figure 3.14: Photo of Heliox^{TM} ^{3}He cryostat (courtesy of M. Blamire).

The Oxford Instruments Heliox^{TM} ^{3}He cryostat is designed to fit on a standard helium dewar and allows measurements to be carried out at temperatures down to 300 mK (depending on the heat load). A schematic of the system is shown. It was adapted for use with the devices rig by Dr. Gavin Burnell and Dr. Richard Moseley. The sample is attached to a carrier using either silver dag or nail varnish. The carrier was attached to the probe Cu block and ^{3}He plot by two connecting bolts and a 0.9” dual-in-line socket. The sample is connected to the electronics system via wire bonds from the sample to a printed circuit board on the carrier. The DIL socket is permanently connected via superconducting Nb wires to a D-socket housed in the Heliox^{TM}. A connection port inside the probe is connected by standard copper wiring to a port at the top of the assembly, which allows the signal wires to be connected to the rig electronics. A breakout box containing shielding and feedthroughs that reduce high frequency interference, is mounted directly on the socket. Magnetic coils can be mounted on the probe if required, but were not used in the measurements in this investigation.

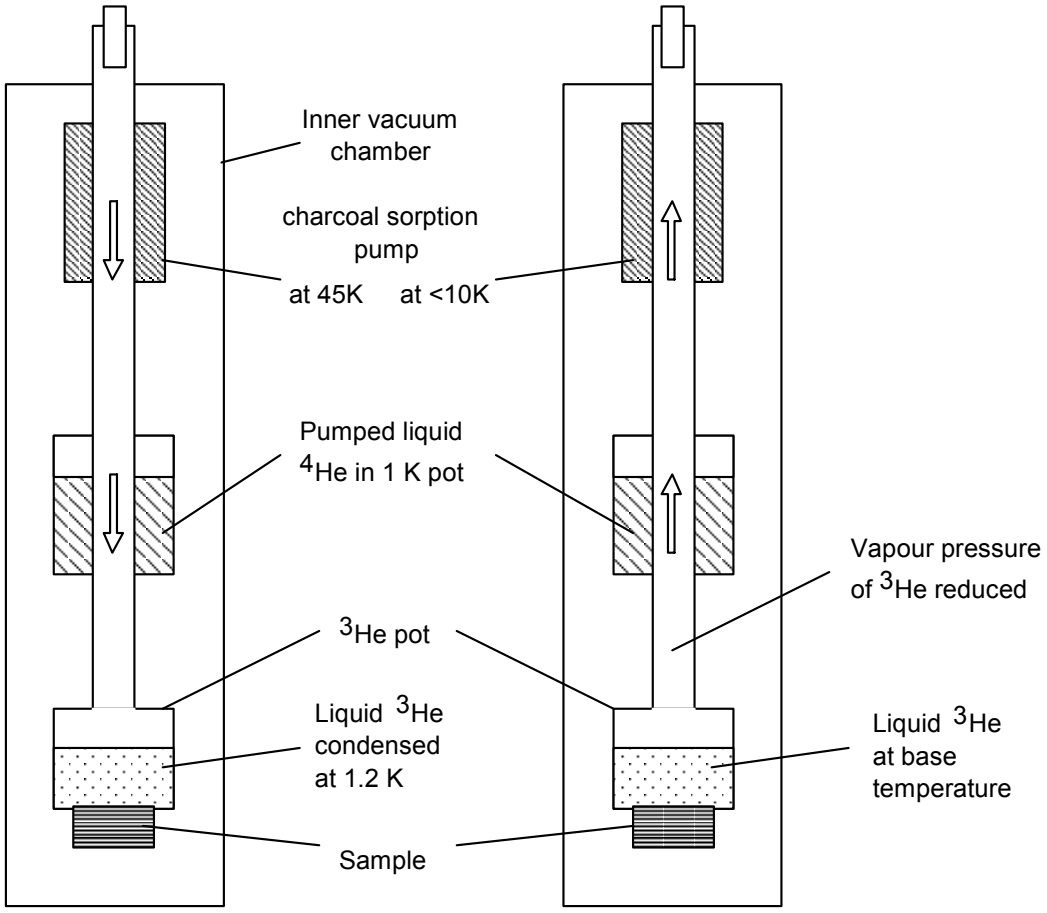

Figure 3.15: The operating principle of the Heliox^{TM} sorption pumped ^{3}He cryostat.

The operating procedure of the Heliox^{TM} can be summarized as follows:

- The sealed sample space is pumped and cooled to 150 K by immersing the whole probe in liquid N_2.
- The probe is then transferred to the helium dewar and cooled by liquid He down to 4.2 K.
- The ^{3}He sorption charcoal is then heated whilst the 1 K pot is being filled constantly with He from the dewar via a capillary and needle valve.
- The 1 K pot is also being pumped by a rotary pump. The result is that the 1 K pot temperature falls and so that the ^{3}He condenses and runs down to the ^{3}He pot on which the sample is mounted.
- The sample can now be cooled to base temperature by ceasing to heat the charcoal sorption pump, which will then start to pump on the ^{3}He (see schematic).

- Temperatures in the range 0.3-1.5 K are achieved by heating the charcoal sorption pump to reduce its efficiency. At higher temperatures control is more complicated. The sample is heated directly by a heater mounted next to the probe holder and indirectly cooled by the 1 K pot.

The entire operation from initial cooling to reaching base temperature takes 3 to 4 hours (the sample chamber should be loaded the evening before and pumped overnight).

Chapter 4: Preliminary Studies

4.1 Previous Experimental Work on SNS Junctions

The first experimental studies of the proximity effect in superconductor-normal metal (SN) bilayers (Hauser 1966) were carried out at the same time as the theoretical work of de Gennes (see Section 2.4.3). The first thorough study of superconductor-normal metal-superconductor (SNS) junctions (in a sandwich geometry) was carried out by Clarke (Clarke 1969) and results were found to be in good agreement with a simplified form of the de Gennes theory. SNS junctions in a sandwich geometry were unsuited for practical applications due to their large cross-sectional area (of order 1 μm^2), leading to unfeasibly large junction critical currents and low normal state resistances. Hence in the early 1970s interest shifted to SNS junctions in a planar variable-thickness bridge geometry, based on a thin film (~100 nm) SN bilayer. A trench was created by patterning a resist film on top of the SN bilayer and etching through the upper superconducting layer (Notarys 1973, van Dover 1981). The difficulty of submicron-scale (electron beam) lithography and the unreliability of the etching procedure made accurate control of the barrier cross-sectional area and length (and hence the resulting junction parameters I_C, $I_C R_N$) impossible. Thus this avenue was largely abandoned in the search for a reliable SNS junction technology. SNS sandwich junctions with semiconductor or magnetically doped metals (Niemeyer 1979) as 'normal' layers were considered more promising alternatives. At present most low T_C Josephson circuits are based on Nb-AlO_3-Nb SIS junctions with resistive shunts (Likharev 1999). Recent reports mention SNS variable-thickness bridges only in the context of novel fundamental studies (Irmer 1999, Dubos 2000).

The acquisition of a Focused Ion Beam microscope (FIB) has enabled our research group to take a fresh approach to the problem of nanoscale variable-thickness bridge fabrication. The FIB allows us to circumvent the problems of deep submicron lithography and anisotropic chemical etching. As described in Section 3.2.5, rectangular-cross section slots of width 50 nm can be milled with ease into Nb up to an aspect ratio of 2.5 (i.e a depth of 125 nm). The early work of Moseley (Moseley 1999, 2000) was carried out using an area dose method to determine the slot depth. A large area of Nb on Cu was milled until such time as the end point detection sensor in the apparatus indicated that the Cu layer was reached; the dose was then scaled for the area of the desired slot. The mill rate was suspected to be slower for a high aspect ratio cut so this method gave overestimates of cutting depth. The development of an *in situ* resistance measuring technique (Latif 2000) has afforded us much greater control of cutting depths (up to ± 5 nm).

4.2 Characteristics of Room Temperature Sputtered Films

Films of Cu and Nb deposited by sputtering (nominally) at room temperature are usually polycrystalline (Barber 1986).

TABLE 4.1:
Characteristics of room temperature sputtered films (T_m = melting temperature, T_d = deposition temperature, Pd = deposition pressure).

Material	T_m (K)	T_d /T_m(max)	P_d (Pa)	Structure
Nb	3041	0.1	0.5-2Pa	Fibrous grains
Cu	1356	0.2	"	Columnar grains

4.3 Resistance versus Temperature Measurements

Qualitatively resistance in normal metals obeys Matthiessen's rule. The resistivity ρ is comprised of two components:

$$\rho = \rho_0 + \rho_i \tag{4.1}$$

At high temperatures resistivity is dominated by electron-phonon scattering ρ_i ($\propto T$) then at low temperatures it tends as T^5 (electron-electron scattering being the dominant scattering mechanism) to a residual resistivity ρ_0 , which is due to electron scattering off impurities and lattice defects. A useful figure is the ratio of the resistance at room temperature to that at 4.2 K (the residual value). This ratio is known as the Residual Resistance Ratio (RRR). For bulk specimens RRR may be as large as 100; for a thin film a value of 10 is very good. For an epitaxial film the mean free path is limited by the thickness of the film. In a polycrystalline film the grain size (which is usually smaller at the interface with the substrate) is the limiting factor. A polycrystalline film may be regarded as a series of layers of improving quality and hence decreasing resisitivity. RRR values for Cu and Nb films of different thicknesses are shown in Table 4.2..

TABLE 4.2:
RRR for different Nb and Cu film thicknesses

Material	Film thickness (nm)	RRR
Cu	25	1.9
Cu	50	3.6
Cu	400	7.7
Nb	125	2.5

4.4 Transmission Electron Microscopy Studies

Valuable information about the microstructure of the films and the profiles of the cuts made with the FIB was obtained by a Transmission Electron Microscopy (TEM) study. The results of this study also demonstrate the validity of the *in situ* resistance measurement technique in determining cut depths. The study of the cross-section of a specific device is only possible with access to a FIB, once again illustrating the tremendous versatility of this instrument. This was carried out with the assistance of Dr. Stephen Lloyd. A series of cuts of increasing depths were made into the tracks on a 125 nm Nb 50 nm Cu chip (Figure 4.1 (a)). The track areas were then covered over with Platinum utilizing the *in situ* localized Pt deposition feature of the FIB (Figure 4.1 (b)). The track used to prepare the final TEM sample was track 2 (top right in both these pictures).

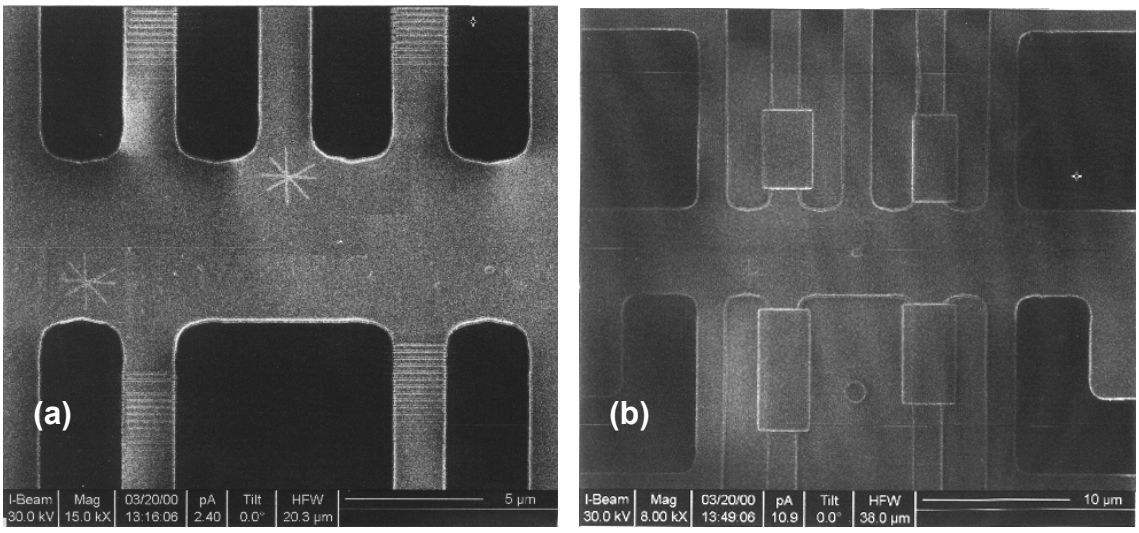

Figure 4.1: FIB images of tracks cut for TEM sample (a) before and (b) after Pt deposition.

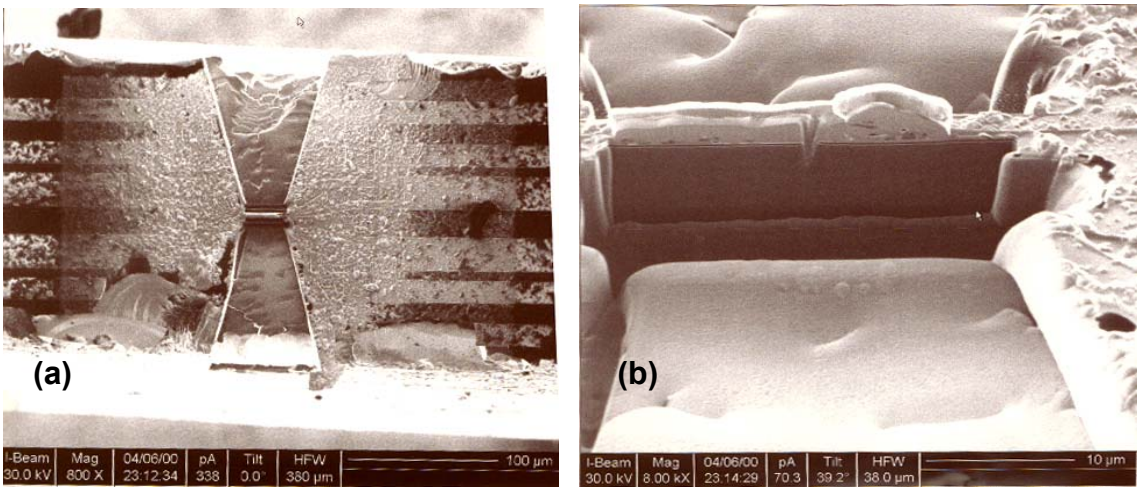

Figure 4.2: FIB images taken during final stages of track thinning for TEM (a) from above and (b) the side.

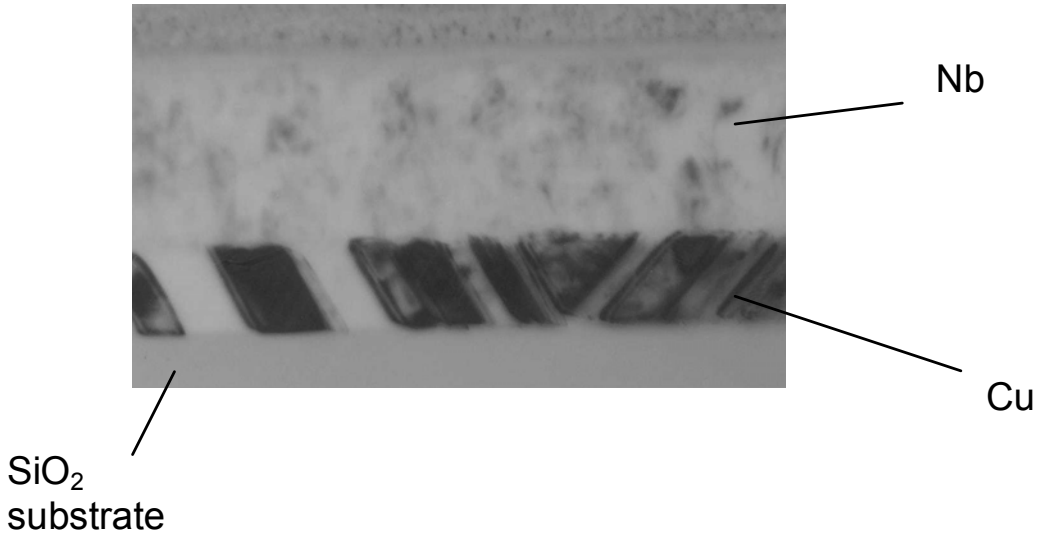

Figure 4.3: Dark field TEM image of a 125 nm Nb 50 nm Cu bilayer.

The area of interest (1 mm × 2mm) was then cut from the chip using a dicing saw and thinned on an abrasive turntable to 0.05 mm × 2 mm. The sample was then mounted in the FIB and the areas of chip on either side of the area of interest were removed by milling on high beam current (Figures 4.2(a) and (b)). The area of track containing the cuts was then thinned using progressively smaller beam currents until a section of thickness ~50 nm remained. It was then possible to carry out TEM studies of the specimen.

The dark field image (Figure 4.3) illustrates most clearly the differing microstructure in the two layers. The columnar stucture in the Cu is clearly visible, with a grain size in the plane of the film of about 30 nm. Here we also see some sort of twin boundary in the polycrystal. The Nb layer above clearly has a much finer grain structure.

The subsequent bright field TEM images show the profiles of the cuts milled in the bilayer track using the FIB. Figure 4.4 shows a series of cuts of increasing mill time (4, 5, 6, 7, 8 s) from left to right. The cut profile is basically rectangular and appears to increase linearly with cutting time. Figure 4.5 shows the next set of cuts in the series, 9 to 13 s from left to right. Here it is clear that once the Cu layer is reached, the milling rate increases markedly (Cu is sputtered faster than Nb). Also, the aspect ratio of the cuts is now greater than 2.5, leading to significant redeposition of material in the bottom of the trench. These two factors mean that the cut cross section begins to taper when the Cu layer is penetrated.

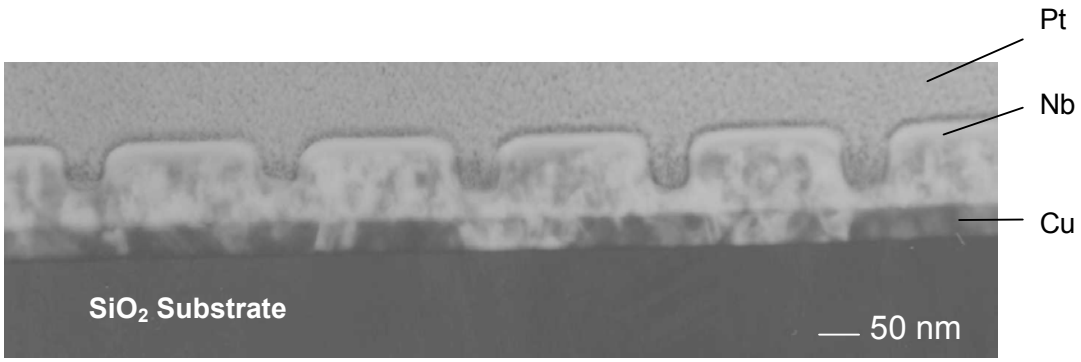

Figure 4.4: Bright Field TEM image of (from left) 4, 5, 6, 7 and 8 s cuts into a 125 nm Nb 50 nm Cu bilayer.

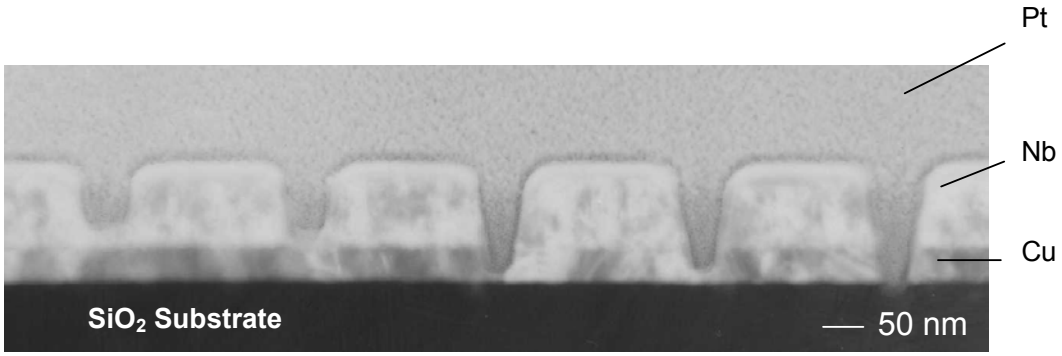

Figure 4.5: Bright field TEM image of (from left) 9, 10, 11, 12, 13 s cuts into a 125 nm Nb 50 nm Cu bilayer.

The local milling rate may depend on the microstructure of the material at that point hence the depth of the cut may vary slightly across the width a track. This effect appears most pronounced in the Cu layer, where the grain size is much larger than in the Nb. Figure 4.6 demonstrates this effect. Figure 4.6 (a) and (b) show 8 and 9 s cuts respectively. These cuts terminate in the Nb. The profiles are basically rectangular but with some unevenness at the bottom. Figure 4.6 (c) and (d) show cuts into and through the Cu layer. There is noticeable damage to the substrate in both these images. In Figure 4.6 (c) this implantation effect occurs even through an appreciable remaining thickness of Cu (≅15 nm). This observation tallys with the calculated stopping distances of 30 keV Ga^+ ions in various materials. The stopping distances in Nb, Cu and Si are 11.3, 9.5 and 25 nm respectively, calculated (Moseley 2000) using the SRIM 2000 Monte Carlo-based program (Biersack 1980). The shorter stopping distances within metallic layers also reflects the fact that these elements are sputtered ~2.5 times faster than Si in the FIB (Kempshall 2001) – this in turn leads to greater susceptibility to redeposition effects when milling metallic films. Hence the maximum aspect ratio for a straight-sided slot achieved here is much poorer than what could be attained when milling Si. Furthermore in this study we are unable to employ the 'enhanced etch' mode of the FIB to improve the aspect ratio. There milling is assisted by the introduction of iodine into the chamber - in Cu films this has the highly undesirable side-effect of forming copper iodide.

In conclusion, the conversion of resistance data to cut depth is based on the assumption that the cut profile is rectangular, as indeed appears to be the case up to an aspect ratio of 2.5. Resistance data was aquired as the initial cuts were milled, and the cut depths observed by TEM were found to be within ±5 nm of those predicted (up to an aspect ratio of 2.5). The TEM images also provide valuable insight into the film microstructure and the extent of Ga implantation at the base of the cuts.

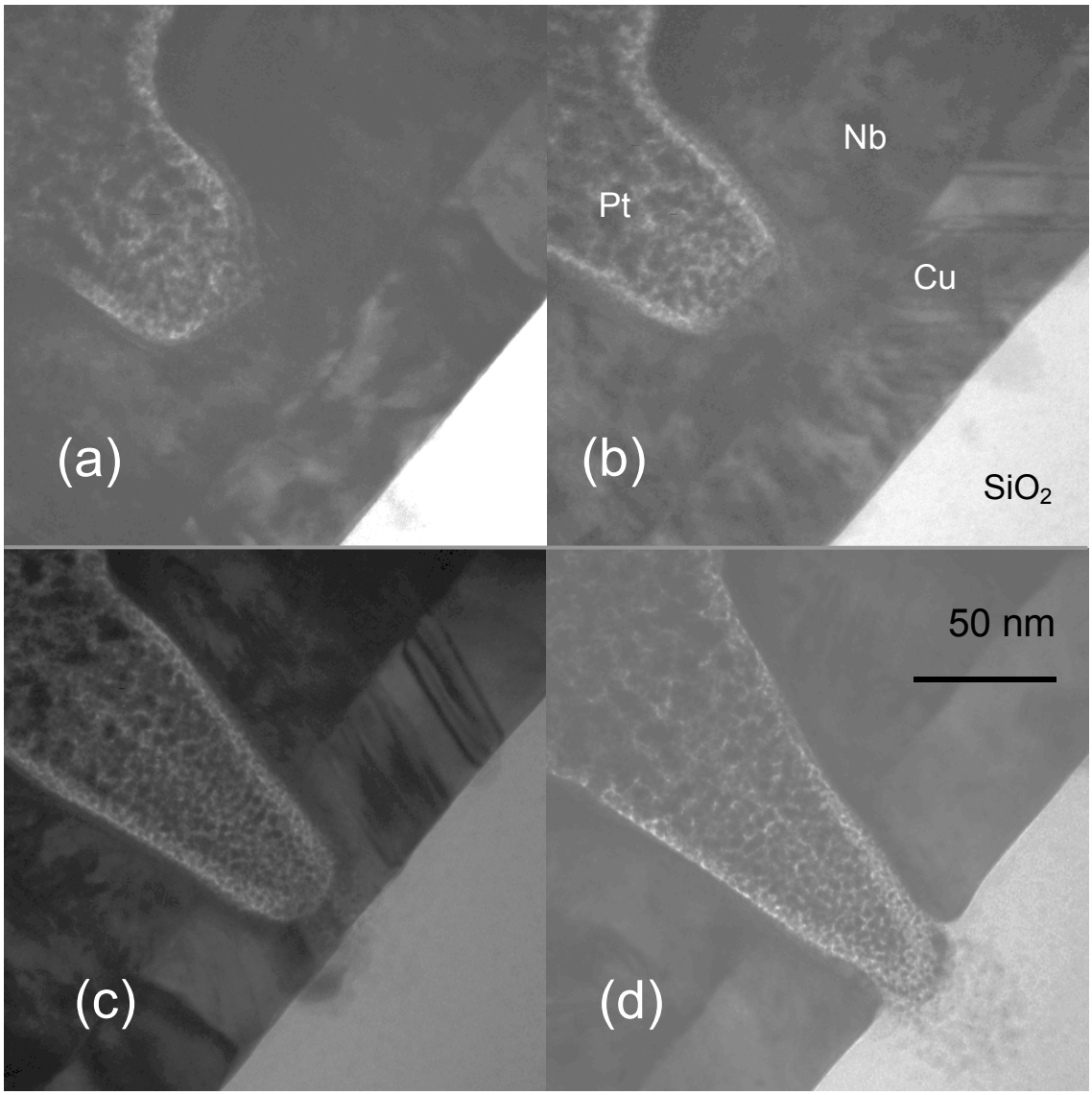

Figure 4.6: Close-up TEM images of various cuts (a) 8 s (b) 9 s (c) 12 s (d) 13 s

Chapter 5: Characteristics of Planar SNS Junctions

5.1 Summary

In this investigation initial devices were made using the *in situ* resistance measurement technique in 125 nm Nb, 75 nm Cu, 1.5 μm wide bilayer tracks, since similar devices fabricated by Moseley had yielded promising results (Moseley 2000). These devices were thoroughly characterized at 4.2 K in terms of their current-voltage *(I-V)* characteristics, magnetic field- and microwave-response. A comparison was made with devices fabricated in 125 nm Nb single layer tracks. A systematic study was then carried out of the effect on the characteristics of devices at 4.2 K of varying the Cu thickness: further devices were fabricated in chips of 125 nm Nb on top of 12.5 nm, 25 nm, 37.5 nm and 175 nm Cu. Using the results of this study a theoretical picture of device operation has been developed. The Heliox^{TM} ^{3}He cryostat allowed *I-V* characteristics for a number of devices to be measured down to 300 mK. The $I_C(T)$ and $I_CR_N(T)$ data thus obtained was compared with established SNS junction theory. The magnetic field response and microwave properties of individual junctions have now been studied in detail. The core results contained in this Chapter have been published (Hadfield 2001a).

5.2 Measurements at 4.2 K

5.2.1 Devices created in 125 nm Nb 75 nm Cu bilayer tracks

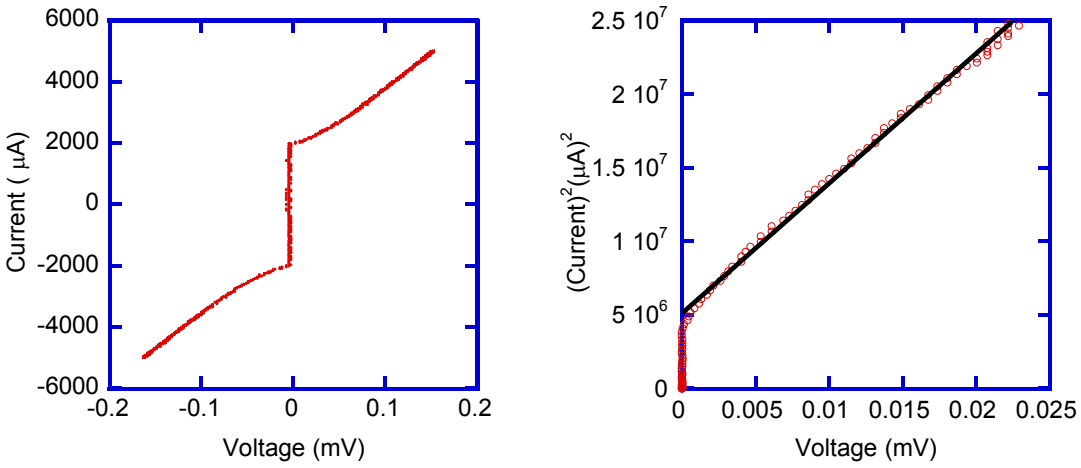

Figure 5.1: Device created in a 125 nm Nb 75 nm Cu track (1.5 μm width) with 6.6 second cut (70% through Nb):low bias characteristics at 4.2 K (a) *I-V* at low bias (b) Plot of I^2 against V^2.

Figure 5.1 (a) shows a typical low bias *I-V* characteristic of a single-junction device fabricated in a 125 nm Nb, 75nm Cu bilayer track. In this case a 50 nm slot was cut for 6.6 s (70% of the way through the Nb layer). At low voltages the junction displays a characteristic of RSJ form (I_C = 1980 μA, $I_C R_N$ = 100 μV). As seen in Figure 5.1 (b), for this set of data $I^2 \propto V^2$, in correspondence with the RSJ prediction (2.40). The normal state resistance R_N of a given device was determined using the best-fit gradient of such a plot. At higher currents, instead of tending to an asymptotic R_N value, the *I-V* characteristic deviates from RSJ behaviour (Figure 5.2). The normal state resistance of the device starts to increase and at a certain bias current value ($I_{C(Track)} \cong$ 7300 μA), the whole track is driven into the normal state resulting in large hysteresis. This sort of behaviour is well known in variable-thickness bridges and is explained in terms of hotspot formation centred on the junction region, as the current is so large as to drive the whole track into a resistive state (Skocpol 1974).

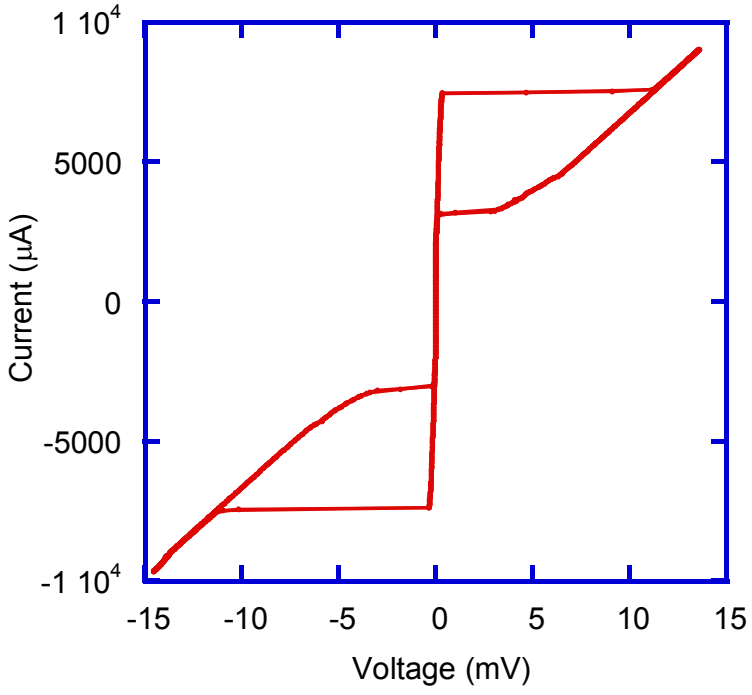

Figure 5.2: *I-V* characteristics of the same device at high current bias. (125 nm Nb 75 nm Cu track 6.6 second cut (70% through Nb)).

The magnetic field response of a single junction device fabricated by a 8.8 s cut into the Nb of a 125 nm Nb 75 nm Cu bilayer is sown in Figure 5.3. The pattern is basically of Fraunhofer type indicating that this junction is in the short limit. A more thorough exploration of the magnetic field response of this type of junction is given in Section 5.4.1.

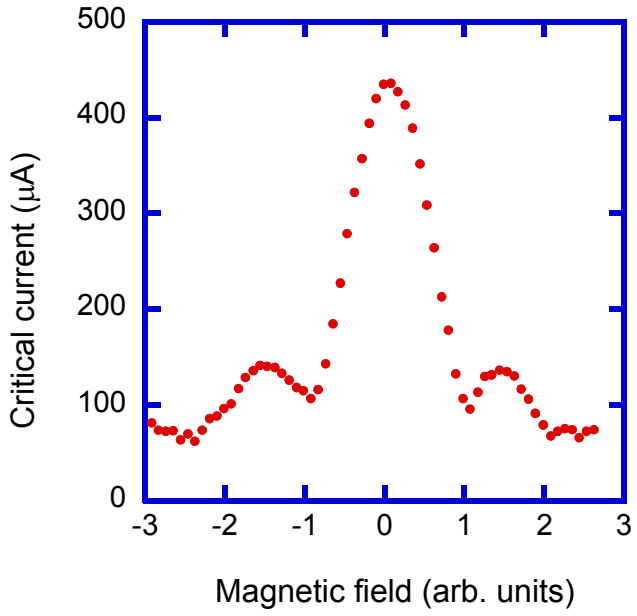

Figure 5.3: Magnetic field response of a junction created by a 9.4 s (90%) cut through the Nb on a 125 nm Nb
75 nm Cu chip measured at 4.2 K.

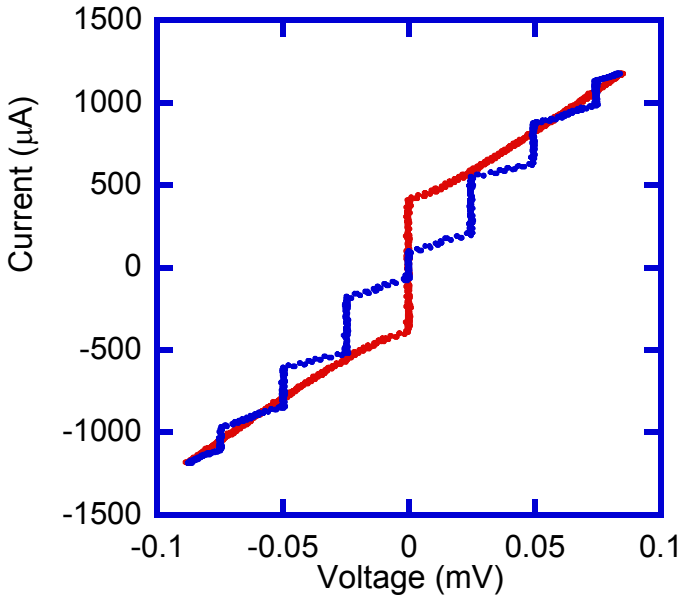

Figure 5.4: The microwave response of a junction created by a 9.4 s (90%) cut into Nb on a 125 nm Nb 75 Cu chip (microwave frequency = 12.05 GHz; reduced frequency Ω~1*)*.

The microwave response of the same junction is shown in Figure 5.4, exhibiting clear Shapiro steps. The measurement setup used here facilitated the calibration of the applied microwave power via a Schottky diode. This allowed the modulation of the step heights with applied microwave power to be measured. Results for the n = 0, 1 and 2 steps are shown in Figure 5.5 and show the expected Bessel function-like behaviour (Ω~1). Non-zero minimum step heights are artifacts of the step height-finding subroutine.

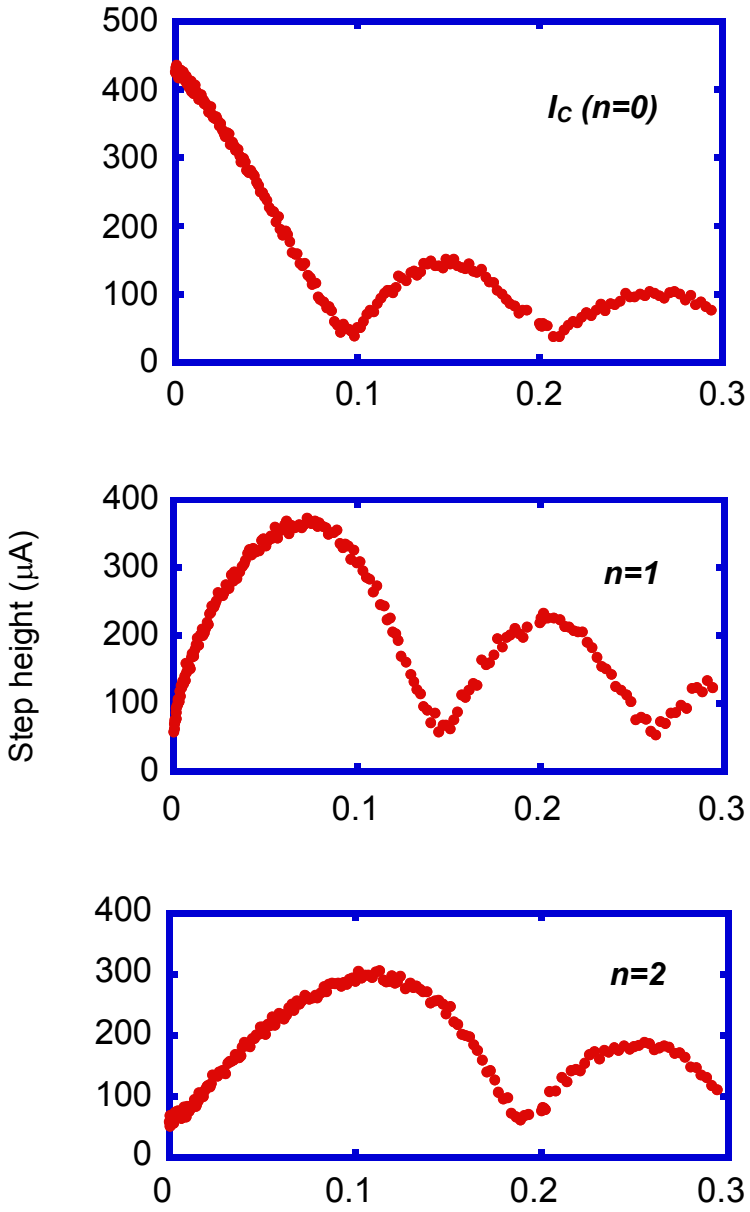

Figure 5.5: Modulation of Shapiro step heights with microwave power for n=0, 1, 2 steps (same device as Figure 5.4; 9.4 s (90%)cut into Nb on 125 nm Nb 75 nm Cu bilayer. Microwave frequency 12.05 GHz.

I-V characteristics at 4.2 K for devices of increasing cut depth (60-90% into the Nb layer) from a single 125 nm Nb 75 nm Cu chip are shown in Figure 5.6 (a). (Measurable I_C 's at 4.2 K were obtained for cuts into the Cu layer, though the exact depth of these cuts was hard to control as the milling rate of Cu is high and the cut cross-section begins to taper – see Chapter 4). The results in Figure 5.6 indicate that at 4.2 K a significant proportion of the Josephson current is passing through the Nb at the bottom the trench: the deeper the cut, the lower the I_C, which is unsurprising as the junction area is being reduced as the cut depth increases. It is interesting to note the behaviour of the I_CR_N product in relation to cut depth for these same devices (Figure 5.6 (b)). There is a steady decrease in I_CR_N with increasing cut depth. This is because the normal state resistance remains more or less the same: in the finite voltage state the quasiparticle current travels through the Cu layer (the normal state resistivity of Cu is much less than that of Nb) which is of equal thickness in all of these devices.

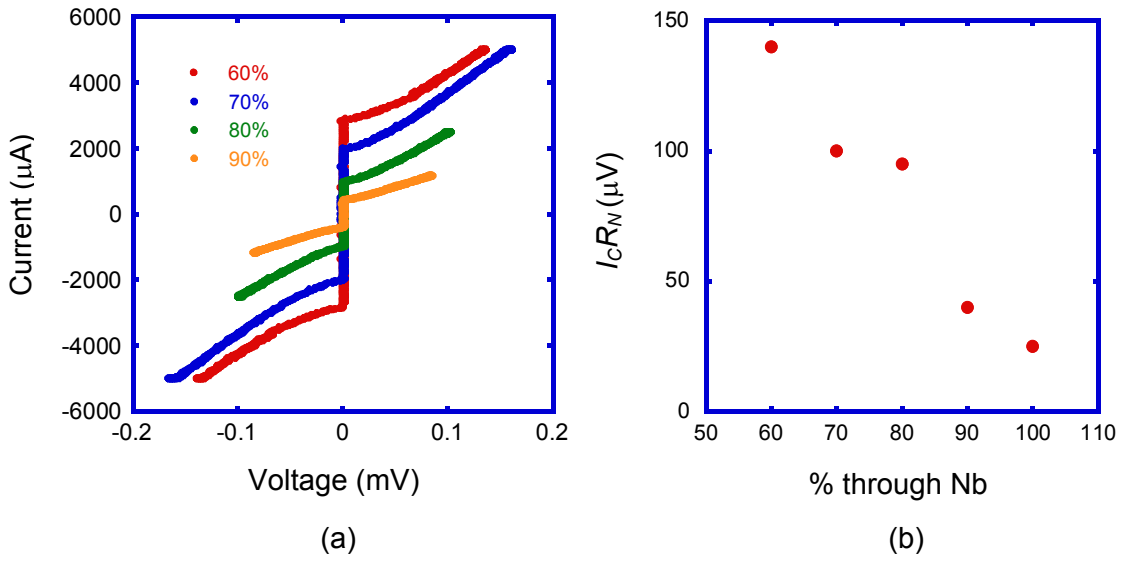

Figure 5.6: (a) Low bias *I-V* characteristics of single junction devices with differing cut depths at 4.2K from a single 125 nm Nb 75 nm Cu chip. (b) I_CR_N product versus percentage cut into Nb for devices from the same 125 nm Nb 75 nm Cu chip. The estimated error in the milling depth is ~5%.

5.2.2 Comparison between devices created in 125 nm Nb 75 nm Cu bilayer tracks and devices created in 125 nm Nb only tracks

Devices were also fabricated by making 50 nm cuts of the same depth into tracks on a 125 nm Nb-only chip. These produced Josephson junction-like *I-V* characteristics at 4.2 K over a much narrower range of cut depths (70-80%). The *I-V* characteristic at 4.2 K of a device fabricated with a 70% cut through the Nb in a 125 nm Nb-only chip is compared with that of a device of identical cut depth fabricated in a 125 nm Nb 75 nm Cu chip in Figure 5.7. The Nb-only device (blue) has a markedly lower I_C (595 μA as compared to 1980 μA) and clearly a much higher R_N (1.6 Ω as compared to 0.05 Ω) than the 125 nm Nb 75 nm Cu device. The *I-V* characteristic of the Nb-only device also shows signs of hysteresis, presumably due to the thermal effects (Nb has a much lower thermal conductivity than Cu). 125 nm Nb devices also showed much poorer magnetic field and microwave response than their 125 nm 75 nm Cu counterparts. A plausible explanation for the poorer performance of Nb-only microbridges is that the device characteristics are determined by a thin (20 to 30 nm) remaining layer of Nb, which is implanted with Ga up to 15 nm through its thickness. Clearly the exact properties of this region are difficult to control. The presence of a Cu layer underneath, in addition to carrying a small proportion of the Josephson current, greatly improves heat dissipation in the region of the junction and allows a much larger I_C to be supported without hysteresis. The only potential drawback of employing a Cu layer is that the R_N of the junction is reduced (a high I_CR_N product being desirable for certain applications).

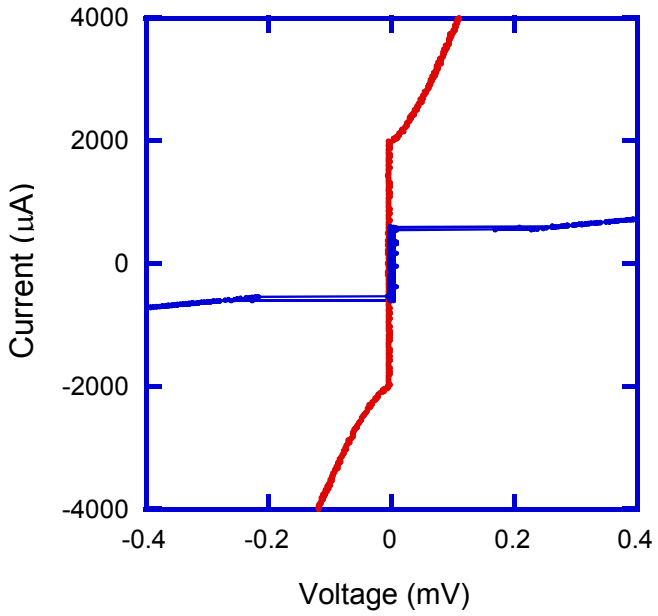

Figure 5.7: The *I-V* characteristics at 4.2 K of a junction created by a 6.6 s cut into a 125nm Nb 75 nm Cu bilayer (70% through Nb – Red – I_CR_N=100 μV) and a cut of equal depth into a 125 nm Nb only track (Blue – I_CR_N =860 μV).

5.2.3 Variation of device properties with Cu layer thickness

A detailed study was carried out of the effect on device properties (R_N, I_C, I_CR_N) of the variation of Cu thickness for a given cut depth. Cu thicknesses from 0 to 175 nm and cut depths from 60-100% through the Nb layer were investigated (a device with zero Cu thickness is a simple Nb-only variable thickness bridge). The Nb thickness remained constant at 125 nm and a 50 nm trench width was always used. Data for 70% cut devices over the full range of Cu thickness is given in Table 5.1. In all cases R_N decreases as Cu thickness increases. The trend in I_C is more complex. The addition of thin layer of Cu results in a dramatic lowering of I_C: as the order parameter at the bottom of the Nb layer is suppressed. I_C falls an order of magnitude below that of a Nb-only variable thickness bridge. As the Cu layer thickness is increased, however, the proximitized Cu layer begins to carry an increasing proportion of the Josephson current. At 175 nm Cu thickness, I_C appears to be approaching saturation, as the film thickness now exceeds the dirty limit coherence length in the normal metal (≅75 nm).

TABLE 5.1:
Variation of device parameters at 4.2 K with Cu layer thickness for 70% cuts through 125 nm niobium layer.

Cu layer thickness (nm)	I_C *(μA/μm)*	R_N*(Ω/μm)*	I_CR_N *(μV)*
0	540	1.6	864
12.5	60	0.85	51
25	46	0.48	22
37.5	320	0.13	42
75	1010	0.044	44
175	1100	0.018	20

TABLE 5.2:
Length scales of importance for Cu layers in this investigation.

Cu thickness (nm)	*Residual resistivity,* ρ_{Cu} *(μΩcm)*	*Electronic mean free path* l_n *(nm)*	*Clean limit coherence length* ξ_{nc} *at 4.2K (nm)*	*Dirty limit coherence length* ξ_{nd} *at 4.2K (nm)*
12.5	6.3	15	450	47
75	1.76	33	450	70
175	0.58	122	450	130

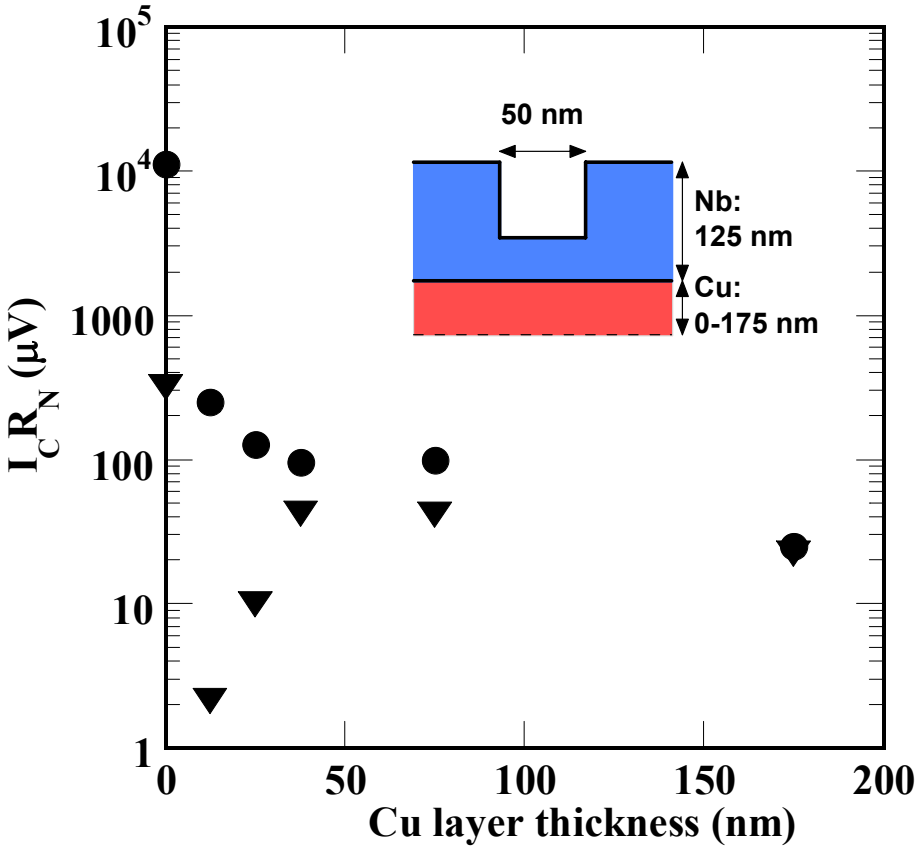

Figure 5.8: $I_C R_N$ at 4.2 K versus Cu thickness for 60% (circles) and 80% (triangles) cuts through 125 nm Nb layer. Inset is a schematic of the device structure (S = superconductor below its T_C, S'= superconductor above its T_C, N = normal metal). Note that the point for the 60% cut at zero Cu thickness does not strictly represent a Josephson junction.

$I_C R_N$ data for 60% and 80% cuts into the 125 nm Nb layer over the full range of Cu thicknesses is shown in Figure 5.8. The initial decrease in I_C and hence $I_C R_N$ is most dramatic for the 80% cut, as the Nb layer remaining at the bottom of the trench is thinner. For the 80% cut, $I_C R_N$ then begins to recover at a Cu thickness of 25 nm, rising to a maximum at around 75 nm Cu. For the 60% cut $I_C R_N$ varies little over this Cu thickness range. As Cu thickness increases further, $I_C R_N$ decreases gently for both cut depths, due to the reduction in R_N with increasing Cu thickness. The data sets for other cut depths (70, 95, 100% - omitted from Figure 5.9 to allow clear representation) follow the trends illustrated by the 60% and 80% sets. A further important point is that for low Cu thicknesses $I_C R_N$ varies considerably over a narrow range of cutting depths: only at Cu thicknesses of 40 nm and above were junction-like properties achieved over a wide range of cut depths (60-100%). Furthermore, a thick Cu layer greatly improves heat dissipation from the region of the junction, allowing devices to support a higher critical current at 4.2 K without thermal hysteresis.

5.2.4 Towards a model of device behaviour

From this data and the calculated length scales in Table 5.2 we can develop a picture of the current transport in these devices: the Josephson current penetrates the Cu layer up to the dirty limit coherence length ξ_{nd}. ξ_{nd} becomes shorter than the film thickness at around 75 nm Cu thickness. Beyond this point we should hence expect little further increase in I_C for a given cut depth. As R_N continues to fall with increasing Cu thickness we should expect $I_C R_N$ to saturate over this length scale, which indeed appears to be the case.

Figure 5.9: Towards a model of device behaviour.

The results of this study lead us to propose a model whereby Josephson current flows in parallel through two interacting channels: the SS'S channel through the damaged and proximitized Nb and the bottom of the trench and the SNS channel through the Cu beneath (S = superconductor below its T_C, S' = superconductor above its T_C, N = normal metal). This situation can also be represented by an order parameter that is inhomogeneous vertically through the centre of the junction (Figure 5.9). The profile of the order parameter Δ along the line y-y' must determine the critical current of the device. A model which allows this profile to be calculated, taking into account the remaining Nb thickness and the thickness of the normal metal layer, relative to the coherence lengths in both materials, would allow variations of I_CR_N with remaining Nb depth (such as shown in Figure 5.6 (b)) to be calculated. In terms of useful applications of these devices, control of device parameters is vital, so a slow variation of I_CR_N with milling depth is highly desirable. To date the slowest variation has been achieved with a thick (~100 nm), clean Cu layer. An outline of an approach to calculating the spatial variation of the order parameter vertically through the barrier, based on microscopic Usadel theory (Usadel 1970) is given in Appendix 1.

5.3 Temperature Dependent Measurements

Measurements were carried out of I_CR_N over a more extensive temperature range for selected devices in order to investigate the behaviour of the two interdependent transport channels. In order to study the SS'S channel in isolation, a device created by an 80% cut through a 125 nm Nb-only track was chosen. A fit was made to this Nb-only microbridge data using a theory of de Gennes (de Gennes 1964 – Section 2.4.3). Substituting the value of the electronic mean free path in Nb (l_n = 5 nm, calculated from the residual resistivity) into Equation 2.31 gives an effective junction length L_{Eff} = 400 nm (i.e. long compared to the width of the trench). It should be noted however that measurements were only possible over a limited temperature range due to poor heat dissipation from the region of the junction.

TABLE 5.3:
Summary of parameters used for fitting with Likharev model

Cu thickness (nm)	*Electronic Mean free path l_n (nm)*	*T_c (device) (K)*	*$\xi_{nc}(T_c)$ (nm)*	*$\xi_{nd}(T_c)$ (nm)*	*$I_CR_N(T\rightarrow 0)$ (measured) (μV)*	*$L_{Eff}/\xi_{nd}(Tc)$*	*$I_CR_N(T\rightarrow 0)$ (Likharev prediction) (μV)*
75	33	7.5	250	52	270	5	980
175	122	6.5	290	108	140	8	550

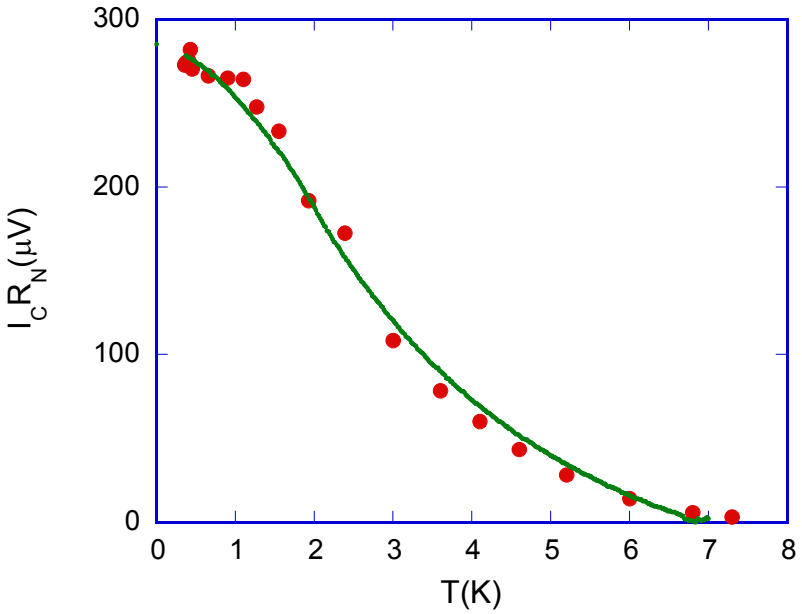

Figure 5.10: $I_C R_N$ measured as a function of temperature for a 100% cut through the Nb layer in a 125 nm Nb 75 nm Cu track. The fit is made using the Likharev one-dimensional-electrodes-in-equilibrium theory for $L/\xi_N = 5$. With normal metal dirty limit coherence length at 4.2 K $\xi_N = 45$ nm, the effective junction length L is 280 nm.

The SNS channel was measured by selecting devices where the Nb layer was cut completely through. A numerical fit to the data was carried out using the one-dimensional-structure-with-electrodes-in-equilibrium theory (Likharev 1976 – Section 2.4.4). Table 5.3 shows the parameters used in the fit for two devices. In Figure 5.11 $I_C R_N(T)$ for a 100% cut device in 125 nm 75 nm Cu bilayer is shown. This gives an effective junction length L_{Eff} of 280 nm. This value seems plausible, envisaging the Josephson current entering the Cu at some average distance into the Nb banks. The absolute value of $I_C R_N$ is 4-5 times lower however than that predicted by the theory, given the value of the gap in Nb (1.3 meV - Warburton 1993). This can be explained in by the suppression of the gap in the Nb in the region of the SN interface. Suppression of the order parameter in the superconducting banks is not taken into account in the Likharev hard boundary condition model, nor is an imperfect interface transparency at the SN interface. These would both lead to the effective order parameter appropriate for substitution in the Likharev model being much less than the ideal value. These arguments were applied by van Dover (van Dover 1981) to results on variable thickness bridges similar to those fabricated in this study in order to fit $I_C R_N(T)$ data. Van Dover multiplied the Likharev $I_C R_N$ predictions by temperature dependent prefactors given representing the suppression of the order parameter and the imperfect interface transparency. The result was a

reasonable fit but with unclear physical justification: the reliability of the fit depends on a factor γ which represents the ratio of the effective mass of a charge carrier in the normal metal to that in the superconductor. This must be far from unity to give a sensible value for the interface transparency.

Hence to date theoretical fits have only been made successfully to temperature dependent data from devices that are either purely SS'S or SNS. In general, as discussed in Section 5.2.4, the devices are two-dimensional in nature and consist of two interdependent transport channels (which can be viewed as an order parameter that is inhomogeneous vertically through the centre of the junction).

5.4 Departures from Ideal Behaviour

5.4.1 Magnetic field response

The basic magnetic field response of a Josephson junction is explained in Section 2.4.5. When the self-field of the current through the junction can be neglected the $I_C(B)$ response is analogous to the diffraction of monochromatic light through a single slit in the Fraunhofer regime (the 'short' limit). Self-field effects become significant in the 'long' limit, when the junction width exceeds the Josephson penetration depth λ_J (Equation 2.35).

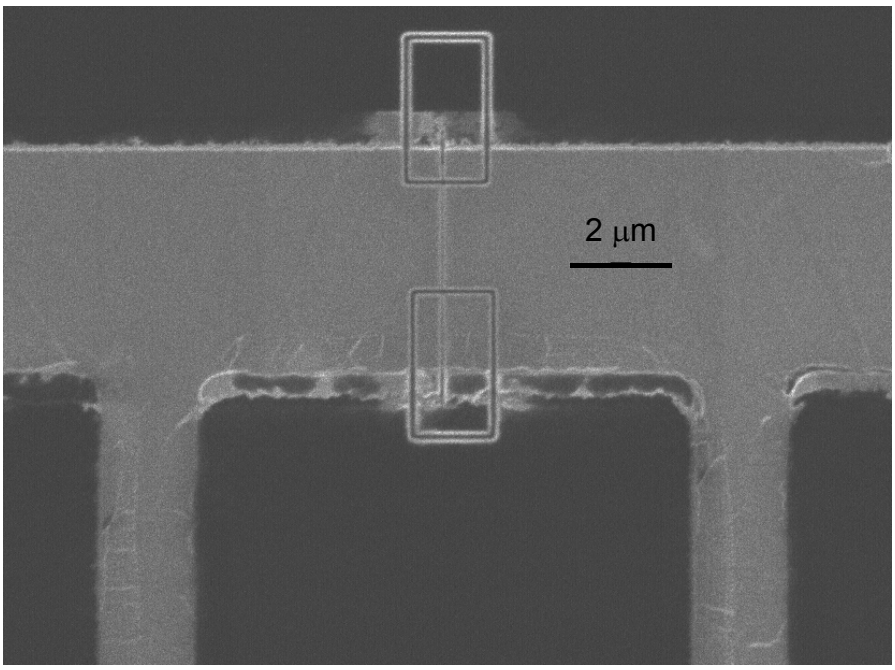

Figure 5.11: FIB image of a 2 μm width junction (80% through Nb) layer. Note the barrier width is defined by isolation cuts milled with a 70 pA beam.

To explore the transition from 'short' to 'long' behaviour junctions of several widths (0.5, 1, 2 and 4 μm) and depths (70% -100% through Nb) were fabricated in a single 125 nm Nb 75 nm Cu chip. The chip was of the type provided by NIST (See Chapter 6) consisting of a long central track (up to 8 μm width) with numerous narrower lines branching off. The milling depth for a 50 nm trench with a 4 pA beam was calibrated using the *in situ* resistance measurement. After trench milling, junction widths were defined using a 70 pA beam (Figure 5.11). To avoid creating excessive debris (which could lead to back-filling of the junction trench), islands of isolated superconducting material were left either side of the actual junction.

Figure 5.12 shows $I_C(B)$ responses of junctions of 70% and 80% milling depth. The $I_C(B)$ is extracted using a 5 μV voltage criterion. The 70% trace (red) exhibits close to a sinc-function (Fraunhofer) response; the incomplete suppression of I_C at the first minimum may be attributed to inhomogeneities in the barrier and the use of a voltage criterion. The first minimum corresponds to one flux quantum Φ_0 linking the junction. The 80% trace (blue) measured in the same field, shows a first minimum where I_C is clearly <u>not</u> suppressed. This indicates we are approaching the long limit, where the $I_C(B)$ pattern is more correctly viewed as a superposition of triangles (Section 2.4.6 - Waldram 1996).

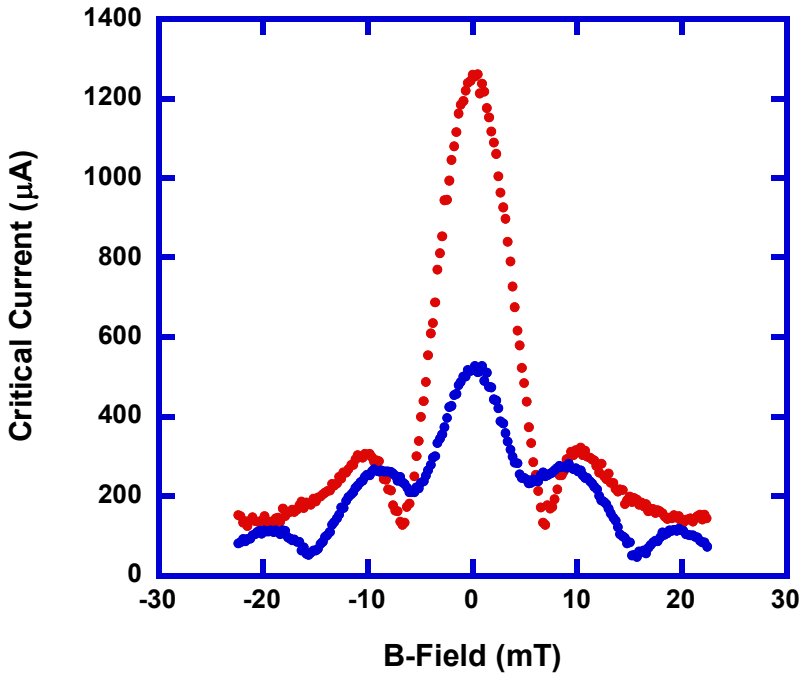

Figure 5.12: Critical current versus applied field response for 1 μm width junctions (Red: 70% cut; blue 80% cut).

TABLE 5.4:
Parameters used in calculating Josephson penetration depth, λ_J for the 1 μm width junctions of Figure 5.12 assuming a uniform current density J_C throughout the remaining Nb-Cu bilayer

Milling depth (%)	*Remaining depth of material (nm)*	*Critical current (μA)*	*Current density J_C (Am^{-2})*	*Thin film penetration depth λ_p (nm)*	*Barrier thickness d'(nm)*	*λ_J (nm)*
70	112.5	1260	1.12×10^{10}	65	180	360
80	100	525	5.25×10^{9}	65	180	525

Hence from Figure 5.12 we can infer that λ_J is typically under 1 μm (depending on milling depth) – clear long junction behaviour is only expected when junction width $w >> \lambda_J$. For comparison λ_J is calculated for these two devices using Equation 2.28. The parameters used are shown in Table 5.4. The current density J_C is calculated by simply assuming the current is uniformly distributed through the remaining Nb and Cu thickness. The thin film penetration depth is $\lambda_p = \lambda_L^2/t$ where λ_L is the London penetration depth and t the superconducting film thickness (125 nm). Inductive measurements of Nb thin films grown in this laboratory put λ_L ($T = 0$) at 90 nm (Schneider 1994). The effective barrier thickness *d'* is the trench width, *d*, plus twice the penetration depth. Surprisingly the 80% depth junction yields the longer λ_J (525 nm compared with 360 nm for the 70% depth junction). In Figure 5.12 the 80% is clearly closer to the long limit (implying a *shorter* λ_J). The discrepancy may arise from the estimate of J_C - as discussed in Section 5.2.4 J_C is in fact liable to be inhomogeneous through the depth following the same dependence as the order parameter Δ in Figure 5.9 (highest in the remaining Nb layer and falling off in the Cu layer with distance from the SN interface). Furthermore a thin layer of Nb in the bottom of the trench (~10 nm) is degraded by Ga implantation. The recalculated values of λ_J are given in Table 5.5. In this case λ_J for the 80% depth device is only slightly longer (203 nm as opposed to 177 nm for the 70% device).

TABLE 5.5:
Parameters used in calculating Josephson penetration depth, λ_J for the 1 μm width junctions of Figure 5.12. assuming majority current transport through the remaining Nb layer.

Milling depth (%)	*Remaining depth of Nb (nm)*	*Critical current (μA)*	*Current density J_C (Am^{-2})*	*Thin film penetration depth λ_p (nm)*	*Barrier thickness d'(nm)*	*λ_J (nm)*
70	27.5	1260	4.58×10^{10}	65	180	177
80	15	525	3.50×10^{10}	65	180	203

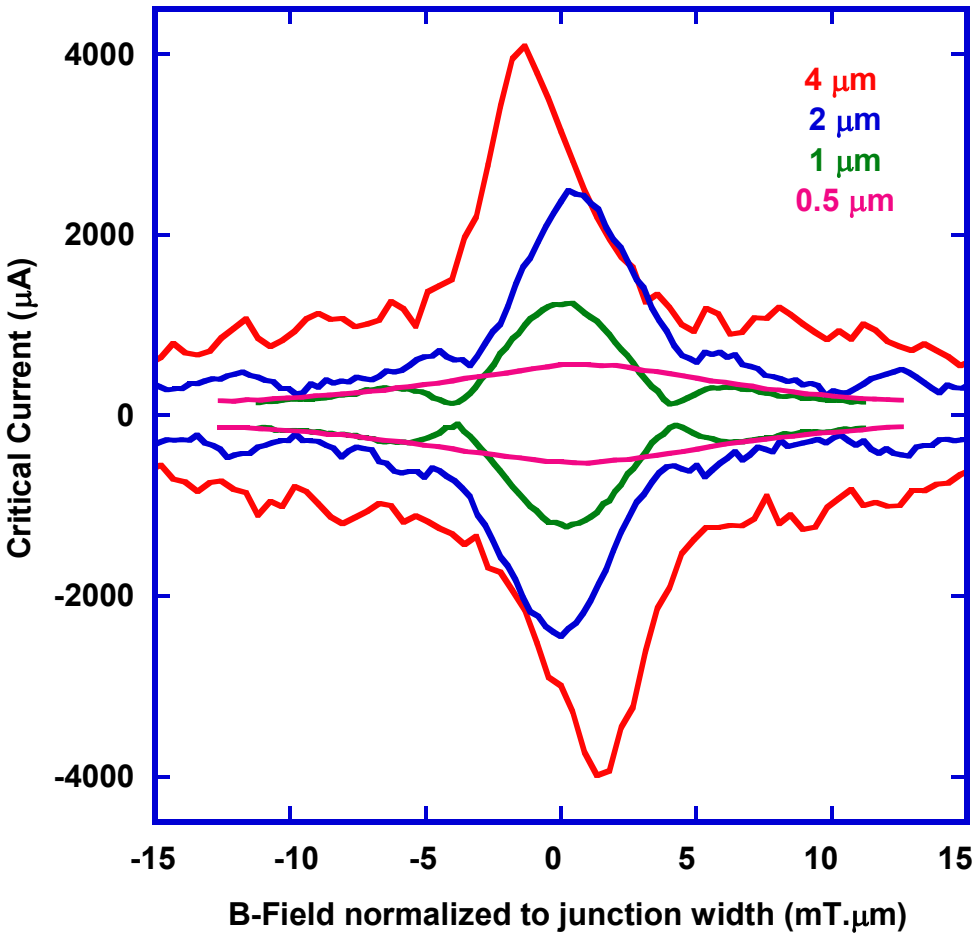

Figure 5.13: Transition from 'short' to 'long' junction behaviour with increasing junction width in 70% cut depth devices. $I_C(B)$ patterns measured at 4.2 K (B-field normalized to track width). Track widths indicated.

Figure 5.13 shows the evolution of $I_C(B)$ for 70% cut junctions of width 0.5 to 4 μm. For clarity, magnetic field is normalized to junction width. I_C is unscaled and so increases with junction width. For the narrowest junctions (0.5 μm width) the full period of the pattern was difficult to obtain, as a greater flux density is required. It is clear that the pattern evolves from sinc-like (0.5 and 1 μm width) to clear long junction type (4 μm), suggesting that $\lambda_J < 1$ μm is a good estimate for these 70% cut depth devices. I_C for the 4 μm width device is noticeably less than the 2 μm width device, indicating that self-field effects are limiting I_C in the long limit. It should also be noted that the patterns for 2 and 4 μm width devices are considerably less clean, indicating increasing barrier inhomogeneity. The asymmetry evident in the 2 μm and 4 μm traces is due to self-field effects arising from the current injection configuration: the current is being driven in a 'U'-shaped path (see Figure 5.11), so a component of the current flows parallel to the barrier (Isaac 1998).

An obvious further question is whether the effective magnetic area of the junctions can be extracted from the $I_C(B)$ data. The usual result for a Josephson junction is that the period of the magnetic field modulation $\Delta B = \Phi_0 / [w(2\lambda_L + d)]$ where w is the junction width, d is the trench width and λ_L is the London penetration depth. For a planar junction in the thin film limit (thickness ~ λ_L or less) flux penetrates the film uniformly and ΔB varies as $1/w^2$ (Rosenthal 1991). This limit is most commonly achieved in junctions based on high T_C materials, where λ_L is long. The planar SNS junctions used in this study are based on polycrystalline Nb films 125 nm thick. As mentioned the best available figure for λ_L is 90 nm (Schneider 1994). Hence with these devices we may expect to be at the crossover between the $1/w$ and $1/w^2$ regimes. Figure 5.14 shows ΔB (half width of the central peak) versus w. For both milling depths studied, the best fit power of w is close to 1.5 indicating that we are in the intermediate regime (thickness ~ λ_L). However, as we enter the long junction regime the analysis may be argued to be invalid. Without the 4 μm width data the best fit power is 2 indicating we are in the thin film limit and flux focusing is taking place. Some studies of flux focusing (Pauza 1993) suggest that for a junction in a thinned track, the appropriate scaling is in fact $1/w_{Track}.w_{Junction}$. In this experiment it is difficult to verify this type of dependence as the data set is small and the geometry is not exactly the same: the presence of the isolated superconducting regions either side of the junction (Figure 5.11) may distort the result.

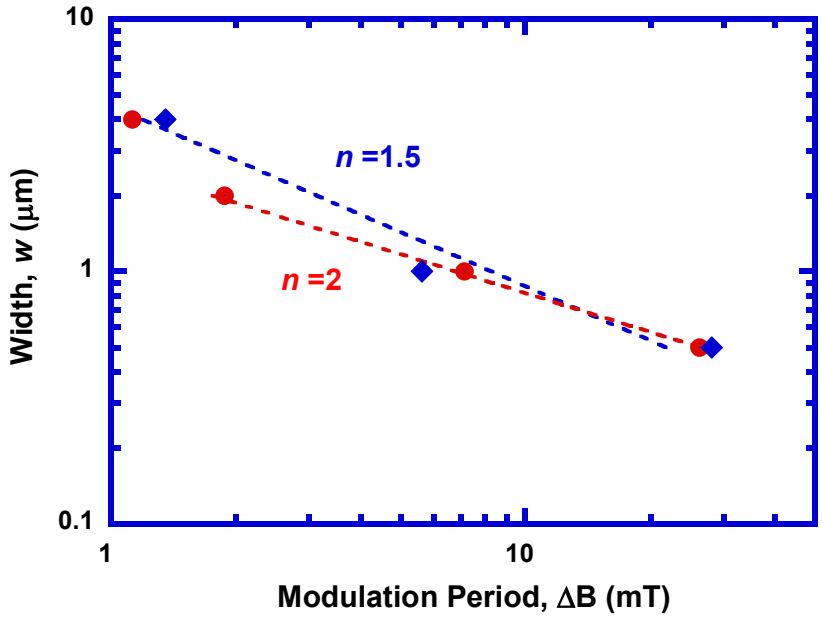

Figure 5.14: Plot of junction width w versus modulation period ΔB for 70% (red circles) and 80% cuts (blue diamonds). A power law fit $\Delta B \propto 1/w^n$ gives n=1.5 for the full range (blue line) and n=2 discarding the 4 μm width junction data (red line).

5.4.2 Microwave response

The development of an improved low-noise measurement setup (Section 3.3.3) has allowed deviations from RSJ-like behaviour in the junction *I-V* characteristics to be studied. The *I-V* characteristic at 4.2 K of a single junction is shown in Figure 5.15. The device was fabricated in a 125 nm Nb 75 nm Cu bilayer provided by NIST (see Chapter 6).

Two features are striking about the *I-V* characteristic:

(a) Without microwaves (red curve)

There appears to be a definite 'shoulder' at 0.03 mV, which is not in agreement with the RSJ model (which predicts a hyperbola: Equation 2.31).

(b) With microwaves at 13.95 GHz (blue and green curves)

At moderate microwave power (blue curve) there are strong Shapiro steps at the expected voltages (first step at ~0.028 mV). However as microwave power is increased further (green curve) half-integer Shapiro steps become evident.

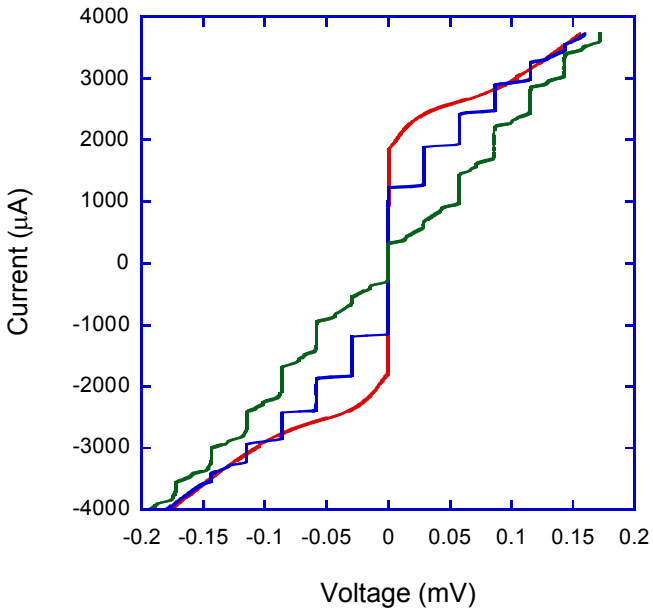

Figure 5.15: *I-V* characteristic of a single junction in a 125 nm 75 nm Cu bilayer at 4.2 K. Red curve: without microwaves. Blue and Green curves: with increasing microwave power at 13.95 GHz.

The 'shoulder' feature in the *I-V* characteristics of planar SNS junctions has been reported elsewhere (Lindelhof 1981) and is ascribed to non-equilibrium processes, which cause a gap oscillation (Lempitskii 1983). The evolution of this feature with temperature has also been studied (Dubos 2000/2001- Figure 5.16). The structure concerned was a long Nb-Cu-Nb junction with a barrier length of 800 nm. At low temperatures the *I-V* characteristic of the device is RSJ-like but as temperature is increased the 'shoulder' feature becomes more and more apparent. This transition takes place over quite a small temperature range (3.5 – 5.5 K; T_C Nb electrodes = 8 K). Hence the reason why this feature is not so obvious in the devices discussed in the previous sections of this Chapter is that the Nb-Cu bilayers provided by NIST have slightly lower T_C than those produced in Cambridge.

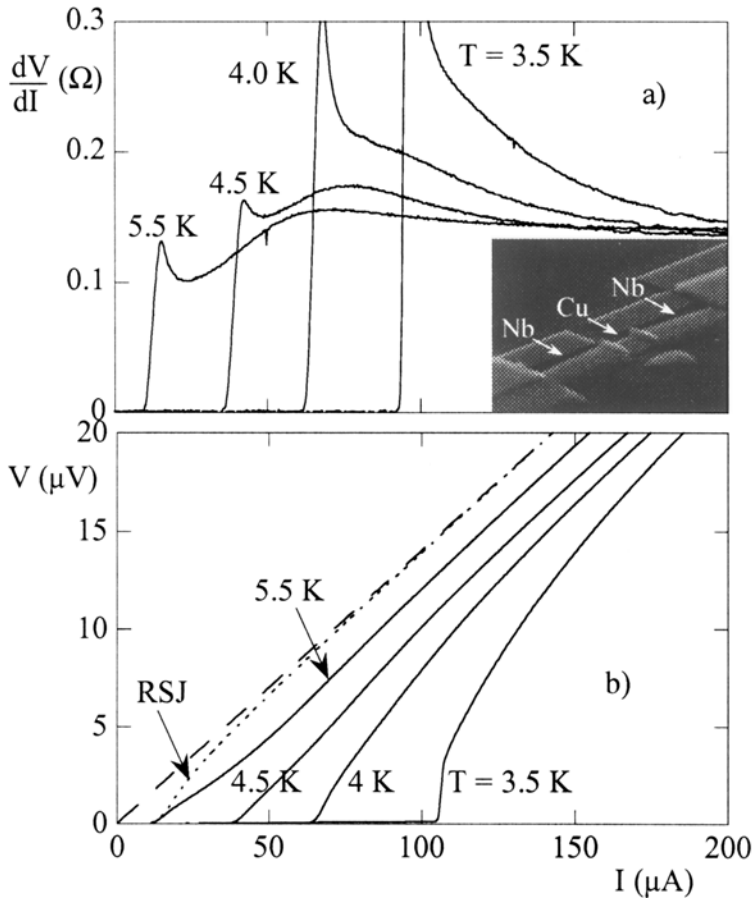

Figure 5.16: (a) Differential resistance of a Nb-Cu-Nb device as a function of dc bias current at different temperatures. Inset: Electron micrograph of device. (b) Current-voltage characteristics as obtained by numerical integration of differential resistance curves. Also shown is an RSJ fit to the data at 5.5 K (dotted line) and ohmic behaviour (dashed line). (Dubos 2001)

More sophisticated theories than the RSJ model can be employed to obtain an improved fit to the *I-V* characteristics of planar SNS junctions. Time-Dependent Ginzburg Landau theory (TDGL) was applied with some success to this problem by van Dover and co-workers (van Dover 1981, de Lozanne 1986). More recently SNS *I-V* characteristics have been simulated theoretically within the framework of quasiclassical Green's functions (Dubos 2000, Wilhelm 2000).

Sub-multiple Shapiro steps have been observed since the earliest SNS junctions were fabricated (Waldram 1970). The explanation usually offered is an additional $\sin(2\varphi)$ term in the current-phase relation (Equation 2.17) – which can again be ascribed to a non-equilibrium current. In the case of long barrier SNS junctions experimental observations of sub-multiple steps (Dubos 2000) have been found to be in good agreement with Usadel-based microscopic theory (Wilhelm 2000). The sub-multiple steps are found to persist at high temperatures even when the dc Josephson current is zero. Hence although the junctions discussed in this Chapter are two-dimensional in nature it is clear that the features observed are in keeping with more idealized SNS experimental systems.

5.5 Conclusion

In this Chapter the results of careful electrical measurements on single superconductor-normal metal-superconductor (SNS) junctions fabricated by the focused ion beam (FIB) have been presented. The goal of this study was to assess the reproducibility of this technique and the range of junction parameters that could be attained. Insofar as was possible, device behaviour was compared with established SNS theory, with a view to gaining insights which would allow us to improve the performance of future devices.

As shown in Chapter 4, the *in situ* resistance measurement technique allows us to control milling depths of 50 nm wide trenches to within 10 nm. Here, the trench depth has been shown to be the decisive factor in determining device characteristics. It has been shown conclusively that the Nb remaining in the bottom of the trench carries a significant part of the Josephson current, whilst the Cu layer beneath carries the quasiparticle current in the finite voltage state and provides effective thermal dissipation from the region of the junction. The investigation of the effect of Cu thickness variation allows device parameters to be tuned to a high level of accuracy and has allowed progress to made towards a theoretical model of device operation (see also Appendix 1). It has been shown that junctions with non-hysteretic *I-V* characteristics at 4.2 K and cut depth-tunable $I_C R_N$ can best be obtained with a thick

(>40 nm) Cu layer. In this range $I_C R_N$ is maximized by limiting the Cu thickness so that it is comparable to the bulk dirty limit coherence length of the normal metal; I_C is maximized by having sufficient normal metal present to augment Josephson current transport without excessively degrading R_N.

The two-dimensional device architecture, although convenient from the point of view of fabrication, makes exact quantitative analysis in terms of conventional (one-dimensional) SNS junction models difficult. However the observed behaviour is in excellent *qualitative* agreement with the established canon. The temperature dependence of $I_C R_N$ for selected devices has been studied and corresponds well to that expected from established SNS theory. A study has also been carried out of the device magnetic field response over a range of junction widths, allowing the transition from 'short' to the 'long' junction behaviour to be observed (the Josephson penetration depth λ_J is typically under 1 μm). As the thickness of the films used is of the order of the penetration depth, flux focusing effects are observed in these junctions. Finally, a new low-noise measurement setup has allowed departures from RSJ-like behaviour in the *I-V* characteristics and novel features of the microwave response of this type of junction to be studied.

In conclusion it has been demonstrated that SNS-type Josephson junctions can be fabricated with ease using the focused ion beam (FIB). The FIB-based fabrication technique affords us a high degree of control over the resulting device parameters and the junction properties are in good qualitative agreement with established SNS junction theory.

Chapter 6: Nanofabricated Series Arrays of SNS junctions

6.1 Introduction

6.1.1 Josephson voltage standards

As described in Section 2.5.2, a microwave signal applied to a Josephson junction gives rise to so-called Shapiro steps in the current voltage (*I-V*) characteristic by phase-locking with the internal Josephson oscillations. If a microwave signal is applied to a series array of *N* identical Josephson junctions, the first Shapiro step (Section 2.5.2) will appear at a voltage

$$V = N\frac{h}{2e}f_{HF}, \tag{6.1}$$

where f_{HF} is the microwave frequency. Hence *N* and f_{HF} can be chosen to give a particular voltage for the first step. The accuracy of this voltage depends only on the precision of the frequency source. Current primary voltage standards are based on the dc operation of series arrays consisting of large numbers of SIS tunnel junctions (e.g. 20,208 Nb-AlO_x-Nb Josephson Junctions for operation in the range –10 V to +10 V (Hamilton 1992, 1997)).

6.1.2 Programmable voltage standards

SIS junction arrays are however poorly suited to time dependent tasks, such as generation of a calibrated sine wave. In a programmable voltage standard binary subdivisions of the overall array are biased at the –1, 0 or 1 step to achieve the desired output voltage (Figure 6.1). The junctions must be non-hysteretic to permit rapid resetting. In addition, a high critical current (~5 mA) is required to provide noise immunity. SNS junctions in a sandwich geometry (Nb-PdAu-Nb; Area ~1 μm^2) have been used successfully by the National Institute of Standards and Technology (NIST) in the U.S. for a 1V Programmable Voltage Standard system (Benz 1997).

For the new NIST 10 V Programmable Voltage Standard System over 13,000 junctions in a series array must be contained within a few mm in order to remain lumped for high-frequency broadband digital codes. This requires a spacing between junctions of under 500 nm. Using the Focused Ion Beam microscope (FIB) -based fabrication technique discussed in Chapter 5 it is routinely possible to fabricate deep-submicron scale junctions with critical current ~1 mA and characteristic voltages ~50 μV. The junctions can in principle be placed as close together as one wishes.

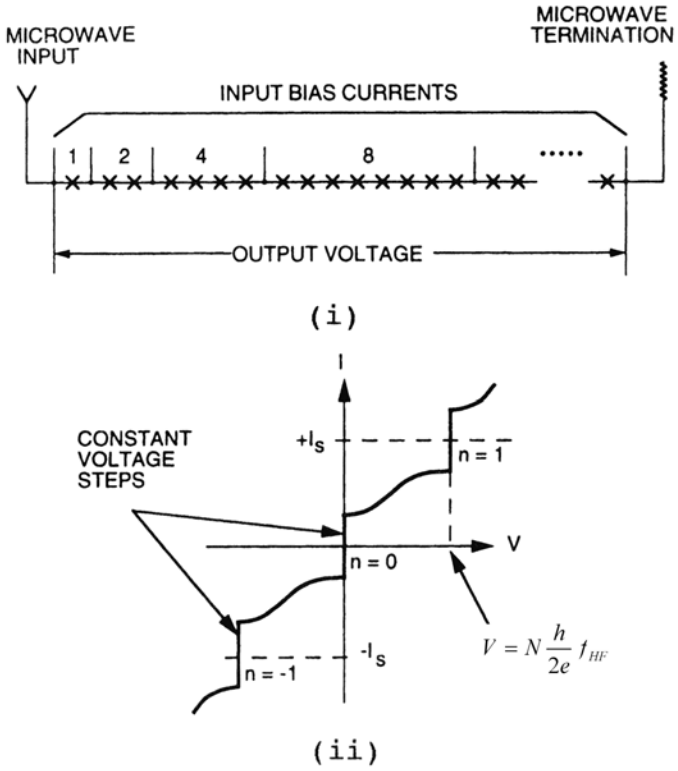

Figure 6.1: (i) A binary divided array for a programmable voltage standard. (ii) Ideal step structure in one of the subdivision of the array when a microwave current is applied (N is the number of junctions in the subdivision). After (Hamilton 1997).

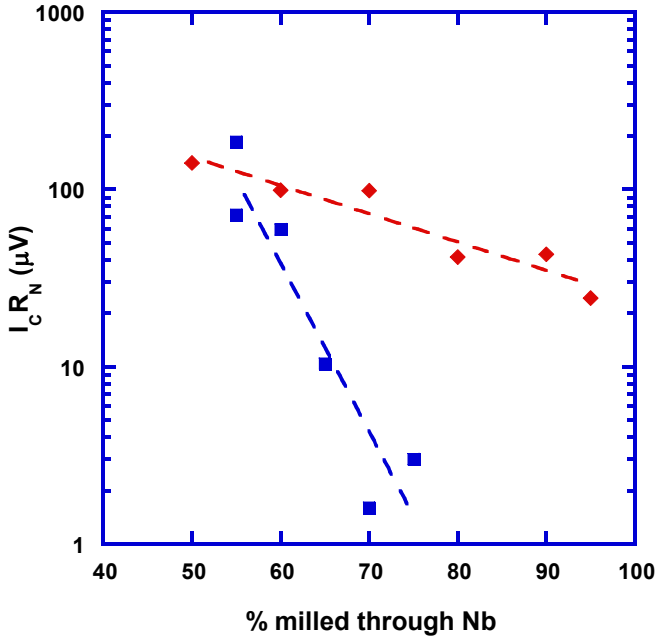

Figure 6.2: Variation of $I_C R_N$ with milling depth for devices fabricated in Nb-PdAu (blue squares) and Nb-Cu (red diamonds). The exponential best fit lines illustrate the general trends

Early studies (Moseley 2000) suggested that in this geometry individual junction properties were only degraded when the nearest neighbour spacing was much less than 100 nm. Over this length scale order parameter and quasiparticle coupling mechanisms through the unbroken normal metal layer come into play. Hence these junctions are excellent candidates for lumped array applications at around 16 GHz. Figure 6.2 shows that for individual junctions fabricated by this method, $I_C R_N$ varies much more slowly with milling depth when Cu used as the normal metal layer, rather than PdAu, which is much dirtier. In terms of the model discussed in Section 5.2.4: although the PdAu film is sufficiently thick (50 nm) such that the coherence length has saturated, it serves mainly to drag down the order parameter Δ in the remaining Nb at the bottom of the trench as PdAu is dirtier than Cu. The increased curvature of Δ leads to a steeper $I_C R_N$ with milling depth profile. Hence a collaboration was established between myself and Dr. Sam Benz at NIST with a view to making prototype arrays of nanoscale SNS junctions in Nb-Cu bilayers.

6.1.3 Allowable spread in junction parameters

In any real array we should anticipate that the properties of individual junctions will not be identical. A question of fundamental importance is what spread in junction parameters (I_C, R_N, $I_C R_N$) will still permit phase-locking of the entire array on a given Shapiro step. The following discussion draws on previous studies (Borovitskii 1985 and Weber 2000).

Consider the effect on (2.38) of an applied microwave current $I_1 \sin(\Omega t)$:

$$I_0 + I_1 \sin(\Omega t) = I_C \sin\varphi + \frac{\hbar}{2eR_N}\dot{\varphi} \qquad (6.2)$$

I_0 is the dc bias current, Ω is the reduced frequency (2.45). All points in (I_C, R_N) space in which a junction is phase-locked at a given step can be determined for a given set of values of I_0, I_1 and Ω. Figure 6.3 shows the reduced parameter areas for the n = 1, 2, 3 steps (S_1, S_2, S_3 respectively) under the condition $I_1 / I_0 = 0.5$. I_C is normalized by I_0 and R_N is normalized by $R_P = \Phi_0 f / I_0$. A shaded area on the diagram represents the variation of junction parameters within a series array. The phase-locking of all junctions at the n^{th} step implies that the shaded area lies entirely within the S_n region of the diagram. Adjusting the bias current I_0 and the input frequency f can alter the position of the shaded area. The extent of the shaded area on the log-log diagram remains the same.

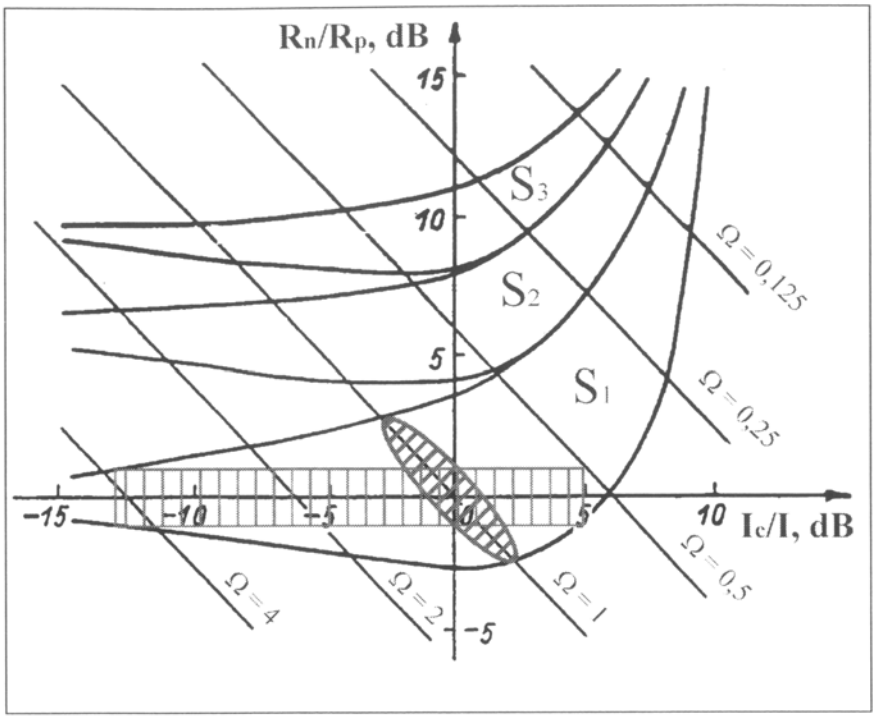

Figure 6.3: Representation of the locking regions for the n=1,2 and 3 Shapiro steps (S_1, S_2, S_3 respectively). The shaded regions represent maximum allowable parameter spreads for arrays to achieve locking on the first step (diagonal hatching: $I_C R_N$ constant; vertical hatching: R_N constant).

Let us consider two possible parameter-spread scenarios:

(a) Constant $I_C R_N$

The shaded area (diagonal hatching) represents an array of non-uniform junctions with equal $I_C R_N$. It is elliptical in form with the long axis parallel to the isochore of Ω. The area is placed at Ω = 1, where the largest parameter spread is allowed for locking at the first step. The tolerance interval for the reduced critical current is from I_C/I_0 = -3 dB to +2dB. This implies an I_C spread $\delta I_C = I_{C\max}/I_{C\min}$= +5 dB ~1.8 ($I_{C\max}$ is the largest single junction critical current within the array; $I_{C\min}$ the minimum). A similar result is obtained for the spread in R_N. Hence Ω = 1 is the optimal working point for an array with constant $I_C R_N$.

(b) Constant R_N

The second shaded area (vertical hatching) represents the parameter-spread area for an array of junctions of approximately equal R_N. The maximum permissible δI_C is along the abscissa. In the diagram $\delta R = R_{\max}/R_{\min}$ = 2 dB = 1.3, which implies δI_C = 17 dB = 7.0. The only disadvantage of this situation is that $I_C R_N$ varies as I_C, so there is no optimal Ω.

6.2 Fabrication Procedure

Dr. Paul Dresselhaus at NIST, Boulder, carried out the film deposition and basic patterning for the samples used in this study. The mask design consists of a main track of 3-8 μm width intersected by voltage taps. The design also incorporated a coplanar waveguide for uniform microwave injection. The samples were then delivered to Cambridge for FIB-patterning and basic characterization by the author. Promising devices were posted back to NIST for further investigation.

The basic fabrication procedure was as follows:

A 125 nm Nb 75 nm Cu bilayer is deposited on an oxidized Si substrate in an ultra-high vacuum magnetron sputtering system in sequence without breaking vacuum. This ensures both excellent film and interface quality. The microscopic track layout was defined in the bilayer by photolithography and reactive ion etching. The patterned sample was wirebonded to a holder in a four-point resistance measurement configuration and the sample is transferred to a standard Focused Ion Beam microscope (FIB) for device fabrication. A region of track 1 μm wide was defined by milling on a high beam current (11 pA). Then an array of junctions was milled using a 4 pA beam either in series (milling each junction in sequence) or in parallel (milling the array as a single object). The software to facilitate accurate control of the milling sequence was written by Dr. Gavin Burnell. For comparison a single junction was milled in a neighbouring section of track. This whole process is performed without altering the beam focus.

The milling depth can be deduced from an *in situ* resistance measurement. Customized software now allows milling to be halted when the desired change in resistance and hence milling depth is reached. For this study arrays of 10 junctions with spacings of 0.2 μm to 1.6 μm were milled in parallel along the main track of a single 10 mm x10 mm chip. The milling time per junction (area milled 2 μm x 50 nm) was 11 s. Figure 6.4 shows a schematic of the array milling process and Figure 6.5 shows a finished 10-junction array viewed in the FIB.

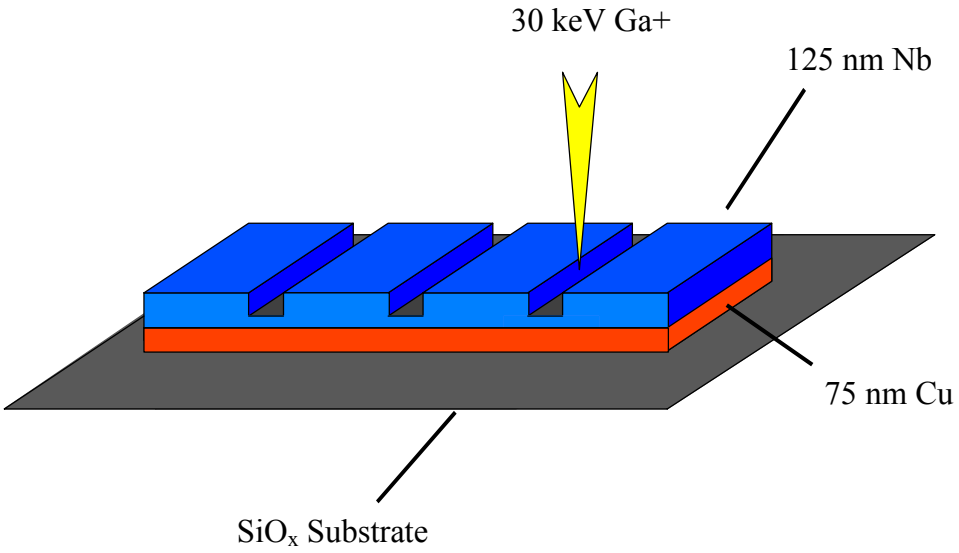

Figure 6.4: Schematic of the array fabrication procedure.

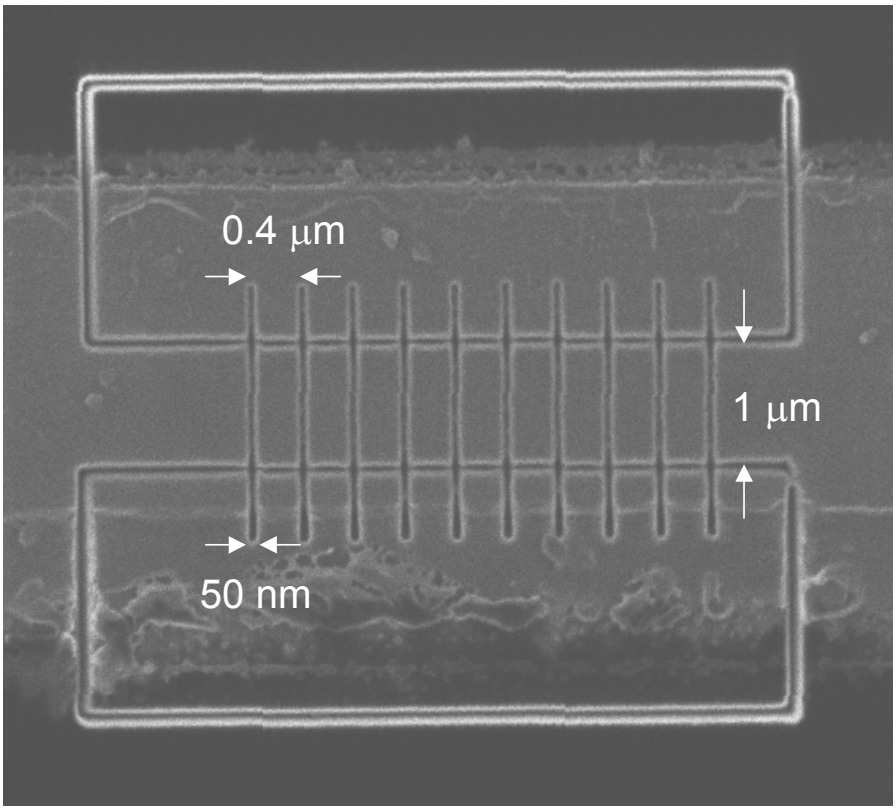

Figure 6.5: FIB image (plan view) of a 10-junction array fabricated in a Nb-Cu layer.

6.3 Results

Basic device characterization was performed between 4.2 K and the transition temperature (T_C) using a dip probe including magnetic field coils and microwave antenna. Current-voltage (I-V) characteristics were obtained in a quasi-static current-biased measurement. Microwave measurements were possible in the range 11-18 GHz.

An example of phase-locking as evinced by a Shapiro step is shown in Figure 6.5 (10-junction array, 1.6 μm spacing, 14.0 GHz, 6.0 K – step appears at 0.28 mV). Table 6.1 shows parameters for arrays of spacing 0.2-1.6 μm. The locking temperature given is the lowest at which a convincing ×10 step was observed. In general this temperature is lower when the junction spacing is shorter, suggesting a penetration depth-dependent electromagnetic coupling mechanism.

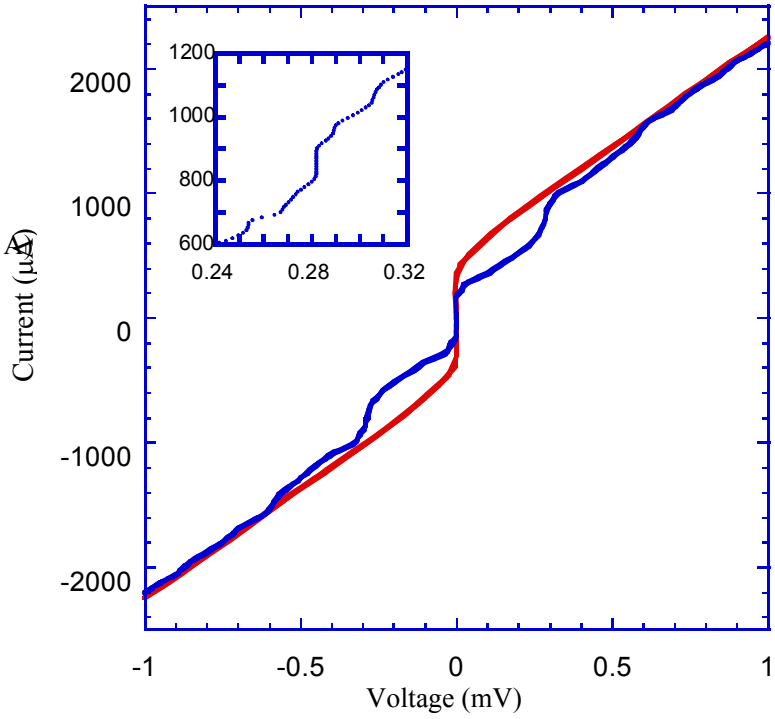

Figure 6.6: I-V characteristic of a 10-junction array (junction spacing 1.6 μm) at 6.0 K. In the main plot the red trace is without microwaves; the blue trace is with microwaves applied at 14.0 GHz. A vertical Shapiro step is obtained at 0.28 mV, but additional features are in evidence (inset).

Low noise differential resistance measurements as a function of bias current (*dV(I)/dI)* were made with the aid of a lock-in amplifier (see Section 3.3.3). This allowed the switching of individual junctions in an array to be observed. Figure 6.7 shows the *dV(I)/dI* characteristic of an array and a single junction at 4.2 K. From the deduced I_C distribution (statistics shown in Table 6.1), the *I-V* of an array can be convincingly reconstructed. Significantly this best fit is obtained by scaling the *I-V* characteristic of a single junction assuming constant R_N (rather than $I_C R_N$). In these devices, when the milled trench does not penetrate the Cu layer, R_N is effectively constant (Cu has a resistivity a factor of 10 lower than that of Nb in the normal state). Due to the small spread in individual junction R_N, locking is achieved in the array in spite of the large spread in I_C (from Table 5.1 $\delta I \sim 1.5$ for 10 junctions).

A low-noise measurement of an array under microwave irradiation reveals structure in addition to the Shapiro-like step (see Figure 6.6 inset). This may arise due to the non-ideal microwave response of individual junctions. The single junction differential resistance profile shown in Figure 6.7 is clearly not ideally RSJ-like, with a bump at ~1.5x I_C (this corresponds to the 'shoulder' feature in 5.12 discussed in Section 5.4). An interesting question is whether this feature leads to a reduction in Shapiro step amplitude if both occur at the same voltage.

TABLE 6.1:
Statistics for arrays of spacings 0.2 to 1.6 μm at 4.2 K

Spacing	*I_C (μA)*			*Spread*	*δI*	*Locking*
(μm)				*(Standard Dev./Mean)*	*(I_{max}/I_{min})*	*Temperature*
	Min.	*Max.*	*Mean*	*(%)*		*(K)*
0.2	890	1700	1389	19.8	1.56	4.2
0.4	2140	3000	2521	10.7	1.40	5.0
0.6	510	1410	904	36.2	2.76	_
0.8	980	1510	1291	11.8	1.54	5.0
1.6	1290	1970	1550	12.3	1.53	5.5

The beam was refocused for the milling of each array, so although the current, area, and milling time per junction were equal, the focusing conditions are only identical for junctions within that particular array.

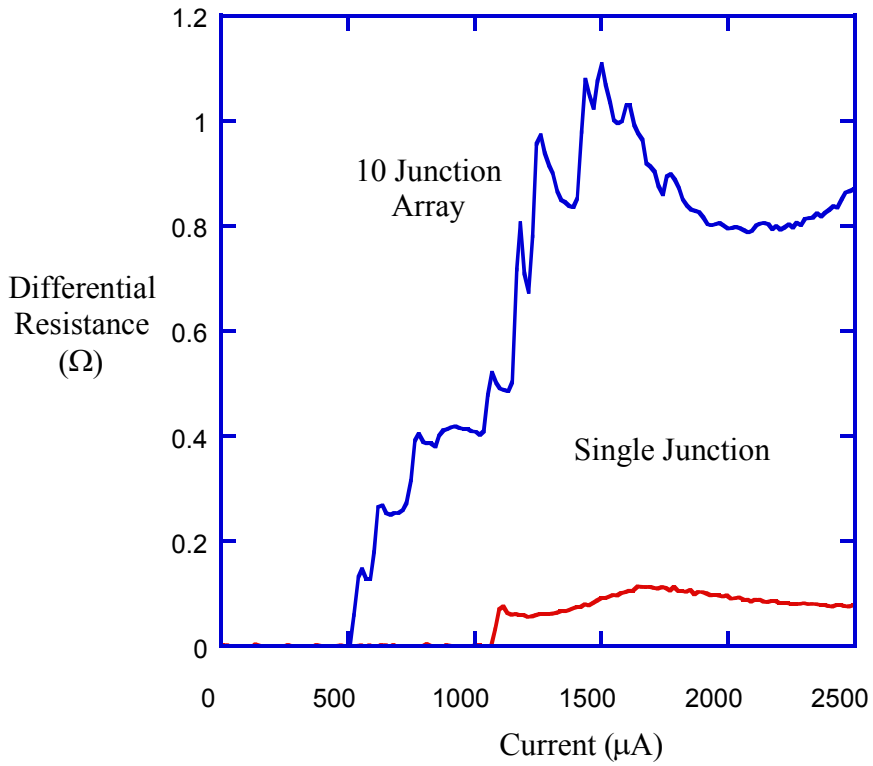

Figure 6.7: Differential resistance versus current for a 10-junction array and a single junction at 4.2 K.

6.4 Discussion and Outlook

6.4.1 Tolerance to spread in junction parameters

As we have seen the current junction technology yields arrays with a small spread in R_N and a large spread in I_C. The unbroken Cu layer effectively shunts all of the junctions in the array, leading to a uniform R_N. The key question is whether the inherent large I_C spread makes this junction technology unsuitable for the fabrication of large-scale arrays. The analysis of Section 6.1.3 suggests that due to the uniform R_N in these arrays a very large spread in I_C can be tolerated, if operating conditions are chosen appropriately. This analysis has already been applied with success to arrays of grain boundary Josephson junctions (GBJs) in high temperature superconductors (Klushin 1996, Weber 2000). Conventional GBJs suffer from large variation in I_C and R_N, but at a given temperature $I_C R_N$ for all junctions is constant. By shunting the junctions with a layer of low resistivity normal metal (Au), the spread in R_N can be negated. The first metrologically-useful devices (secondary voltage standards for 77 K operation) based on this approach are now being produced (Klushin 2001). This is a very encouraging result from the point of view of the work discussed in this Chapter.

6.4.2 Reducing parameter spread: Nb-Cu epitaxy

As discussed in Section 5.4 and shown Figure 6.2 a thick layer of clean normal metal (thicker than the bulk coherence length) leads to the slowest variation of $I_C R_N$ with milling depth. At present Cu provides the best alternative (Au, W, Al, PdAu, Pd, CuNi have also been tried at various times (Moseley 2000, Burnell 2001, Bell 2001). Currently the mean free path and hence the dirty limit coherence length in the Cu films is limited by the grain size (~30 nm, see Chapter 4). A larger grain size could be achieved by using a lattice-matched substrate and raising the deposition temperature.

In an SNS junction I_C depends exponentially on the barrier width (2.27), so even small variations in the width of the FIB-milled trenches will translate to large variations in I_C. For this reason directly-written junctions will always have larger I_C spreads than sandwich structures, where the barrier thickness can be controlled on the order of Å by the deposition process. Beam fluctuations have been eliminated as a source of error by milling all the junctions in the array in parallel, but to little avail. Repeated measurements of the arrays over a period of weeks show no noticeable drift in properties, suggesting migration of implanted Ga is not a serious cause for concern. The fundamental cause of the I_C variation seems likely to be the polycrystalline microstructure of the films leading to an uneven milling rate and hence uneven trench width and depth. Recent reports on FIB milling of single-crystal Cu (Kempshall 2001) suggest that the channeling Ga ions along specific lattice directions in the crystal allows much higher aspect ratio trenches to be milled without topographical degradation. Hence the clearest way to achieve a significant improvement in parameter spreads would also be to use truly epitaxial films.

In a final investigation, the author, with the assistance of Dr. Mark Blamire, attempted the growth of epitaxial Nb-Cu bilayers. As discussed in Chapter 4, films of Nb and Cu sputtered at room temperature onto SiO_2 are polycrystalline in character (grain sizes: Nb under 10 nm, Cu 30 nm in-plane). Epitaxial film growth implies growth of a *single crystal* film. Hence a substrate must be chosen which is matched to the lattice parameters of the metal crystal structure and an elevated temperature is required to initiate epitaxial 'step-flow' growth. In this study r-plane and a-plane sapphire (Al_2O_3) were considered as suitable substrates. Epitaxial Nb films have been successfully grown in this laboratory by sputtering on heated r-plane sapphire substrates (Warburton 1995, Burnell 1998). There are several reports of Nb-Cu heteroepitaxial growth by UHV e-beam evaporation (Di Nunzio 1996) and molecular beam epitaxy (Yamamoto 1998). It should be noted that best results were obtained by depositing a Nb buffer layer on the sapphire.

TABLE 6.2:
Summary of reports of epitaxial Nb-Cu bilayer growth.

Substrate	Nb	Cu	Reference
a-plane sapphire $(11\bar{2}0)$	(110)	(111)	Yamamoto 1998
r-plane sapphire $(1\bar{1}02)$	(001)	(001)	Di Nunzio 1996

To avoid defect growth, substrates were rigorously cleaned using nitric acid, chloroform, acetone and ultrasound (Burnell 1998). The Mark III sputtering system was used in this work (essentially similar in operation to that desribed in Chapter 4). The major difference being the flange used. In this case a heater was employed: substrates were placed on a tantulum strip which through which a current of upto 20 A was passed. To achieve a gradient in temperature the width of strip tapered (the narrowest end being hottest). Films were sputtered at around 1 Pa pressure. Film thicknesses were determined by profilometer and the films were characterized by X-ray diffraction.

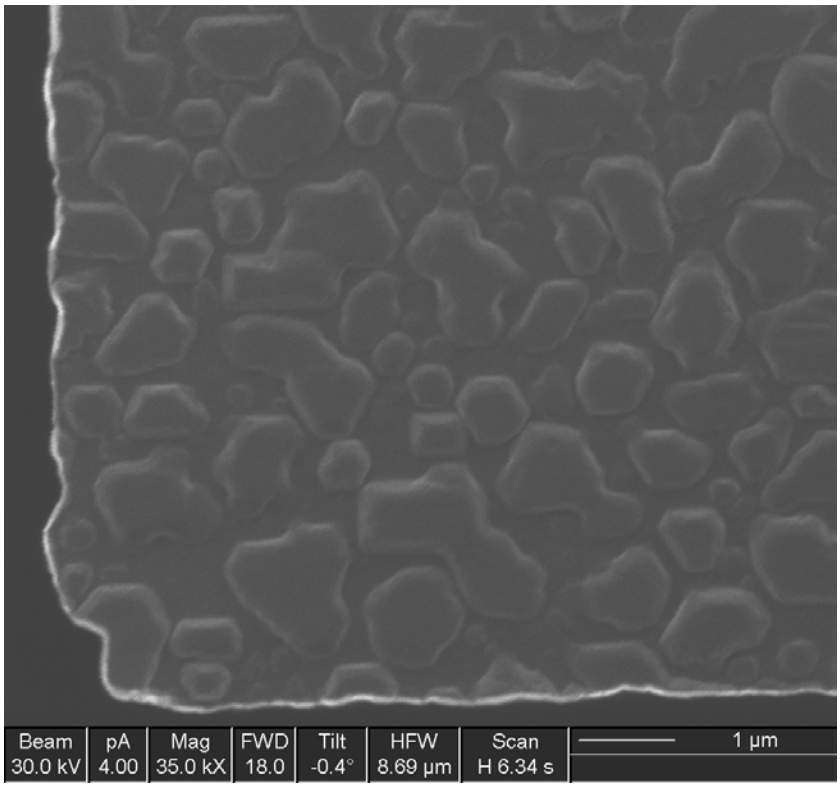

Figure 6.8: FIB image of a Nb-Cu-Nb (125 nm Nb 75 nm Cu 20 nm Nb) sputtered multilayer. The large islands visible on the surface are believed to be Cu grains.

Various difficulties were encountered in this study. T_m is higher for Nb than for Cu, therefore after the deposition of the Cu layer the heater current was raised further. This lead to evaporation (indicated by a Cu-coloured deposit on the heater around the samples) and retexturing of the Cu layer on the samples themselves. In the best samples obtained (again by using a thin Nb (~20 nm) buffer layer), the Cu grain size was considerably larger (up to 1 μm) with promising X-ray response (Cu (111) full width at half maximum 0.5°). However these same films were extremely rough. An FIB image of such a film is shown in Figure 6.8. The individual micron-sized Cu grains are clearly visible. Attempts at creating junctions in these tracks were unsuccessful – at best flux-flow type current voltage characteristics were obtained (resistance increases with increasing current bias).

6.4.3 Scaling up: fabricating large numbers of junctions reproducibly

As mentioned in Section 6.1.1 over 13,000 junctions are required for the NIST 10V Programmable Voltage Standard System. The milling time for each junction is ~10 s making the FIB-based serial writing process is extremely laborious. In addition, as we move over distances of hundreds of μm, refocusing and recalibration of milling depths will certainly be necessary. Hence alternative routes to planar SNS junction fabrication in superconductor-normal metal bilayers were explored by our collaborators at NIST.

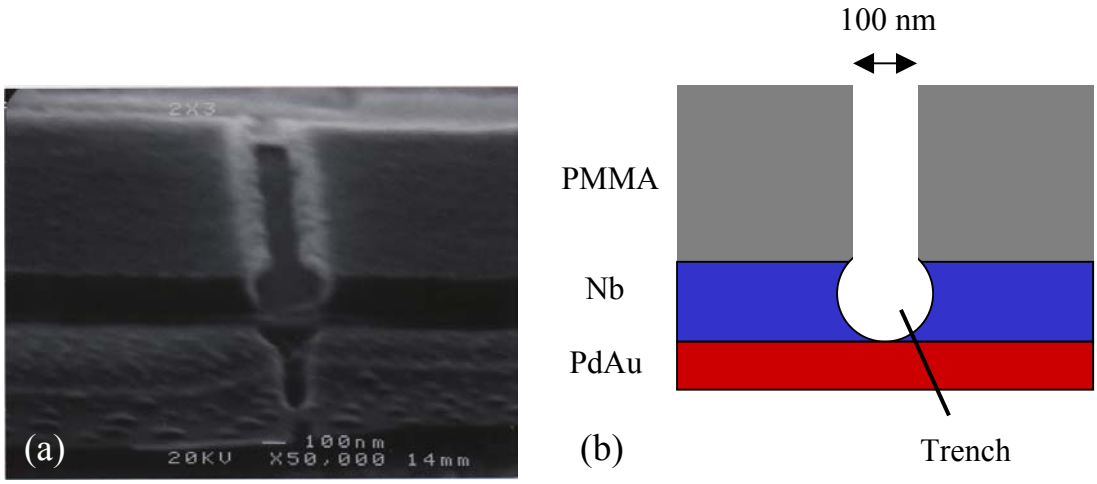

Figure 6.9: Alternative route to planar SNS junction fabrication. (a) SEM image of a trench formed by RIE in a Nb-PdAu bilayer courtesy of Dr. Paul Dresslhaus - note the PMMA mask has been stripped away (b) Schematic of undercutting.

A 100 nm trench was patterned by e-beam lithography in PMMA resist layer. The trench was transferred Nb beneath by Reactive Ion Etching (RIE). RIE, is a combined physical and chemical etch process, using a highly reactive plasma such as SF_6 or CF_4. Under correct conditions a highly anisotropic, selective etch can be achieved. Nb is etched selectively by RIE, whereas other metals and alloys such as Al, PdAu or Cu are unaffected by the process. Figure 6.9 shows the results of RIE etching a Nb-PdAu bilayer. The Nb trench is considerably wider than intended due to backscattering of ions from the PdAu surface. The resulting device showed no critical current at 4.2 K. In order to boost the I_C a thin Al layer could be inserted in the Nb layer, resulting in a Nb microbridge shunted with normal metal. However backscattering from the etch stop layer may still lead to an inhomogeneous trench profile and an unacceptably high spread in device parameters.

6.5 Conclusion

The focused ion beam-based planar SNS junction fabrication technology described in Chapter 5 has been successfully applied to the fabrication of small-scale series arrays. The results contained in this Chapter have been published (Hadfield 2001b). Phase-locking has been achieved in 10-junction arrays of spacings 0.2-1.6 microns. An analysis has been carried out of the spread in individual junction critical currents within each array. Studies show that due to the low spread in junction R_N, the large I_C spread in inherent in the fabrication process is not necessarily an obstacle to finding useful applications. Possibilites for reducing parameter spreads and scaling up the process for the fabrication of large-scale arrays have been discussed. Furthermore, the low noise measurement technique and parameter spread analysis developed here is now being used collaboration with Dr. Dae-Joon Kang for evaluation of junction arrays in $YBa_2Cu_3O_{7-x}$ and MgB_2 fabricated by masked ion damage (Kang 2002).

Chapter 7: The Corbino Geometry Josephson Junction

7.1 Introduction

This Chapter describes the fabrication and measurement of the first thin film based junction with the circular barrier in the same plane as the electrodes. The unique properties of junctions in this geometry have been discussed in Section 2.6. This investigation is an extension of the focused ion beam (FIB) based planar superconductor-normal metal-superconductor (SNS) junction fabrication technique described in Chapter 5. The starting point is a superconductor-normal metal bilayer (125 nm Nb on 75 nm Cu). A 50 nm wide trench is milled into the upper superconducting layer in order to achieve weak coupling. Milling a circular trench and making an electrical contact to the central island creates a Corbino geometry SNS junction. Figure 7.1 illustrates the Corbino geometry; the term derives from the experiment carried out by Corbino in 1911 to demonstrate the Hall Effect in a disc-shaped conducting sample (Corbino 1911).

Figure 7.1: The author demonstrating the Corbino geometry (visual aid courtesy of Wham-o Inc.). Orso Mario Corbino demonstrated (Corbino 1911) that if current contacts are made to the centre and the rim of a disc-shaped conducting sample and a magnetic field is applied perpendicular to the plane of the sample, in addition to the radial current (marked by the arrows), there will also be a circulating current. The Corbino Effect is hence the equivalent of the Hall Effect in a circular geometry.

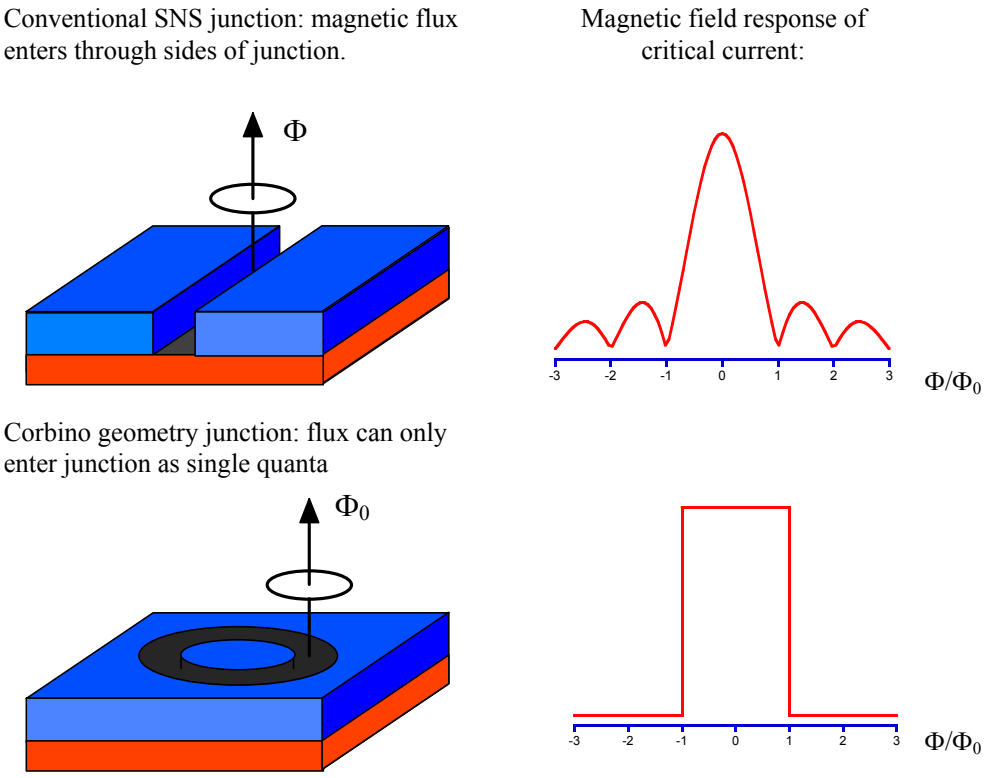

Figure 7.2: Simple view of conventional and Corbino geometry junction magnetic field response.

A simple consideration of the basic phenomenology expected in this special junction geometry is shown in Figure 7.2. In a conventional Josephson junction magnetic flux can enter progressively through the edges of the junction. As a result the phase difference between the electrodes varies across the width of the junction, leading to a continuous modulation of the junction critical current. In the simplest two-dimensional geometry the critical current versus magnetic field, $I_C(B)$ follows a modulus of a sinc function dependence, analogous to the diffraction pattern of monochromatic light due to a single slit in the Fraunhofer regime (Barone 1982). The first minimum occurs when one flux quantum Φ_0 is present in the barrier. In the case of a SNS junction fabricated in the Corbino geometry, the barrier region is entirely enclosed in a loop of superconductor, therefore magnetic flux is only permitted to enter as single quanta (Tilley 1966). The critical current versus magnetic field dependence $I_C(B)$ should now abruptly switch from the maximum value to zero as flux enters, resulting in a top hat $I_C(B)$ pattern. In this investigation the $I_C(B)$ response of such junctions at 4.2 K - as we shall see, the observed behaviour is more subtle than this simple picture. As the junction is overdamped, quantized flux trapped in the barrier will not propagate freely. However, when a bias current is applied the flux can be driven around the barrier. In the low temperature limit for a clean barrier the driving force should be attenuated by Berry phase effects (Gaitan 2001, Plerou 2001).

7.2 Experimental Technique

As in the basic planar SNS junction experiments, a microscopic track layout was defined by lift-off patterning of the sputtered bilayer (125 nm Nb, 75 nm Cu on an oxidized Si substrate). The track layout contains a main track of 8, 7, 6 μm width sections intersected by voltage/current lines. The milling depth of a 50 nm wide trench on 4 pA FIB beam current was calibrated on a test track using the *in situ* resistance measurement. Circular trenches (2.5 μm radius, various depths 60 - 100 % through Nb thickness) were then milled in the main track.

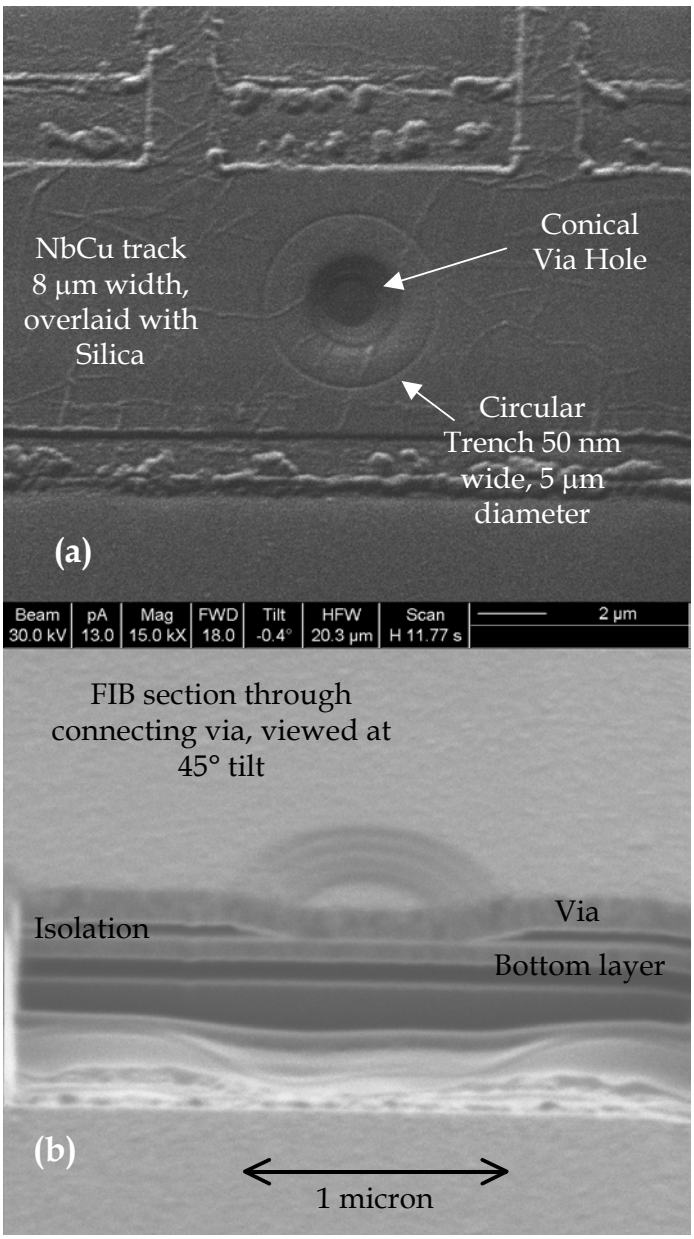

Figure 7.3: (a) FIB image of device at via milling stage (b) Via contact sectioned and viewed at 45° tilt in the FIB.

Isolation cuts were milled in the main track to separate the individual devices using a large beam current (70 pA). After further lift-off patterning, a silica isolation layer (thickness 250 nm) was deposited by RF sputtering over the region of interest. The sample was then returned to the FIB system and via hole milled onto the central island of each junction. In the FIB, milling depth per unit area through an insulating layer can be calibrated by measuring the sample stage current; a jump is observed when the insulating layer is breached (this is known as the FIB 'end-point detection' facility). Straight-sided via holes were found to give poor via filling when the final metallization layer was deposited, leading to a considerable shunt resistance in early devices (Hadfield 2002b). The perfected via hole procedure was as follows: a sequence of concentric circles was milled (1.25 to 0.75 μm radius) to create a conical hole 80 % of the way through the insulator. After a final lift-off patterning stage, the sample was transferred to a combined Ar milling/dc magnetron sputtering system. The final (Ga-implanted) insulating layer was removed by Ar milling and a Nb-Au (~30 nm Nb, ~200 nm Au) layer was deposited without breaking vacuum. The Nb layer was purely intended to improve Au adhesion – a thick superconducting top electrode was found to make the resulting device too insensitive to external magnetic field. Figure 7.3 (a) is an FIB image of a device at the end of the via hole milling stage. Figure 7.3 (b) shows a conical via (no junction barrier defined) sectioned and viewed at 45° tilt in the FIB.

7.3 Results and Discussion

7.3.1 Measurements at 4.2 K

We are now routinely able to produce Corbino geometry junctions with comparable critical current densities to planar SNS junctions previously fabricated. Figure 7.4 (a) shows a comparison plot of normalized critical current versus milling depth through the Nb layer for planar SNS and Corbino geometry devices. Figure 7.4 (b) shows the current-voltage *(I-V)* characteristic of a Corbino geometry junction at 4.2 K with and without applied microwave radiation. The *I-V* characteristic without microwaves is non-hysteric and approximately RSJ type. Series resistance due to the via contact is minimal. There is a strong microwave response: the critical current can be completely suppressed indicating a pure Josephson current and strong Shapiro steps are observed; half integer steps (a common feature of planar SNS devices (Dubos 2001)) are also evident.

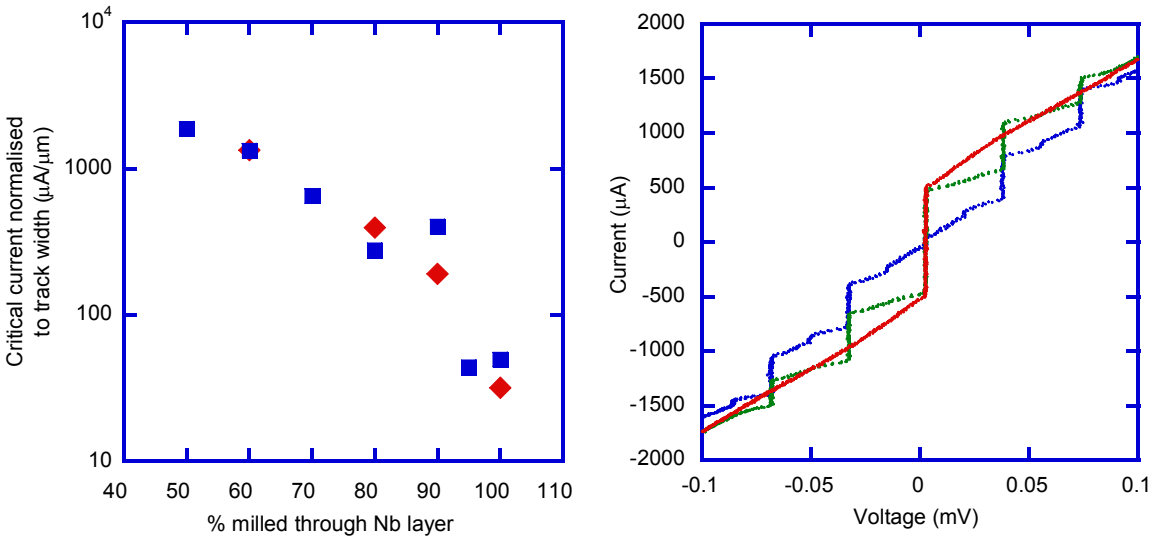

Figure 7.4: (a) Critical current normalized to barrier width for planar SNS junctions (blue squares) and Corbino geometry junctions (red diamonds). (b) Microwave response at 17.0 GHz of a Corbino geometry junction. Series resistance is under 1 mΩ.

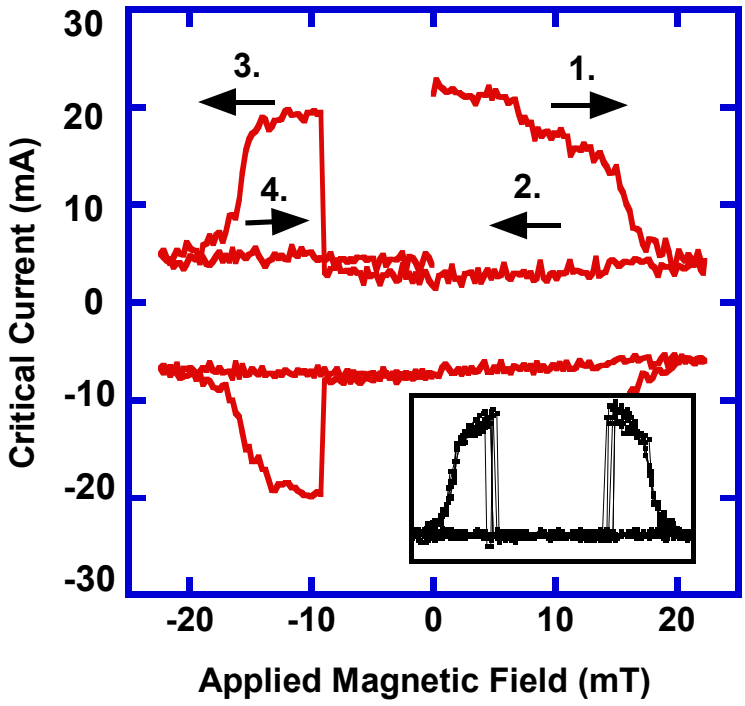

Figure 7.5: Critical current versus applied field for 5 μm diameter junction in a 8 μm width track. The numbered arrows indicate the field sweep sequence. Inset shows the same behaviour repeated over multiple cycles.

As discussed in Section 7.1, a distinctive magnetic field response is expected for this type of device. Figure 7.5 shows the critical current, I_C of a high critical current Corbino geometry junction (5 μm diameter junction in 8 μm width track) in a perpendicular magnetic field at 4.2 K. Measurements were taken with a mumetal shielded dip-probe in a He bath. Current-biased measurements were made of the *I-V* characteristic at each value of field; the value of I_C was extracted using a voltage criterion.

Magnetic field was applied perpendicular to the plane of the sample via a calibrated Helmholtz pair. Over a small field range no irreversible change in I_C is observed. If the external field exceeds 15 mT, I_C is suppressed steeply and irreversibly. This can be identified as the entry of one quantum of flux ($\Phi_0 = h/2e$) into the junction barrier. When the external field is reduced back to zero I_C remains suppressed and the flux is trapped in the junction. As the field direction is reversed I_C reappears abruptly at 8 mT. At this point a flux quantum of opposite orientation enters the junction and annihilates the original trapped vortex. A second steep, but not abrupt, suppression of I_C occurs at 15 mT corresponding to the trapping of a flux quantum of negative polarity in the junction barrier. As illustrated in Figure 7.5 (inset) this behaviour can be repeated over multiple cycles, the flux entry/annihilation events occurring at almost identical fields (given the presence of electrical and thermal noise at 4.2 K). This dynamic response of the critical current to magnetic field is dependent on the exact configuration of the Meissner state in the superconductor; slightly different behavior can be observed in the same device each time it is heated and cooled through the superconducting transition.

A more reproducible way to identify the flux entry event is to *field cool* the device at set external field. Results for a device of lower current density are shown in Figure 7.6. Quantized flux trapping in the barrier is identified by performing an $I_C(B)$ sweep at 4.2 K. If the field was swept first in the same direction as the cooling field, no change should be expected (I_C remains suppressed). An annihilation event is then expected when the field is swept in the opposite direction to the cooling field. Scanning Hall Probe studies on microscopic Nb thin film tracks (Field 2002) suggest there is a small but measurable surface barrier to flux entry (see also Section 2.2.5 - the experiment in question supports an unpublished theory by Clem (Clem 1998)). This would lead us to expect an abrupt suppression in I_C at this cooling field. Although I_C is rapidly suppressed with cooling field, conclusive evidence of flux trapping in the barrier was only observed at relatively high cooling fields. This suggests that flux is entering the film at low cooling field, but being pinned elsewhere (the via contact in particular is liable to contain a large concentration of pinning sites).

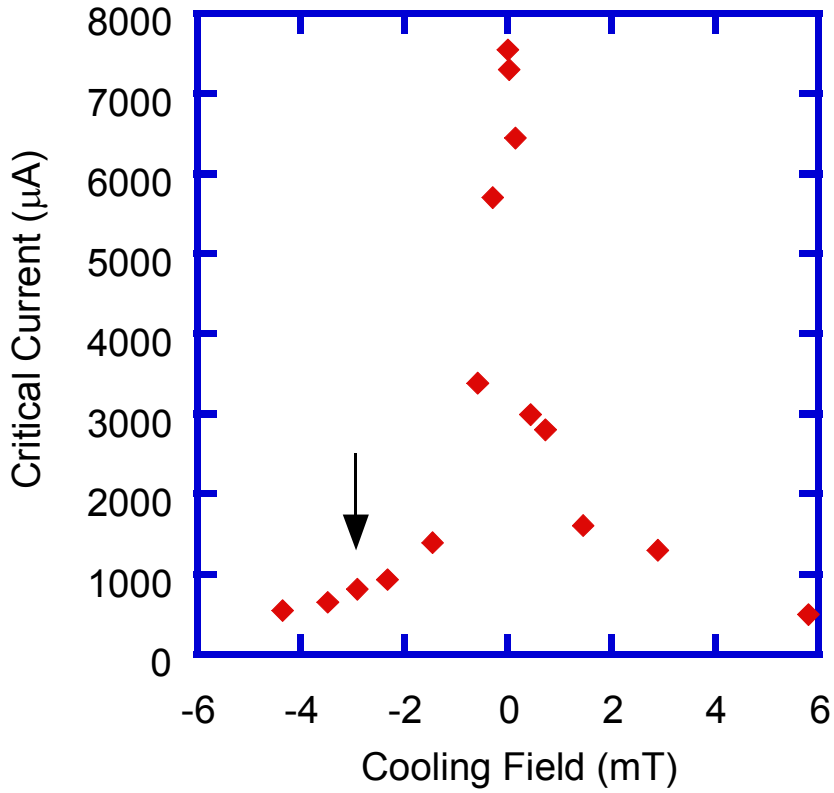

Figure 7.6: Field-cooled measurements of critical current (5 μm device in 8 μm width track). Irreversible flux trapping in the junction occurs at an external field of 2.5 mT as indicated.

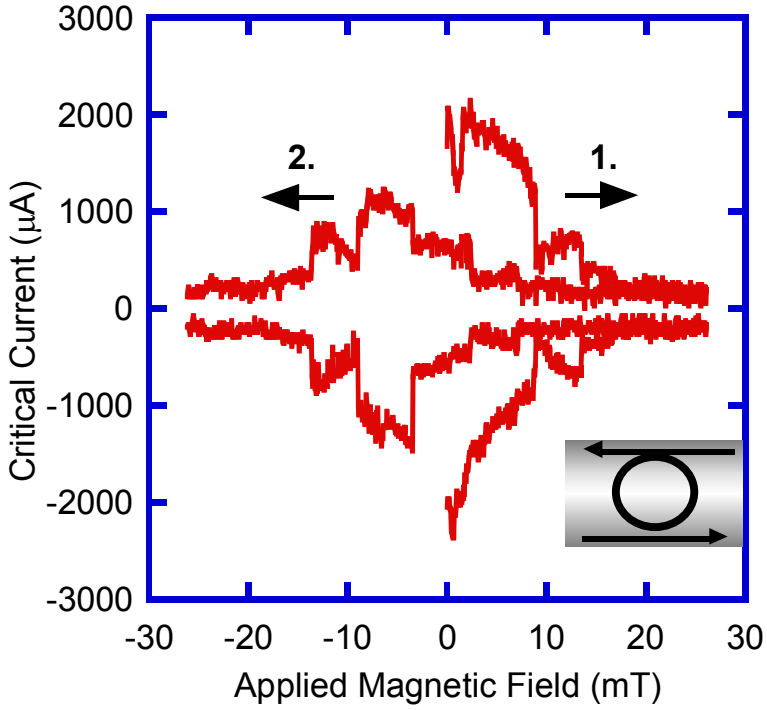

Figure 7.7: Critical current versus magnetic field for a 5 μm diameter junction in a 6 μm track. The field is swept from 0 to +25 mT to –25 mT. Inset: schematic of geometry. Flux quantization (2.4) is not achieved if screening currents overlap the edges of the junction.

We have also explored the situation where the track is thinned such that the superconductor surrounding the junction barrier is of the order of the London penetration depth λ_L at its narrowest point (≅ 100-500 nm for Nb in the plane of the film). Figure 7.7 shows critical current versus magnetic field at 4.2 K for a 5 μm diameter junction in a 6 μm width track. The critical current is now suppressed in a series of jumps. As the field is reduced critical current reappears incrementally, before another series of suppression events. As in Figure 7.5, this behaviour was repeatable over a large number of cycles. As mentioned in Section 2.2.5, flux quantization in units of less than *h/2e* may occur over mesoscopic distances from an edge a in thin film superconductor (Kogan 1994, Geim 2000). These electrical measurements strongly suggest that flux trapping is occurring in units less than *h/2e* in the junction barrier itself.

7.3.2 Model based on the approach of a single vortex to the junction

Firstly consider a vortex in a semi-infinite thin film. As the interface is approached the flux on the vortex is reduced (Kogan 1994). The relevant penetration depth is $\lambda_p = \lambda_L^{\,2} / t$ where t is the film thickness. Figure 7.8 shows the how the flux associated with the vortex is reduced as the surface is approached.

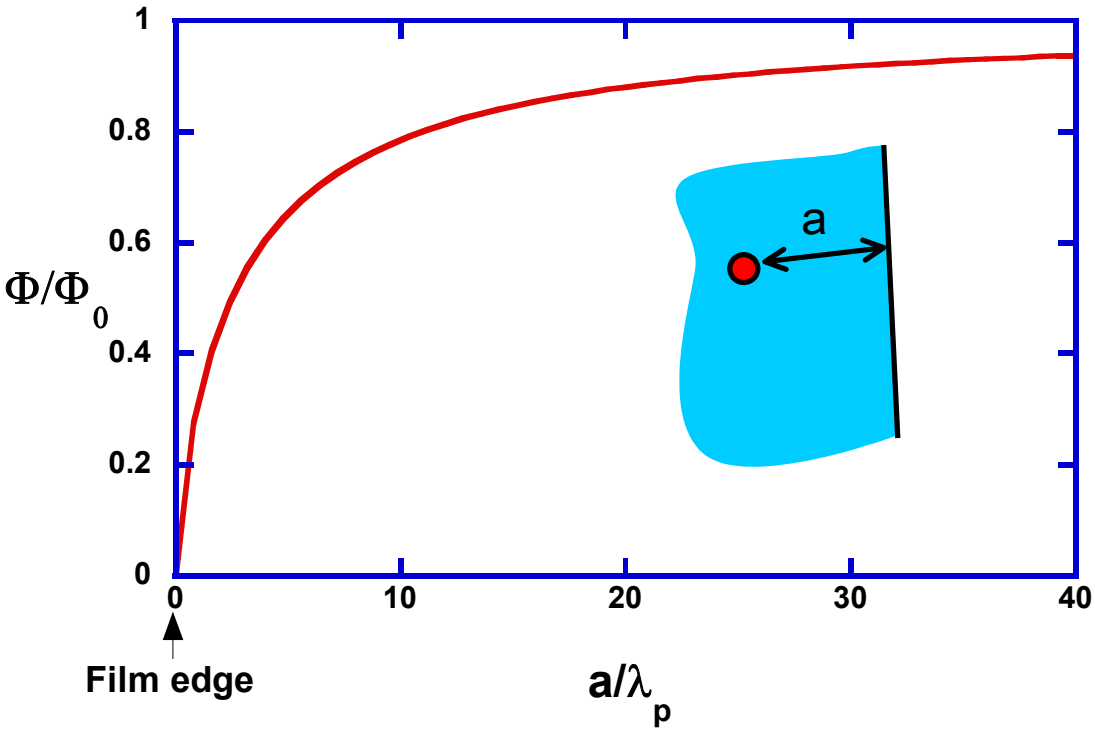

Figure 7.8: Flux on Pearl's vortex approaching an interface (after Kogan 1994) as a fraction of the flux quantum $\Phi_0 = h/2e$.

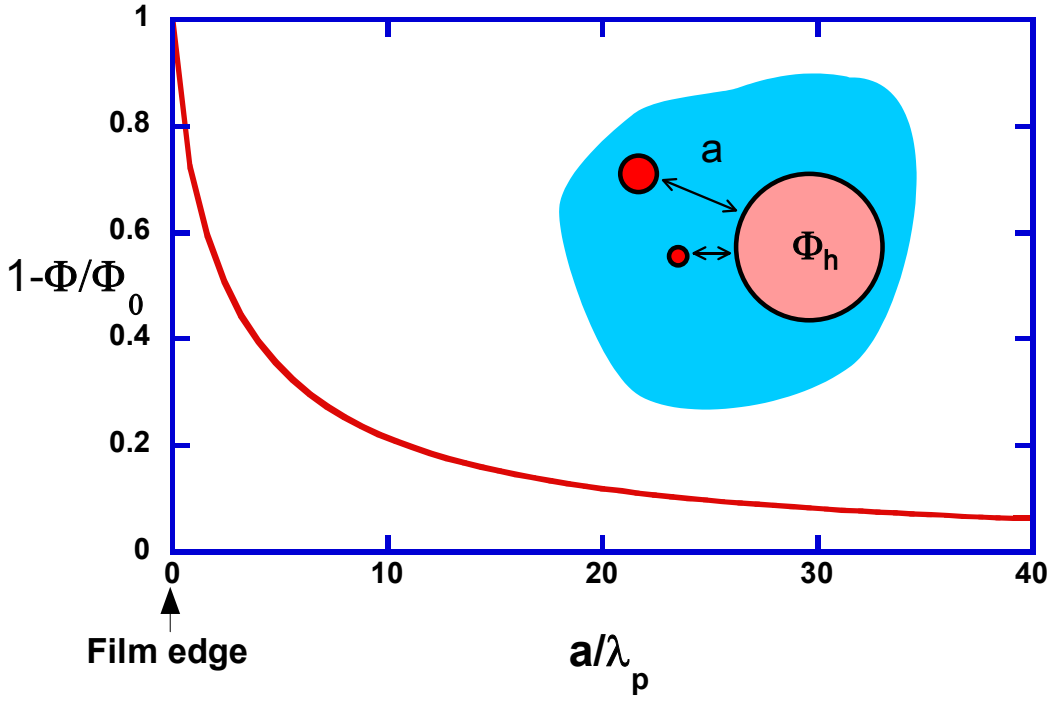

Figure 7.9: Migration of flux into a cavity in a superconducting sheet with the approach of a vortex. Flux in cavity $\Phi_h=\Phi_0-\Phi$.

The same approach to can be applied to a hole in an infinite superconducting sheet. As the vortex approaches the hole the flux lost by the vortex must end up in the hole. (Figure 7.9). Similarly if we have a Corbino geometry junction embedded in an infinite superconducting sheet, the flux lost by the approaching vortex must migrate to the junction barrier. In the short junction limit ($\lambda_J >> 2\pi R >> \lambda_L$) we can assume that this flux is uniformly distributed in the junction barrier.

The effect on the phase difference around the junction barrier due to the approaching vortex is illustrated in Figure 7.10. The phase varies linearly with θ due to the even distribution of flux in the junction barrier. The overall change in phase with one revolution must be 2π, therefore at θ_{Vortex} there is a discontinuity. When the vortex enters the junction the flux in the junction is equal to Φ_0 so the discontinuity disappears. In the short junction limit it is straightforward to calculate the variation in junction I_C with vortex separation a.

$$I_C \propto \sin\left(2\pi \frac{\Phi_h(a)}{\Phi_0} + \varphi_0\right) \qquad (7.1)$$

The flux in the junction is given by the expression illustrated in Figure 7.9. Maximizing with respect to φ_0 using Mathematica™ we obtain the result of Figure 7.11.

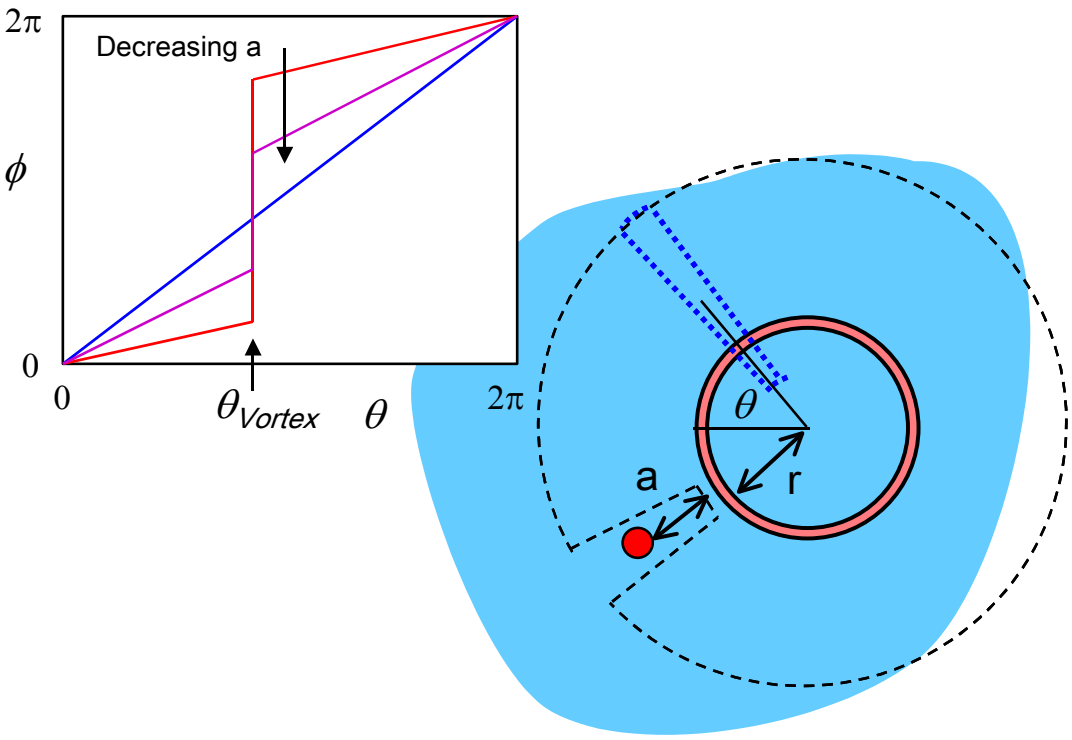

Figure 7.10: Phase difference contributed by approaching vortex for a short junction.

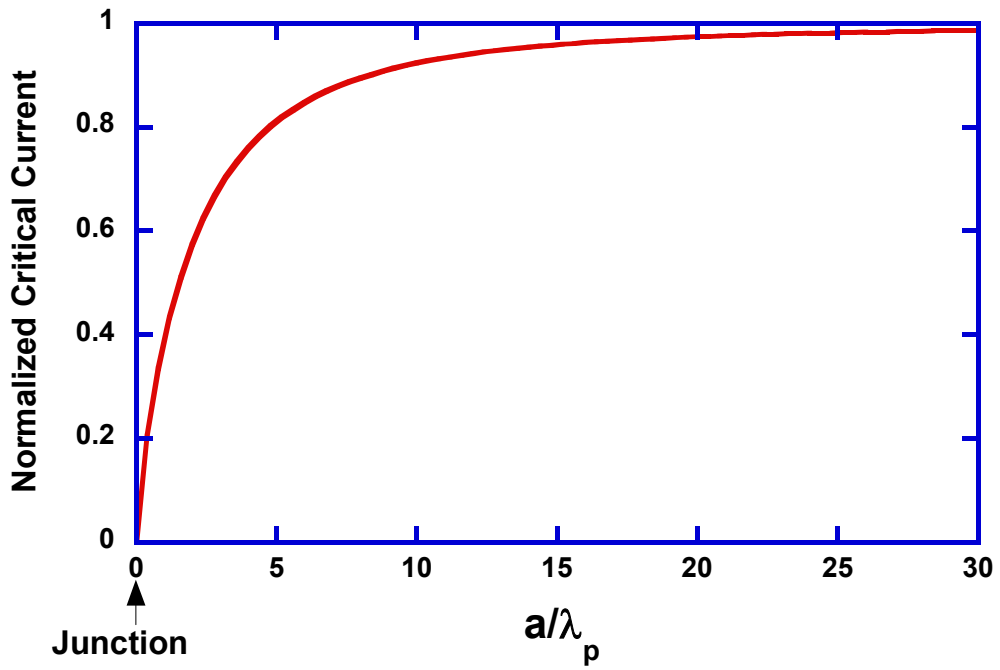

Figure 7.11: Variation of critical current with vortex separation (calculated using Mathematica™).

The simulation of Figure 7.11 suggests that critical current I_C will be suppressed steeply but not abruptly as a vortex approaches the junction. This is quite similar the suppression of I_C that we see in the data (Figure 7.5). The result of Figure 7.7, where the distance from the junction barrier to the edge of the superconductor is reduced may be interpreted as the entry of several vortices into the junction, each carrying an overall flux less than *h/2e*. The distance of the vortex from the junction must be reduced as the applied magnetic field is increased ($B \propto 1/a^2$). However in a real device actual vortex separation must be strongly dependent on surface barriers to flux entry and pinning sites within the film (Figure 7.12).

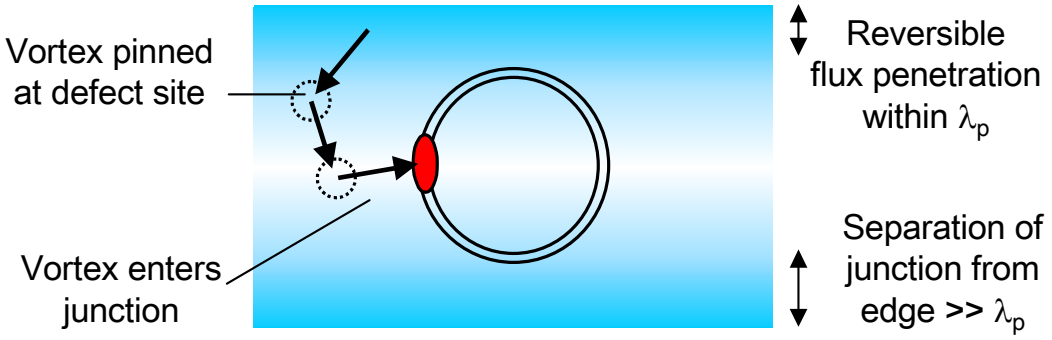

Figure 7.12: In a real device the migration of flux into junction barrier is likely to be via a series of pinning sites.

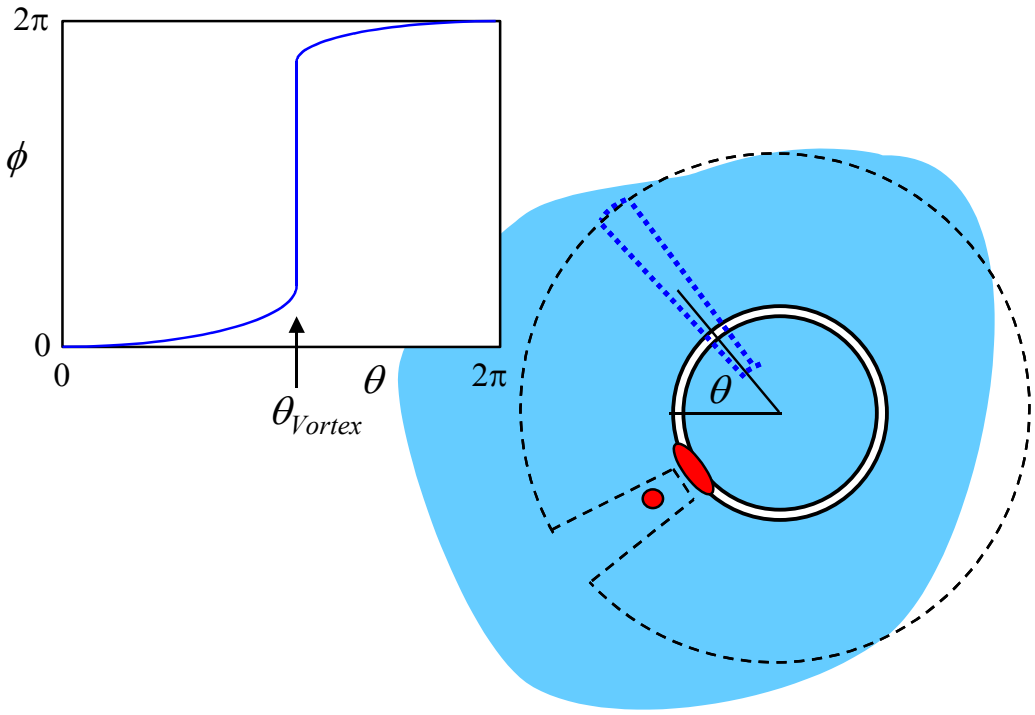

Figure 7.13: Phase difference contributed by approaching vortex for a long junction. The flux in the junction is confined on the scale of the Josephson penetration depth λ_J.

Furthermore the junctions used in this investigation are in the long junction limit. As Figure 7.4 (a) clearly shows, the critical current per unit barrier width scales with milling depth in the same way in both Corbino geometry and planar SNS junctions. Hence the estimate of Josephson penetration depth of Section 5.4.1 applies equally well to the Corbino geometry devices of this Chapter: $\lambda_J < 1$ μm as compared to an overall barrier circumference 'w' of 15.7 μm. The flux in the junction will then be confined on the length scale of λ_J (illustrated in Figure 7.13). Simulations of Abrikosov vortex approach to a long junction are more challenging, but qualitatively may be expected to yield a similar result in the Corbino geometry case as that illustrated in Figure 7.11. It is clear that the approach of a second vortex will not lead to a significant change in the critical current – there may be a reappearance of I_C when the vortex is very close. If the external field direction is reversed a more dramatic result can be expected - *anti*-vorticies penetrate the film (Figure 7.14). The vortex trapped in the junction and the anti-vortex experience an attractive force, leading an abrupt annihilation. This is evinced in the $I_C(B)$ characteristic as a rapid reappearance of I_C. This is indeed what is seen in Figure 7.5.

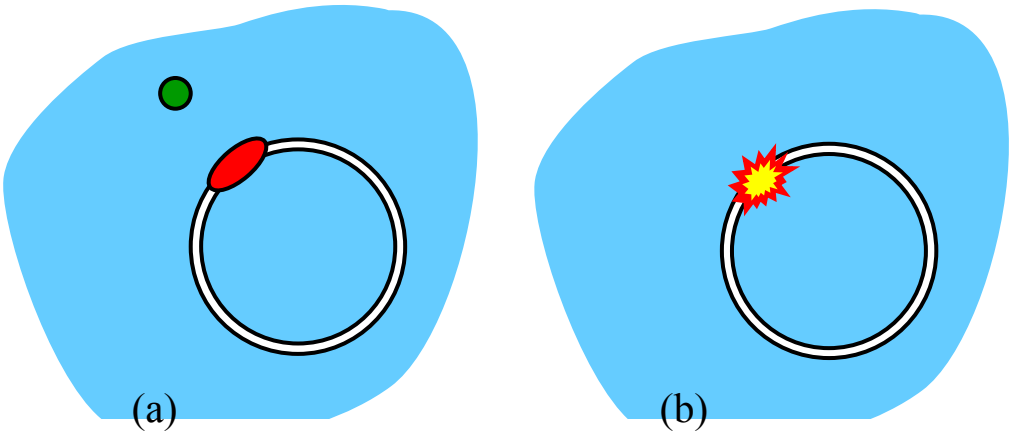

Figure 7.14: Long junction with one vortex (red) trapped (a) anti-vortex (green) approaches junction (b) abrupt annihilation event takes place.

In practice the most elegant method of investigating the effect of junction I_C of an approaching vortex would be by Low Temperature Scanning Electron Microscopy (LTSEM) (Gross 1994). The electron beam can be used to drag a vortex into the junction whilst measuring the junction *I-V* characteristic (Ustinov 1993). This technique should allow us reproduce the numerically predicted result of Figure 7.11. Furthermore this technique would afford the opportunity to study the current density distributions in the structure.

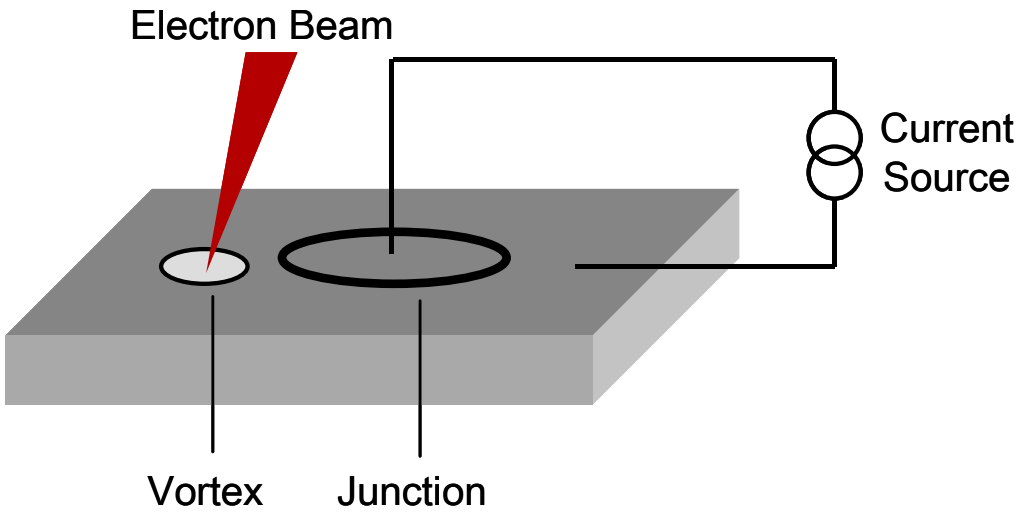

Figure 7.15: Proposed Low Temperature Scanning Electron Microscopy (LTSEM) experiment: the electron beam is used to drag a vortex into the junction barrier, whilst the *I-V* characteristic of the junction is measured.

7.3.3 Alternative model based on self-fields of screening currents

Another approach was taken to modelling junction response to external magnetic fields, taking into account the actual geometry used in the experiment. We assume that the separation of the junction barrier is of the order of the magnetic penetration depth, λ_p.

$$I = I_C \sin(\varphi) \ . \tag{7.2}$$

The phase difference across the junction φ varies with position as (Barone 1982):

$$\underline{\nabla}\varphi = \frac{2\pi\mu_0 d_{eff}}{\Phi_0}\underline{H} \wedge \underline{\hat{u}} \ , \tag{7.3}$$

where $\underline{H}$ is the effective magnetic field and $\underline{\hat{u}}$ is a unit vector in the direction of current flow. There are two magnetic field contributions to take into account, illustrated in Figure 7.16.

Firstly, in an external applied field screening currents will flow in the edges of the film (Figure 7.16 (a)). The self-field of these screening currents leads to an effective field in the junction barrier. This can be approximated by a $\sin^2$ field distribution with angle θ (for computational ease we pick the simplest analytic function with the correct period). Secondly in the actual experiment the bias current is injected from one side or other of the junction (and extracted through the central island). To ensure a uniform current flow through the junction barrier, current flows by two different paths into the far side of the junction (Figure 7.16 (b)). The self-field contributed by these two different current paths can be modeled by a sinusoidal field distribution. This means that if the junction is exactly aligned on the axis of the track, the self-field of the bias current will contribute no net flux over the whole barrier.

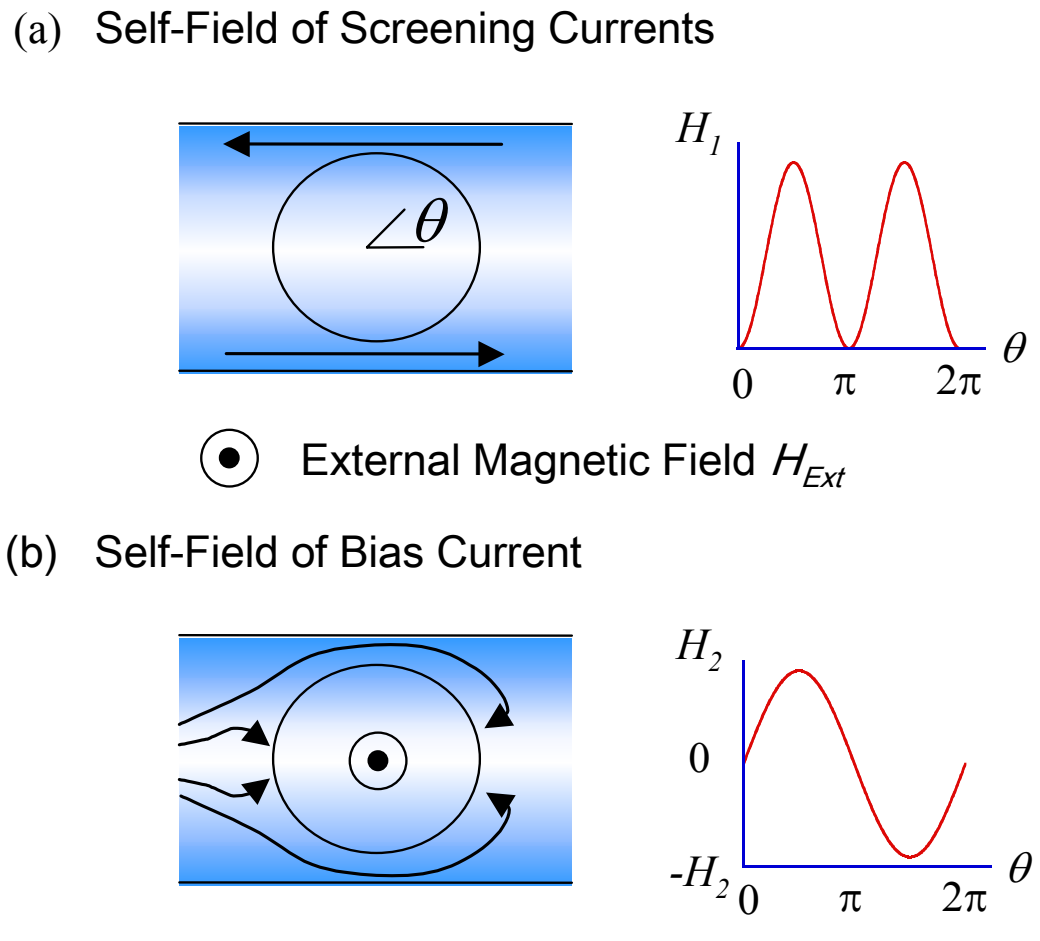

Figure 7.16: Fields perturbing the phase difference around the Corbino geometry juncion; (a) self-field of screening current and (b) self-field of bias current.

The phase difference induced due to the effective field $H(\theta)$ is given by:

$$\varphi(\theta) \propto \int_{\theta} H(\theta')d\theta' . \tag{7.4}$$

The overall critical current of the junction will hence be given by:

$$I_C = \int_0^{2\pi} J \sin\left(\varphi_0 + \varphi_1(\theta, H_{Ext}) + \varphi_2(\theta, I_C)\right)d\theta . \tag{7.5}$$

The phase difference due to the external field H_{Ext} is given by φ_1 and the phase difference due to the self field of the bias current is given by φ_2, which is therefore a function of the bias current and hence of I_C.

To remove the constant phase factor φ_0 we maximize I_C with respect to φ_0, arriving at:

$$I_C = \left(\langle C\rangle^2 + \langle S\rangle^2\right)^{1/2}, \tag{7.6}$$

where

$$\langle S\rangle = \int_0^{2\pi} J \sin(\varphi_1 + \varphi_2)d\theta , \tag{7.7}$$

$$\langle C\rangle = \int_0^{2\pi} J \cos(\varphi_1 + \varphi_2)d\theta . \tag{7.8}$$

As the right-hand side of Equation 7.6 is a function of I_C, in order to find the correct root we use the Newton-Raphson method (Jeffrey 1989). Figure 7.17 illustrates the root finding process as external field is increased (plots generated using Mathematica™). At zero external field there is one intersection: this is the correct value of I_C. As the external field increases a dip appears in the function I_C. Clearly at a certain value of external field a second solution will appear at $I_C = 0$.

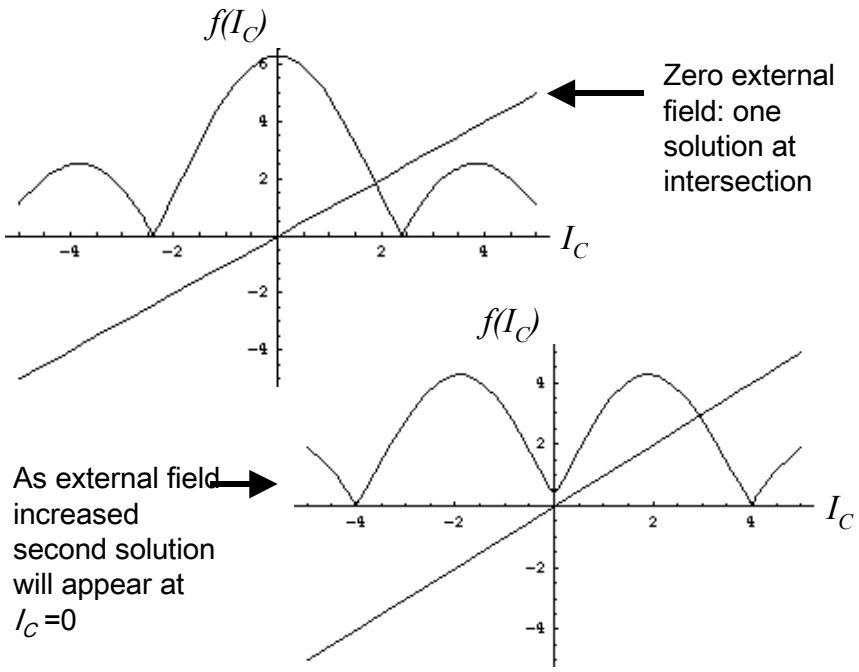

Figure 7.17: The root (solution for critical current I_C) for a particular value of external field H_{Ext} is found using the Newton-Raphson method.

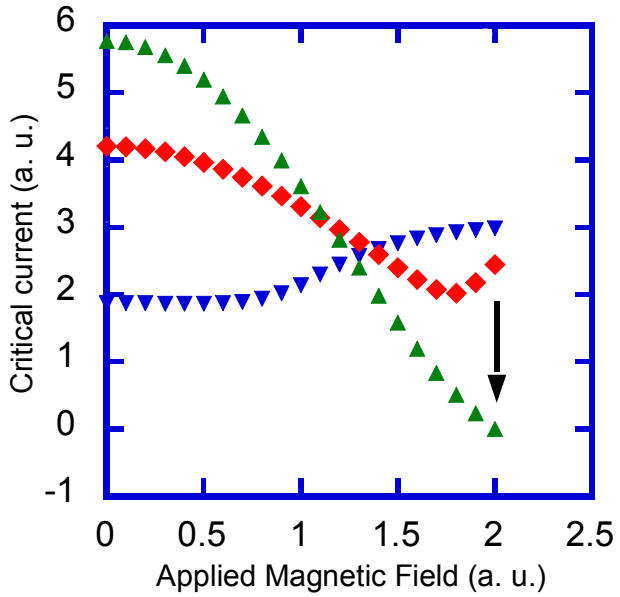

Figure 7.18: Simulated critical current response to external field. Scaling factor n=1 (inverted triangles), n=3.5 (diamonds), n=10(triangles). When the self-field of the bias current is taken into account (n=1, 3.5) a second solution abruptly appears at I_C=0. When the self-field of the bias current is small (n=10) a smooth suppression to I_C=0 is obtained. In all cases, an I_C=0 solution exists at an external field corresponding to one flux quantum, Φ_0 linking the junction.

The relative weights of the two field terms in the simulation can be varied. Qualitatively this results in the stretching or contraction of $f(I_C)$ along the x-axis. If the self-field of the bias-current is small then $f(I_C)$ will be stretched. This will lead to a smooth suppression of I_C to zero. If the self field of the bias current is dominant $f(I_C)$ is contracted, leading to several possible non-zero solutions. Figure 7.18 shows a selection of simulated $I_C(B)$ curves up to the point where an $I_C = 0$ solution appears. This model can also be adapted to take into account an asymmetric bias current (for example, where the circular barrier is not aligned perfectly on the axis of the track - a situation which did arise in some of the devices fabricated). In this case, in both experiment and simulation, current bias and external field direction have to be reversed to obtain the same magnitude of I_C.

This model shows that reversible field penetration leads to perturbations in I_C. In all cases explored an $I_C = 0$ solution exists at the same value of external field - this is interpreted as corresponding to the case where the total flux linking the junction is equal to one flux quantum. In my view this model is less satisfactory than that proposed in Section 7.3.2 as it does not take into account the *mechanism* of flux entry into the junction i.e. as individual vorticies. However, it is not without merit, as it does take the actual experimental geometry into account. In the experiments performed we typically did see reversible perturbations in I_C when sweeping over low field ranges, which can be attributed to reversible field penetration as described in this model. The irreversible suppression/reappearance of I_C seen at larger external fields in contrast can only be explained in terms of quantized flux entry/annihilation, which is best described using the model of 7.3.2.

7.3.4 Double well potential

The dependence of junction properties on the effective magnetic field distribution around the barrier considered in Section 7.3.3 has some interesting implications: consider a Corbino junction with trapped flux. (extent of vortex $\sim\lambda_J$, the Josephson penetration depth $<< 2\pi R$). With an external magnetic field, field energy is $\propto(H_1(\theta)+H_{Vortex})^2$. With external applied field the trapped flux will be located at $\theta = 0$ or π i.e. in double well potential. This seems to be a highly plausible scenario – Scanning Hall Probe studies of flux penetration in microscopic superconducting tracks typically show at low fields vortices neatly aligned along the track axis, as far from the edges as possible (e.g. Field 2002). The depth of the potential can be varied by the magnitude of the external field and, since λ_J is strongly temperature-dependent, the shape of the potential is modified by the temperature. If a bias current is applied through the junction the vortex can be driven between minima. It would be easy to couple a number of such systems together by writing a series of such circles along a superconducting track.

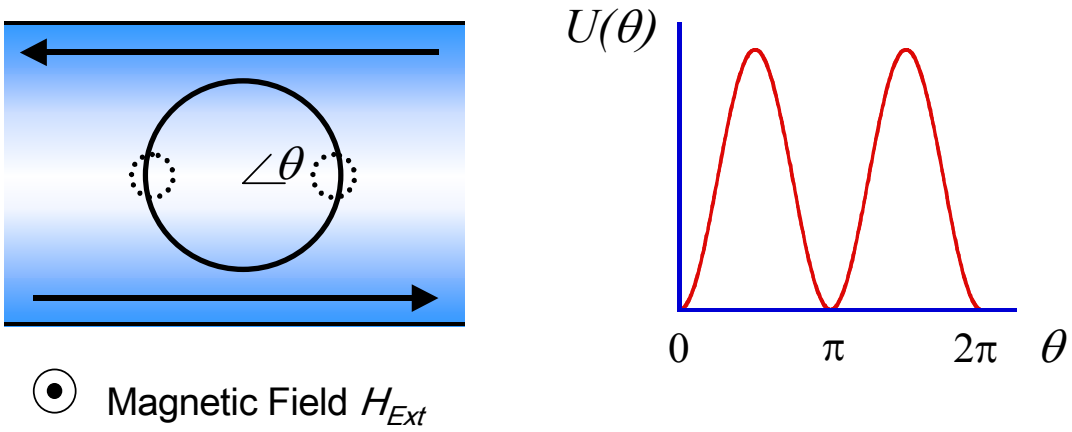

Figure 7.19: Double potential well. Consider a Corbino geometry junction with trapped flux. $T<<T_C$ so the flux vortex is confined (extent of vortex $\sim\lambda_J$, the Josephson penetration depth). With an external magnetic field, field energy is $\propto(H_1(\theta)+H_{Vortex})^2$ so potential energy takes the same form as $H_1(\theta)$ i.e. a double well potential. With external applied field the vortex is most likely to be located at $\theta = 0$ or π.

Double well potentials in heart-shaped annular junctions have been proposed as the basis of a qubit, the basic element of a quantum computer (Wallraff 2000). It is proposed that at sufficiently low temperatures, macroscopic quantum tunneling (Caldiera 1981) of fluxons will occur. In this case we have an overdamped SNS junction as opposed to an underdamped SIS junction (this implies a quality factor 10^6 smaller), which means quantum effects persist over impracticably short timescales and the trapped vortex behaves as a classical object. To raise the quality factor of our Corbino geometry junctions and enter the quantum regime we could employ in-plane SIS ramp junctions or planar high temperature superconductor junctions (Booij 1997).

7.3.5 Berry's phase effects

It has recently been pointed out (Section 2.6.2 - Gaitan 2001, Plerou 2001) that the appearance of a Berry phase as a vortex is driven around a circular junction barrier should lead to a disturbance of the current distribution and a variation in the driving force on the vortex. This should be expressed as a measurable variation in the *I-V* characteristics of the junction at low temperatures. Common annular SIS junctions are unsuited to this type of experiment because the geometry is incorrect. We have succeeded in creating a device in the ideal geometry. A further consideration is that a *clean* SNS barrier is required (coherence length in N layer longer than overall barrier width). At present our junctions are in the dirty limit (Hadfield 2001a). The use of epitaxial Nb-Cu bilayers would enable the fabrication of a clean limit Corbino geometry SNS junction (Section 6.4.2). Alternatively a ballistic N barrier could be achieved using a 2DEG (van Wees 1996).

7.4 Conclusion

The first Corbino geometry SNS junction has been successfully realized. The experimental work presented in this Chapter has focused primarily on measurement of critical current in response to an applied magnetic field at 4.2 K. As the junction barrier is embedded in a superconducting strip, magnetic flux can only enter as quantized units. A dynamic measurement of critical current as external field is varied reveals abrupt suppression/reappearance of critical current, corresponding to flux entry/annihilation in the junction barrier. When the superconducting region surrounding the barrier is sufficiently thin the suppression/reappearance occurs in a series of steps, suggesting incomplete flux quantization. The response of the junction I_C to the approach of an individual vortex has been simulated. In the near future we hope to study this exact situation experimentally by use of LTSEM (in collaboration with Professor Dieter Koelle at the Univerisity of Tübingen in Germany). A second model has been developed to take into account reversible magnetic field penetration in the actual device geometry. Using this approach it is possible to the critical current response of the junction to external field up to the point of irreversible flux entry into the barrier. These considerations indicate that a trapped vortex is confined in a double potential well in this device geometry. This work demonstrates that studies of this Josephson junction geometry are now technologically feasible. It is hoped that the publication of this work (Hadfield 2002b) will stimulate further experimental and theoretical studies.

Chapter 8: Conclusion

8.1 Outlook

In addition to the work on arrays and Corbino geometry junctions there are a number of other avenues my colleagues and I have pursued with our focused ion beam-based fabrication technique.

8.1.1 Junctions in magnesium diboride thin films

The long-overlooked compound magnesium diboride (MgB_2) was shown to superconduct at 39 K in early 2001 (Nagamatsu 2001). Tunneling studies indicate that MgB_2 is isotropic with an s-wave character, albeit with a double energy gap arising from multiband superconductivity (Pickett 2002). Josephson devices based on MgB_2 could potentially operate close to 30 K, well within the range of commercial cyrocoolers. In MgB_2, unlike the cuprate high temperature superconductors, grain boundaries do not give rise to weak links. Using 100 nm MgB_2 thin films from Korea (Moon 2001) my colleague Dr. Gavin Burnell has succeeded in fabricating the first thin-film MgB_2 Josephson junctions (Burnell 2001). As with the devices described in Chapters 5, 6 and 7 weak coupling was achieved by milling a 50 nm trench across a microscopic track. The junctions created are SNS type, with non-hysteretic RSJ-like current-voltage characterstics ($I_C R_N$ ~1 mV at 4.2 K) and strong microwave response (Figure 8.1), making these junctions excellent candidates for high frequency applications.

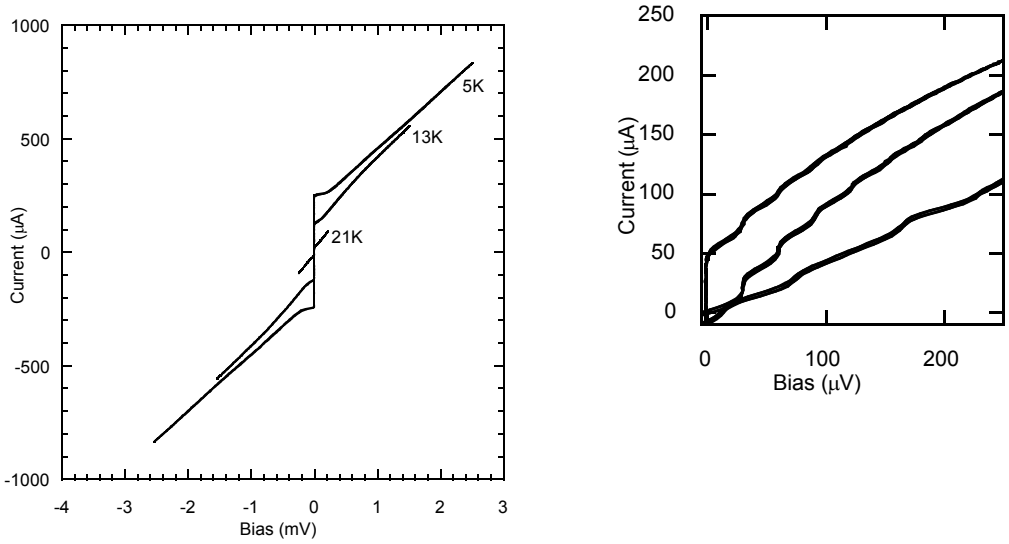

Figure 8.1: Current-voltage characteristic of a FIB junction in MgB_2 at 5, 13 and 21 K (left). Microwave response of junction at 5 K with increasing microwave power (right). (Burnell 2001b)

The first studies of MgB_2 SQUIDs (Blank 2001, Zhang 2001) suggest that due to the high flux pinning in this material, low noise SQUIDs for high temperature operation may be a real possibility. Thin film based dc SQUIDs fabricated by Dr. Burnell show an extremely large voltage modulation (up to 175 μV at 10 K - Burnell 2002b). Currently the limiting factor in making larger scale devices in MgB_2 is the quality of the available films (Zeng 2002). We have however already demonstrated that our existing junction technology is well-suited to the fabrication of SQUIDs and prototype Single Flux Quantum logic circuits (Ortlepp 2001) in this material.

8.1.2 The asymmetry modulated SQUID

One further technological application considered for superconductor-normal metal SNS bridge devices discussed in Chapter 5 is the Asymmetry Modulated SQUID or AMS (Tarte 2000). The common acronym SQUID stands for Superconducting QUantum Interference Device. The AMS is intended primarily for use as an X-ray detector. It is a development of the concept of a hot electron-tunable SNS junction (Baselmans 1999, 2001). In this case the N region of the SNS junction is attached to a larger normal metal reservoir. By altering the electron and phonon distributions in the reservoir the I_C of the junction can be modulated.

The AMS device is based on a dc SQUID - one junction barrier is attached to a normal metal reservoir (Figure 8.2). The two junctions are designed to have nominally equal I_C 's. The reservoir serves as an absorber for incoming high-energy particles. The arrival of an X-ray photon raises the temperature of the electron distribution in the reservoir, altering the I_C of the connected junction. The induced *asymmetry* between the I_C 's. of the two junctions in the SQUID loop leads to a circulating current and hence a magnetic flux Φ in the loop.

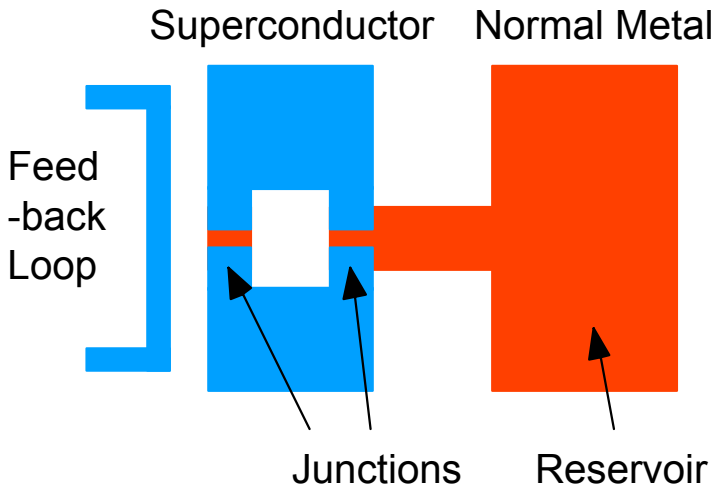

Figure 8.2: Schematic of the asymmetry modulated SQUID.

This in turn alters shape of the transfer function $V(\Phi)$ of the SQUID loop. The current in a feedback loop is used to apply an external flux which also modulates the current flow in the SQUID loop allowing the operating point to be set.

The AMS must be operated at low temperatures (in the region of 300 mK) in order to achieve the necessary decoupling of the electron and phonon distributions in the normal. The results in Chapter 5 indicate that the Nb-Cu bilayers are not necessarily the best choice for devices operating in this temperature regime (the critical current I_C saturates below 1 K and the *I-V* characteristics become hysteretic, plus a higher normal state resistance R_N is desirable for SQUID applications). Dr. Gavin Burnell has investigated devices in the alternative bilayer systems Nb-Al, TaNb-Cu and TaMo-Cu. Functioning dc SQUIDs based on this junction technology have been successfully fabricated (operating down to 2 K) and considerable progress has been made towards realizing the AMS concept (Burnell 2001a, 2002a).

8.1.3 A trilayer-based device fabrication technique

Recently my colleague Chris Bell has investigated the possibilities offered by the FIB for creating nanoscale sandwich-type device structures. This allows many of the problems usually associated with multilayer devices (such as poor interfaces) to be avoided. A similar FIB-based approach has been used with great success to fabricate structures for studies of intrinsic tunneling in single crystals of high temperature superconductor (Latyshev 1999). The basic fabrication strategy is as follows:

- The starting point is an *in situ* deposited trilayer structure, consisting of two thick electrodes (>100 nm) and a barrier layer (e.g. superconductor–normal metal-superconductor). The layers are deposited in sequence without breaking vacuum, ensuring excellent interface quality.

- A pattern of microscopic tracks is defined in the trilayer film, either by photolithography prior to deposition followed by lift-off, or photolithography and ion milling after deposition (see Chapter 3).

- Using the TEM sample preparation facility of the FIB (see Chapter 4) a small section of track (~1 micron long) is thinned to ~100 nm thickness on a high beam current (milling deep into the substrate on either side).

- The sample is then tilted on its side. The addition of a 45° wedge to the standard SEM stub allows the thinned track to be viewed almost sideways on. A small beam current (4 pA) is used to mill two slots as shown in the schematic Figure 8.3.

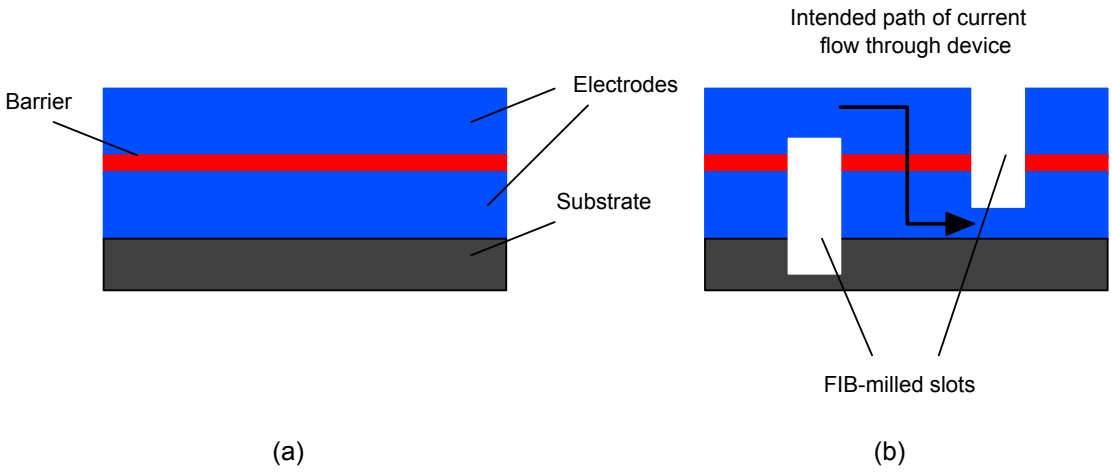

Figure 8.3: (a) Initial trilayer structure; (b) Thinned trilayer with FIB milled slots defining current path.

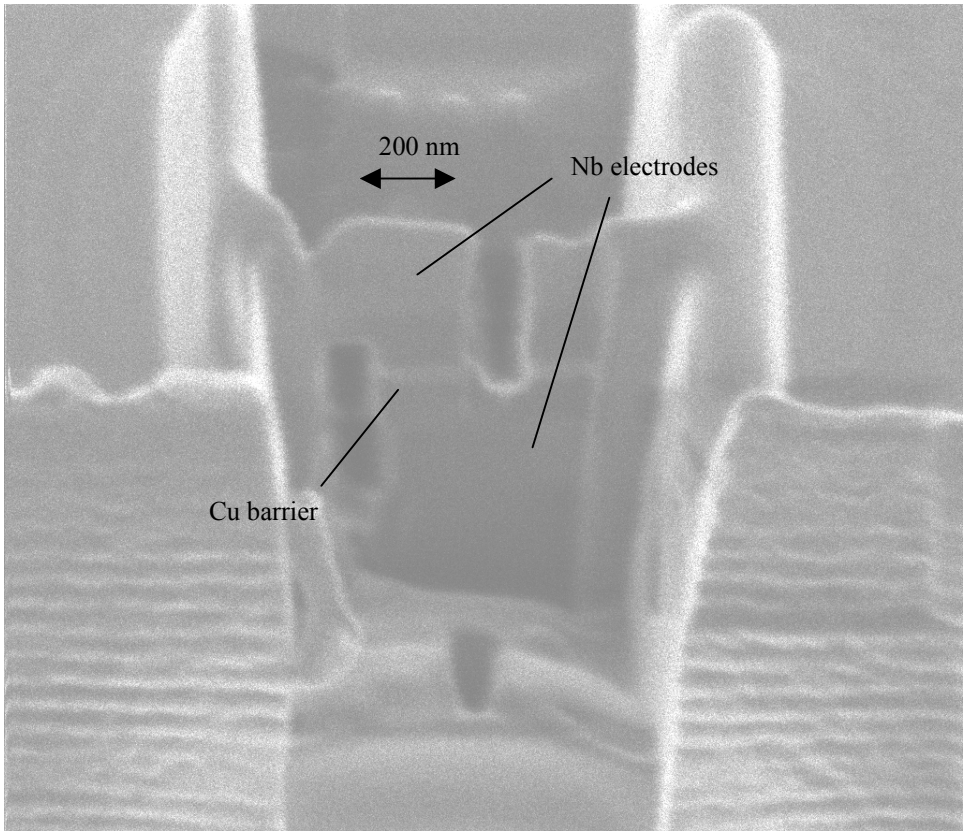

Figure 8.4: A finished trilayer device viewed at 45° tilt in the FIB

An image of a completed SNS device viewed at 45° tilt in the FIB fabricated in a Nb-Cu-Nb trilayer is shown in Figure 8.4. The Cu layer due to its high conductivity shows up as bright stripe between the Nb electrodes. The finished area of the junction is 100 nm x 200 nm.

We view this technique as being useful in fabricating individual test-devices in novel materials, rather than a means of fabricating large numbers of identical devices. In our laboratory we have the facility to deposit not only superconductors and normal metals, but also insulating barriers, ferromagnets, giant magnetoresistance (GMR) multilayers and maganite materials. We should soon also have the capability to deposit thin films the new superconductor MgB_2. This device structure could be used to realize a MgB_2 SIS junction (using MgO as a barrier). Other device configurations under consideration include SFS (π-junctions) that are of interest as a basis for quantum computing (Rayazanov 2000) and SIS junctions with magnetic impurities in the barrier (Bulaevskii 1977). An interesting possibility suggested by a number of theoreticians (Begeret, Golubov 2001) is a SFIFS structure: device behaviour depends strongly on whether the ferromagnetic layers are aligned parallel or antiparallel. The versatility of this technique extends beyond superconducting devices – we have also used this method to prototype blue LEDs in GaN heterostructures deposited by Metal-Organic Chemical Vapour Deposition (MOCVD) in our Department.

8.2.4 Long term outlook

In the longer term the outlook for focused ion beam based device work in Cambridge is very promising. 2003 will see the opening of a new Nanotechnology Centre in West Cambridge, reflecting the importance of this field in the future of science and technology (*Financial Times* 2001). The facilities will be shared between our research group (Device Materials, Materials Science) and the groups of Professor Richard Friend (Physics) and Professor Mark Welland (Engineering). In addition to extensive new cleanroom facilities there will be an expanded FIB suite. The FIB will applied to new areas such as bio-nanotechnology. The next generation of 'dualbeam' FIB systems feature both electron and Ga ion sources. The electron beam allows the progress of milling to be monitored without causing further implantation damage. The combination of a FIB system with a cold stage is a very interesting prospect for superconducting device fabrication. Furthermore the localized deposition of insulating materials will be possible. In the more distant future, FIB systems with lighter ion sources (H, Ar) may become commercially available. This would remove the current constraints on FIB applications which arise due to Ga implantation issues.

8.2 Conclusion

The body of work presented in this thesis demonstrates the usefulness and versatility of the focused ion beam (FIB) in superconducting device fabrication.

A single Josephson junction is fabricated in a superconductor-normal metal bilayer (125 nm Nb 75 nm Cu) by milling a 50 nm wide trench across a microscopic track. The resulting junctions are of superconductor-normal metal-superconductor (SNS) type. The depth of the trench and hence the resulting device parameters can be accurately controlled by means of an *in situ* resistance measurement. A thorough study has been carried out of the effect of the varying the normal metal layer thickness – the thickness is now optimized to achieve the slowest possible variation of device parameters with trench depth. The properties of single junction devices are well understood in the context of established SNS theory.

The junctions show promise for use in the next generation of Josephson voltage standards. The current-voltage characteristics are of resistively shunted junction type, with characteristic voltages of order 50 μV. Prototype series arrays of SNS junctions have been fabricated in collaboration with the U.S. National Institute of Standards and Technology (NIST). Phase-locking with an external microwave source has been achieved in 10-junction arrays between 4.2 K and the transition temperature. Low-noise measurements of the array differential resistance reveal a significant spread in junction critical currents; locking is achieved due to the shunting effect of the unbroken normal metal layer. Large-scale arrays require a significant reduction in device parameter spread. This may be achieved by using epitaxial films.

The FIB offers the opportunity to explore novel junction geometries. The first Corbino geometry SNS junction is reported. This device is fabricated by milling a *circular* trench in a bilayer track. An electrical contact is made to the central superconducting island, allowing a current to be passed radially through the device. As the junction is embedded in a superconducting track, when a magnetic field is applied flux can only enter the barrier in quantized units. Measurements of the device critical current reveal both flux entry and annihilation events. When the surrounding superconductor is sufficiently thin, flux entry in units of less than the flux quantum Φ_0 is observed. Numerical simulations have been carried out in support of these measurements. In the near future imaging work will be carried out in order to visualize the flux entry process. The possibilities of utilizing such a device to observe further novel quantum effects have been discussed.

8.0 Extensions to this Work

This section gives a summary of possible extensions to the work carried out in this thesis (more detailed discussion can be found in Chapters 6 and 7). Other FIB-based superconducting device fabrication work currently being carried out in our laboratory by my colleagues is summarized in Section 8.1.

The properties of planar SNS junctions fabricated by focused ion beam (FIB) are now well understood. The devices fabricated in Nb-Cu bilayers have the basic properties required for the next generation of Josephson Voltage Standards (non-hysteretic current-voltage characteristics, high current densities, low (~50 μV) characteristic voltage at 4.2 K and high potential integration density). The FIB-based technique offers sufficient reproducibility to allow functioning 10-junction arrays to be fabricated successfully. The final application requires up to 10,000 junctions; the current technique is considered too slow (10 s per junction) and the variation in device parameters too great. E-beam lithography and an anisotropic etch, in combination with the insertion of an etch-stop layer in the Nb could be used to create devices similar to those produced in this thesis – with benefit of much improved scalability. The fundamental cause of variation in device properties appears to be the polycrystalline microstructure of the thin films used. The use of epitaxial films may lead to a significant reduction in the device parameter spread. Attempts have been made in this thesis to achieve epitaxial Nb-Cu growth; an alternative deposition technique to sputtering, or a different choice of normal metal may lead to improved results. Furthermore, an alternative choice of normal metal may lead to high characteristic voltage junctions (~1 mV) which would then be of interest for other applications in superconducting digital electronics (RSFQ, SQUIDs).

The Corbino geometry Josephson junction reported in Chapter 7 undoubtedly merits further study. In the immediate future it would be of great interest to carry out an imaging experiment on the existing devices (Scanning Hall Probe, SQUID and LTSEM are suitable techniques). This would allow the movement of individual flux quanta to be visualized and correlated with electrical measurements. Underdamped Corbino geometry junctions could be fabricated by adding a capacitive shunt to the existing device structure, giving rise to propagating fluxon modes. Clean limit Corbino geometry SNS junctions (for example using a 2DEG as a normal metal layer) could be used to study Berry phase effects at low temperatures.

Appendix 1: Calculation of Δ*(x)* for a SN bilayer using Usadel theory

As discussed in Chapter 5, it would be very useful to able to calculate the form of the superconducting order parameter Δ for a superconductor-normal metal (SN) bilayer. This problem has already been dealt with in the limit close to T_C (Martinis 2000) using the Usadel microscopic theory (Usadel 1970).

The Usadel Equations

Usadel theory is based on the assumption that electronic transport in a metal is diffusive. The superconducting state is described by the function $\theta(x, E)$ where x is a position co-ordinate (the one-dimensional case is considered here for simplicity). The variable is complex and ranges in magnitude from 0 to π/2. $\theta=0$ corresponds to the normal state.

The Usadel equations used to solve for $\theta(x, E)$ are

$$\frac{\hbar D_S}{2}\frac{\partial^2\theta}{\partial x^2} + iE\sin\theta - \left[\frac{\hbar}{\tau_{sf}} + \frac{\hbar D_S}{2}\left(\frac{\partial\phi}{\partial x} + \frac{2e}{\hbar}A_x\right)^2\right]\cos\theta\sin\theta + \Delta(x)\cos\theta = 0 \qquad \text{(A.1)}$$

and

$$\Delta(x) = n_S V_{eff}\int_0^{\hbar\omega_D} dE\,\tanh\left(E/2k_BT\right)\mathrm{Im}\left[\sin\theta\right] \qquad \text{(A.2)}$$

where $D_S = \sigma_S / n_S e^2$ is the diffusivity constant, n_S is the density of states, σ_S is the normal state conductivity, V_{eff} the BCS-like interaction potential, τ_{sf} is the spin-flip time, ϕ is the superconducting phase, A_x is the vector potential, Δ is the superconducting order parameter, $\hbar\omega_D$ is the Debye energy and T is the temperature. The limit of a uniform superconductor we can neglect the first (spatial variation) and third (pair-breaking) terms in (A.1). θ is solved to be $\theta_{BCS}(E) = \arctan(i\Delta / E)$. Substituting θ_{BCS} into (A.2) gives the usual BCS form of the pair potential.

Solution Strategy

If pair breaking can be neglected (A.1) becomes

$$\frac{\hbar D_S}{2}\frac{\partial^2\theta}{\partial x^2} + iE\sin\theta + \Delta(x)\cos\theta = 0 \qquad \text{(A.3)}$$

The superconductor extends from x=-l_S to 0 and the normal metal extends from x=0 to l_N. We start with a trial solution for $\Delta(x)$ (a simple step function: Δ finite in the superconductor and Δ zero in the normal metal.

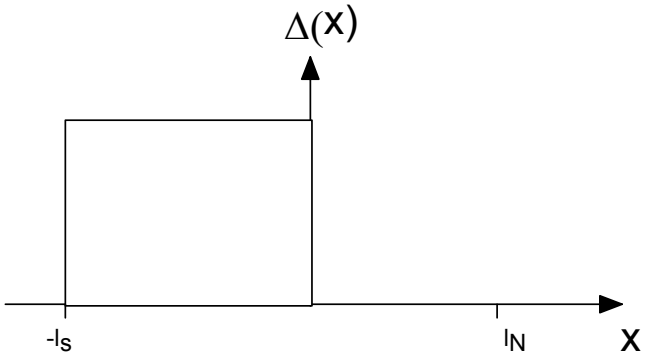

We substitute $\Delta(x)$ into (4) and find $\theta(x)$ by splitting θ into real and imaginary parts:

$\theta = A + iB$. The boundary conditions at x=-l_S and l_N are $\frac{\partial\theta}{\partial x} = 0$. At the superconductor-normal metal interface, current conservation requires that

$$\sigma_S\frac{\partial\theta_S}{\partial x} = \sigma_N\frac{\partial\theta_N}{\partial x} = \frac{G_{\text{int}}}{A}\sin(\theta_S - \theta_N) \qquad \text{(A.4)}$$

where S and N denote superconductor and normal metal respectively, and G_{int}/A is the electrical conductance of the interface per unit area.

Hence $\theta(x)$ will take the form

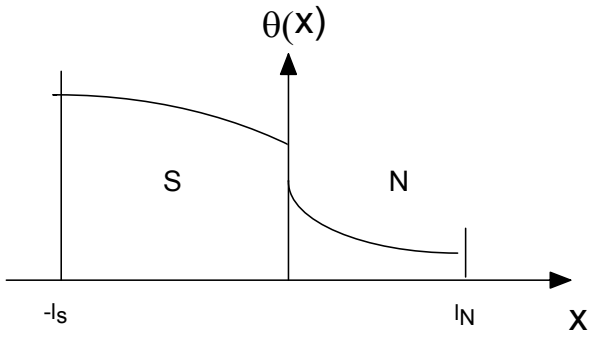

We repeat then solution of at intervals over range of energies E over which to integrate to find Δ (say $0<E<\hbar\omega_D$). The solutions $\theta(x, E)$ can then be used to solve the self-consistency equation (2) and obtain a new function $\Delta(x)$:

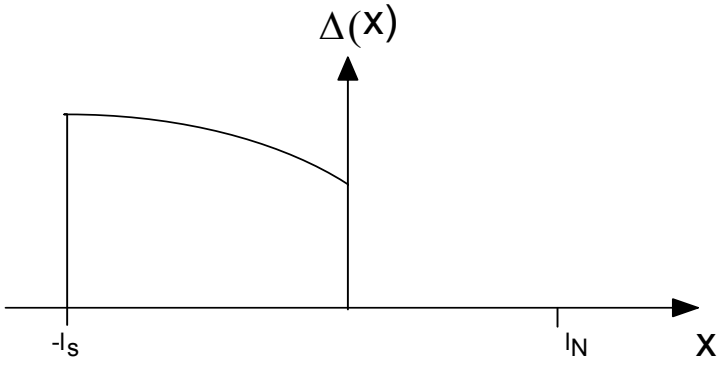

We then repeat the process using this as the input function until $\Delta(x)_{\text{old}}=\Delta(x)_{\text{new}}$.

Once the final form of $\theta(x, E)$ is known, useful quantities can be calculated. For example the quasiparticle density of states is given by $n_{qp} = n_S \,\mathrm{Re}\left[\cos\theta\right]$. The supercurrent density is given by

$$j_S = \left(\sigma_S / e\right)\left[\partial\phi/\partial x + \left(2e/\hbar\right)A_x\right]\int_{-\infty}^{+\infty} dE \tanh\left(E/2k_BT\right)\mathrm{Im}\left[\sin^2\theta\right] \qquad \text{(A.5)}$$

Now care must be taken as a supercurrent can act as a pair-breaker. If the supercurrent density is small (that is if the quadratic term inside the square bracket in (A.1) is much less than Δ) then

$$j_S \propto \Delta^2 \frac{\partial \phi}{\partial x} \tag{A.6}$$

Hence by calculating Δ*(x)* vertically through the centre of the device, the dependence of I_C and $I_C R_N$ on remaining Nb thickness, normal metal layer thickness and composition can be calculated.

Appendix 2: Scientific Meetings attended

EURESCO Conference 'Future Perspectives in Superconducting Josephson Devices' Pommersfelden, Germany, 29th June-4th July (Poster: The Corbino geometry Josephson junction).

Electromagnetic Technology Division, National Institute of Standards and Technology, Boulder, CO, USA, 5th June 2002 (Seminar: Josephson junctions fabricated by focused ion beam).

Beasley Group, Department of Applied Physics, Stanford University, CA, USA, 30th May 2002 (Seminar: Josephson junctions fabricated by focused ion beam)

Joint meeting of European Physical Society and Institute of Physics Condensed Matter and Materials Physics Division, Brighton U.K. 7th-11th April 2002 (Poster prize winner: The Corbino geometry Josephson junction).

Institute of Physics Superconductivity Group Workshop 'Mesoscopic Phenomena in Superconductors' University of Bristol, U.K., 26th September 2001 (Oral presentation: The Corbino geometry Josephson junction).

International Symposium on Superconducting Device Physics, 25-27 June 2001 Tokyo, Japan (Poster: Novel Josephson junction geometries in NbCu bilayer films fabricated by focused ion beam microscope).

International Superconductive Electronics Conference, 19-22 June 2001 Osaka, Japan, (Poster: Nanofabricated SNS junction series arrays in superconductor-normal metal bilayers).

Royal Microscopical Society Workshop: Advances in Focused Ion Beam Microscopy. University of Oxford, U.K., 30th March 2001.

Institute of Physics Superconductivity Group Meeting, March 2001, University of Birmingham, U.K. (Poster – runner up in Poster Competition).

Institute of Physics Condensed Matter and Materials Physics Meeting, 19-21 December 2000, University of Bristol, U.K. (Oral session SCd: Nanoscale SNS junction fabrication in superconductor-normal metal bilayers).

Applied Superconductivity Conference, 17-22 September 2000, Virginia Beach, VA, USA (Poster Session 5EC01: Nanoscale SNS junction fabrication in superconductor-normal metal bilayers).

Electromagnetic Technology Division, National Institute of Standards and Technology, Boulder, CO, USA, 10 July 2000 (Seminar: Nanoscale SNS junction fabrication in superconductor-normal metal bilayers).

Boulder School for Condensed Matter and Materials Physics, 3-28 July 2000, University of Colorado, Boulder, CO, USA. (Participant).

Institute of Physics Superconductivity Group Meeting, March 2000, University of Birmingham, U.K. (Poster).

COST-TMR Workshop on Mesoscopic Superconductors and Hybrid Structures, 16-19 December 1999, University of Lancaster, U.K.

Bibliography

Abrikosov A. A., *Zh. Eksp. Teor. Fiz.* **32** 1442 (1957);*Sov. Phys. JETP* **5** 1174 (1957)

Ambergaokar V., Halperin B. J. *Phys. Rev. Lett*. **22** 1364 (1969)

Anderson P. W., Rowell J. M. *Phys. Rev. Lett.* **10** 230 (1963)

Anderson P. W., Dayem A. H. *Phys. Rev. Lett.* **13** 195 (1964)

Andreev A. F., *Zh. Eksp. Teor.Fiz.* **46** 1823 (1964); *Sov. Phys. JETP* **19** 1228 (1964)

Ao P., Thouless D. J. 'Berry's phase and the Magnus force for a vortex line in a superconductor' *Phys. Rev. Lett.* **70** (14) 2158 (1993)

Arrington C. H., Deaver B. S. *Appl. Phys. Lett.* **26** 204 (1975)

Ashcroft N.W., Mermin N. D. *Solid State Physics,* Saunders College (1976)

Averin D. V. 'Solid state qubits under control' *Nature* **398** 748 (1999)

Barber Z. H., Ph.D. Thesis, University of Cambridge, U. K. (1986).

Bardeen J., Cooper L. N., Schrieffer J. R. *Phys. Rev.* **108** 1175 (1957)

Bardeen J. *Phys. Rev. Lett.* **7** 162 (1961)

Barone A. and Paterno G. *Physics and Applications of the Josephson Effect* Wiley and Sons, New York (1982)

Baselmans J. J. A., Morpurgo A. F., van Wees B. J., Klapwijk T. M., 'Reversing the direction of the supercurrent in a controllable Josephson junction' *Nature* **397** 43 (1999)

Baselmans J. J. A., van Wees B. J., Klapwijk T. M. 'Controllable π-SQUID' *Appl. Phys. Lett.* **79** (18) 2940 (2001)

Bean C. P., Livingstone J. D. *Phys. Rev. Lett.* **12** 14 (1964)

Bednorz J. G. , Müller K. A. *Z. Phys.* B **64** 189 (1986)

Bergeret F. S., Volkov A. F., Efetov K. B. 'Josephson current in superconductor-ferromagnet structures with a nonhomogeneous magnetization' cond-mat/0106510 (2001)

Bending S. J., Grigorenko A. N., Howells G. D., Humphreys R. G., Bekaert J., Van Bael M., Temst K., Van Look L., Moshchalkov V. V., Bruynseraede Y., Borghs G., 'Scanning Hall Probe Microscopy of Nanostructured Superconductors', *Physica C* **341-348**, 981 (2000).

Bell C., Dissertation for Certificate of Postgraduate Study, University of Cambridge, U.K. (2001)

Benz S. J., Burroughs C. J. 'Constant-voltage steps in arrays of Nb-PdAu-Nb Josephson Junctions' *IEEE Trans. Appl. Supercond.* **7** 2434 (1997)

Berry M. V. *Proc. R. Soc. Lond. A*, **392** 45 (1984)

Berry M. V. *Physics Today* **43** (12) 34 (1990)

Biersack J. P. 'SRIM 2000' computer program (1980)

Blachly M.A., Giordano N. *Phys. Rev. B* **49** 10 (1994)

Blamire M. G., Somekh R. E., Barber Z. H., Morris G. W., Evetts J. E. 'Microstructure Effects on Electronic Properties of Nb/Al_20_3/Nb Tunnel Junctions' *Journal of Applied Physics* **64** (11) 6396 (1988)

Booij W. E., Pauza A. J., Tarte E. J., Moore D. F., Blamire M. G. *Phys. Rev. B* **55** 14600 (1997)

Borovitskii S. I., Klushin A. M., Korotina T. B., Pariiskii A. E., Khorshev S. K., Shisharin P.A. *Sov. Tech. Phys. Lett.* **11** (6) 275 (1985)

Brandt E. H. 'The flux-line lattice in superconductors' *Rep. Prog. Phys.* **58** 1465 (1995)

Bulaevskii L. N., Kuzii V. V., Sobyanin A. A. *Pis'ma Zh. Eksp. Teor. Fiz.* **25** 7 314-318 (1977); *JETP Lett.* **25**, 7, 291 (1977)

Burnell G., Ph.D thesis, University of Cambridge, U. K. (1998)

Burnell G., Tarte E.J., Booij E. J., Blamire M. G., 'Niobium-copper superconductor-normal metal asymmetry modulated SQUIDs' *IEEE Trans. Appl. Supercon.* **11** 1 1243 (2001a)

Burnell G., Kang D.-J., Lee H. N., Moon S. H., Oh B., Blamire M. G. 'Planar Superconductor-Normal-Superconductor Junctions in MgB_2' *Appl. Phys. Lett.* **79** (21) 3464 (2001b)

Burnell G., Tarte E. J., Kang D.-J., Hadfield R. H., Blamire M. G., 'Asymmetry Modulated SQUIDs made by direct focused ion beam milling' *Physica C* **368** (1-4) 241 (2002a)

Burnell G., Kang D. J., Ansell D. A., Lee H. N., Moon S. H., Tarte E. J., Blamire M. G. 'Directly coupled superconducting quantum interference device magnetometer fabricated in magnesium diboride by focused ion beam' *Appl. Phys. Lett.* **81** (1) 102 (2002b)

Burnell G., Hadfield R.H., Bell C., Kang D.-J., Blamire M. G., 'Nanoscale Superconductor-Normal Metal-Superconductor Junctions fabricated by Focused Ion Beam' accepted for publication *Physica C* (2002c)

Caldiera A. O., Leggett A. *Phys.Rev. Lett.* **46** 211 (1981)

Cataliotti F. S., Burger S., Fort C., Maddaloni P., Minardi F., Trombettoni A., Smerzi A., Inguscio M. *Science* **293** 843 (2001)

Chaudari P., Mannhart J., Dimos D., Tsuei C. C., Chai J., Oprysko M. M., Scheuermann M. *Phys. Rev. Lett.* **60** 16 1653 (1988)

Cheishvili O. D. *Fizika Tverdogo Tela* **11** (1) 185 (1969); *Sov. Phys. Solid State,* **11** (1) 138 (1969)

Clarke J. *Proc. Roy. Soc. LondonA* **308** 447 (1969); *Phys. Rev.* **B4** 2963 (1971)

Clem J. R. unpublished (1998)

Corbino O. M., *Nuovo Cim.* 1, 397 (1911); *Phys. Zeit.* 12 561 (1911)

Daniel J. H., Moore D. F., 'A microaccelerometer structure fabricatied in silicon-on-insulator using a focused ion beam process' *Sensors and Actuators A* **73** (3) 201 (1999)

Davidson A., Dueholm B., Kryger B., Pedersen N. F. *Phys. Rev. Lett.* **55** 2059 (1985)

Davis J. C., Packard R. E. 'Superfluid ^{3}He Josephson weak links' *Rev. Mod. Phys.* **74** 741 (2002)

Deaver B. S., Fairbank W. M. *Phys. Rev. Lett*. **7** 43 (1961)

de Gennes P. G. *Rev. Mod. Phys.* **36** 225 (1964)

Delin K. A., Kleinsasser A. W. 'Stationary properties of high-critical-temperature proximity effect Josephson junctions' *Supercond. Sci. Technol.* **9** 227 (1996)

de Lozanne A. L., Beasley M. R. 'Time-Dependent Superconductivity in SNS Bridges: AN Example of TDGL Theory' in *Nonequilibrium Superconductivity* ed. Langenberg D.N., Larkin A. I., Elsevier (1986)

Deutscher G. and de Gennes P. G. *'Superconductivity'* vol 2 ed R. D. Parks New York: Marcel Dekker (1969)

Doll R., Näbauer M., *Phys. Rev. Lett*. **7** 51 (1961)

Dubos P.'Transport électronique dans des nanojonctions supraconducteur-métal normal-supraconducteur', Doctoral Thesis, Université Joseph Fourier, France (2000)

Dubos P., Courtois H., Pannetier B., Wilhelm F. K., Zaikin A. D., Schön G., *Phys. Rev. B* 63 64502 (2001a)

Dubos P., Courtois H., Buisson O., Pannetier B, 'Coherent low-energy charge transport in a diffusive SNS junction', *Phys. Rev. Lett.* **87** (20) 206801 (2001b)

Eilenberger G. *Z. Phys.* **241** 195 (1968)

Feynman R. P., Leighton R. B., Sands M., *The Feynman Lectures on Physics,* Vol. III Adison-Wesley, Reading, Massachusetts, (1965)

Field S., Martinis J. M. unpublished (2002)

Financial Times, London, June 15th 2001 National News 'Nanometre research receives £18 m boost'. (2001); see also http://www-g.eng.cam.ac.uk/nano/news_irc.htm

Fischer G. M., Mayer B., Schulze H., Gross R. *IEEE Trans. Appl. Supercond.* **5** (2) 2184 (1995)

Fiske M. D. *Rev. Mod. Phys.* **36** 221 (1964)

Fulton T. A., Dynes R. C. *Solid State Communications* 12 57 (1973)

Galaver J. R. *Appl. Phys. Lett.* 23, 480 (1973)

Gaitan F. *Phys. Rev. B* **51** (14) 9051 (1995)

Gaitan F., Shenoy S. R. *Phys. Rev. Lett.* **76** (23) 4404 (1996)

Gaitan F. *Phys. Rev. B* **63** 104511 (2001)

Gau L., Xue Y. Y., Chen F., Xiong Q., Meng R. L., Ramierez D., Chu C. W., Eggert J. H., Mao H. K. *Phys. Rev. B.* **50** 4260 (1994)

Geerk J., Gurvitch M., McWahn D. B., Rowell J. M., *Physica* **109** 1775 (1982)

Geim A. K., Dubonos S. V., Grigorieva I. V., Novoselov K. S., Peeters F. M., Schweigert V. A. 'Non-quantized penetration of magnetic field in the vortex state of superconductors' *Nature* **407** 7 September 2000 55-57 (2000)

Ginzburg V. L., Landau L. D. *Zh. Eksp. Teor. Fiz* (in Russian) **20** 1064 (1950)

Ginzburg V. L. *Sov. Phys. JETP* **15** 207 (1962)

Ginzburg V. L. *Physics-Uspekhi* (in English) **43** (6) 573 (2000)

Giovanazzi S., Semerzi A., Fantoni S. *Phys. Rev. Lett.* **84** 20 4521 (2000)

Goldobin E., Wallraff A., Thyssen N., Ustinov A. V. *Phys. Rev. B* **57** 130 (1998)

Golubov A. 'Critical current in SFIFS junctions' *JETP Lett.* **75** (4) 190 (2002)

Gor'kov L. P., *Sov. Phys. JETP*, **36** 1364-1367 (1958a)

Gor'kov L.P. *Sov. Phys. JETP* **7** 505 (1958b)

(1934); *Z. Techn. Phys* **15** 539 (1934)

Gor'kov L. P. *Sov. Phys. JETP* **10** 998 (1960)

Gor'kov L. P., Eliashberg G. M. *Sov. Phys. JETP* **27** 328 (1968)

Gorter C. J. and Casimir H. B. G. *Phys. Z.* **35** 963 Ambergaokar V, Baratoff A *Phys. Rev. Lett.* **10** 486 (1963) Erratum **11** 104

Gross R., Koelle D. *Rep. Prog. Phys.* **57** 651 (1994)

Gubankov V. N., Koshelets V. P. Likharev K. K., Ovsyannikov G. A. *JETP Lett*. **18** 292 (1973)

Hadfield R. H., Burnell G., Booij W. E., Lloyd S. J., Moseley R. W., Blamire M. G. 'Nanoscale SNS junction fabrication in superconductor-normal metal bilayers' *IEEE Trans. Applied Superconductivity* **11** 1 1126-1129 (2001a)

Hadfield R. H., Burnell G., Blamire M. G., Dresselhaus P., Benz S. P., 'Nanofabricated SNS junction series arrays in superconductor-normal metal bilayers', *Superconductor Science & Technology* **14** (12) 1086 (2001b)

Hadfield R. H., Burnell G., Grimes P., Kang D.-J., Blamire M. G.'Novel Josephson junction geometries in NbCu bilayers fabricated by focused ion beam microscope', *Physica C* **367** (1-4) 267 (2002a)

Hadfield R. H., Burnell G., Kang D. -J., Bell C., Blamire M. G. 'The Corbino geometry Josephson junction' submitted to *Phys. Rev. B* (2002b)

Hamilton C. A. 'Voltage-standard devices' in the *Concise Encyclopedia of Magnetic and Superconducting Materials* ed. Evetts J. E., Pergamon, Oxford (1992)

Hamilton C. A. *IEEE Trans. Appl. Superond*. **7** 3759 (1997)

Hauser J. J., Theuerer H. C., Werthamer N. R. *Physical Review* **142** 1 (1966)

Irmer B., Simmel F., Blick R. H., Lorenz H., Kotthaus J. P., Bichler M., Wegscheider W. 'Nano-ploughed Josephson Junctions as on-chip radiation sources*' Superlattices and Microstructures* **25** (5/6) 785 (1999)

Isaac S. P., Ph.D thesis, University of Cambridge, U. K. (1998)

Jain A. K., Lukens J. E., Tsai J. S. 'Test for relativistic gravitational effects on charged particles' *Phys. Rev. Lett.*, **58** 1165 (1987).

Jeffrey A. 'Mathermatics for Engineers and Scientists' Van Nostrand Reinhold 4th Edition (1989)

Josephson B. D., *Physics Letters* **1** 251 (1962)

Kang D. -J, Burnell G., Lloyd S. J., Speaks R. S., Peng N. H., Jeynes C., Webb R., Yun J. H., Moon S. H., Oh B., Tarte E. J., Moore D. F., Blamire M. G. *Appl. Phys. Lett.* **80** (5) 814 (2002)

Kanvoussanakli E., Monaco R., Rivers R. J. *Phys. Rev. Lett.* **85** (16) 3452 (2000)

Kempshall B. W., Schwarz S. M., Prenitzer B. I., Giannuzzi L. A., Irwin R. B., Stevie F. A. 'Ion channelling effects on the focused ion beam milling of Cu' *J. Vac. Sci. Technol. B* **19** (3) (2001)

Keyes R. W. 'Physics of digital devices', *Rev. Mod. Phys.* **61** 2 279 (1989)

Kleiner R., Steinmeyer F., Kunkel G., Mueller P. *Phys. Rev. Lett.* **68** 2394 (1992)

Kleiner R. *Phys. Rev. B* **50** 6919 (1994)

Klushin A. M., Prusseit W., Sodtke E., Borovitskii S. I., Amatuni L. E., Kohlstedt H. 'Shunted bicrystal Josephson junction arrays for voltage standards' *Appl. Phys. Lett*. **69** 1634 (1996)

Klushin A. M. 'High Temperature Superconducting Josephson Junction Arrays for a Voltage Calibrator' Proc. International Superconductive Electronics Conference, Osaka, Japan (2001)

Kogan V. G. 'Pearl's vortex near the film edge' *Phys. Rev. B* **49** 22 15874 (1994)

Kose, V. 'Recent advances in Josephson voltage standards' *IEEE Trans. Instr. Meas*. IM-**25** 483 (1976)

Kulik I. O. and Omel'yanchuk A. N. *JETP Lett.* **21** 96 (1975)

Kulik I. O. and Omel'yanchuk A. N. *Sov. J. Low Temp. Phys.* **4** 142 (1978)

Kurprianov M. Yu, Likharev K. K., Lukichev V. F. *Physica* 108B 1001 (1981)

Kurprianov M. Yu, Lukichev V. F., *Sov. Phys. JETP* **67** (6) 1163 (1987)

Kuwada M., Onodera Y., Sawada Y. *Phys. Rev. B* **27** (9) 5486 (1983)

Latif A., Booij W. E., Durrell J. H., Blamire M. G. 'Real time resistometric depth monitoring in the focused ion beam' *J. Vac. Sci. Technol*. B **18** (2) (2000)

Latyshev Yu. I., Kim S. –J., Yamashita T., 'Fabrication of submicron BSCCO stacked junctions by focused ion beam (FIB)' *IEEE Trans. Appl. Supercond*., **9** 4312 (1999)

Laub A., Doderer T., Lachenmann S. G., Huebner R. P., Niemeyer J., Oboznov V. A. *Phys. Rev. Lett.* **75** 1372 (1995)

Lempitskii S. V., *Sov. Phys. JETP* 58 (3) 624 (1983)

Likharev K. K . *Sov. Tech. Phys. Lett.* **2** 12 (1976)

Likharev K. K. *Rev. Mod. Phys.* **51** 101 (1979)

Likharev K. K. '*Dynamics of Josephson junctions and circuits'* Gordon and Breach (1986)

Likharev K. K. and Semenov V. K. 'RSFQ logic/memory family: a new Josephson junction technology for sub-teraherz-clock-frequency digital systems' *IEEE Trans. Appl. Supercond.* **1** 1 3 (1991)

Likharev K. K. 'Superconductor Devices for Ultrafast Computing' in *Applications of Superconductivity* ed. Weinstock H. Kluwer, Dordrecht, (1999)

Lindelof P. E. *Rep. Prog. Phys***. 44** 949 (1981)

Little W. A., Parks R. A., *Phys. Rev. Lett*. **9** 9 (1962), *Phys. Rev.* **133** A97 (1964)

London F., London H. *Proc. R. Soc.* A **149** 71 (1935)

London F. *Superfluids* Wiley, New York (1950)

Loram J. E., Whall T. E., Ford P. J. *Phys. Rev. B* **2** 4 857 (1970)

Makhiln Yu. G., Volovik G. E. 'Spectral flow in Josephson junctions and effective Magnus force' *JETP Letters* **62** (12) 941 (1995)

Makhlin Yu. G., Schön G., Shnirman A., 'Quantum-state engineering with Josephson-junction devices' *Rev. Mod. Phys.* **73** 357 (2001)

Martinis J. M., Hilton G. C., Irwin K.D., Wollman D. A., *Nuclear Instruments and Methods in Physics Research A* 444 23-27 (2000).

McCumber D. E. *J. Appl. Phys.* **39** 3113 (1968)

McLaughlin D. W., Scott A. C. *Phys. Rev. A* **18** 1652 (1978)

Melngailis J. 'Critical review: focused ion beam technology and applications' *J. Vac. Sci. Technol. B* **5** 469 (1987)

Meissner W., *Z. Ges. Kältenindustr.* **34** 197 (1927)

Milner R. G., Arias A.C., Stevenson R., Mackenzie J. D., Richards D., Friend R. H., Kang D-J., Blamire M. G. *Mat. Sci.and Technol.* **18** 759 (2002)

Moseley R. W., Booij W. E., Tarte E. J. Blamire M. G. 'Direct writing of low Tc superconductor-normal metal-superconductor junctions using a focused ion beam' *Appl. Phys. Lett*., **75** 262 (1999)

Moseley R.W.,'Focused ion beam fabricated non-equilibrium superconducting devices' PhD thesis, University of Cambridge, U.K. (2000)

Nagamatsu, J., Nakagawa, N., Muranaka, T., Zentitani, Y., Akimitsu, J. 'Superconductivity at 39 K in magnesium diboride' *Nature* **410** 63 (2001)

Nakamura Y., Pashkin Yu. A., Tsai J. S. 'Coherent control of macroscopic states in a single-Cooper pair box' *Nature* **398** 786 (1999)

Nappi C., Cristiano R. *Appl. Phys. Lett.* **70** 1320 (1997)

Nappi C., Cristiano R., Lissitski M. P., Monaco R., Barone A. *Physica C* **367** 241 (2002)

Niemeyer J., von Minnigerode G., Z. *Physik B* **36** 57-66 (1979)

Niemeyer J. 'Josephson arrays for dc and ac metrology' *Supercond. Sci. Technol.* **13** 546 (2000)

Notarys H. A., Mercereau J. E. *J. Appl. Phys*. **44** 4 1821 (1973)

Ohring M., *The Materials Science of Thin Films*, Academic Press (1992)

Onnes H. K., *Commun. Phys. Lab. Univ. Leiden* No 124c (1911)

Ortlepp T., Toepfer H., Uhlmann H. F., *Supercond. Sci. Technol.* **14** L37 (2001)

Owen C. S., Scalapino D. J. *Phys. Rev.* **164** 538 (1967)

Rosenthal P. A., Beasley M. R., Char K., Colclough M. S., Zaharchuk G., 'Flux focusing effects in planar thin-film grain boundary Josephson junctions', *App. Phys. Lett.* **59** (26) 3482 (1991)

Pauza A. J. 'Fabrication of Josephson junctions with an electron beam' Ph.D. thesis, University of Cambridge, U.K. (1993)

Pearl J. *App. Phys. Lett.* **5** 65 (1964)

Phaneuf M. W. 'Applications of focused ion beam microscopy to materials science specimens' *Micron* **30** (3) 277 (1999)

Pickett W. *Nature* **418** 733 (2002)

Pippard A. B. *Proc. R.. Soc. Lond. A* **216**, 547 (1953)

Plerou V., Gaitan F. *Phys. Rev. B* **63** 104512 (2001)

Poole C. P. (Ed.) *Handbook of Superconductivity* Academic Press, San Diego (2000)

Reyntjens S., Puers R. 'A review of focused ion beam applications in microsystem technology' *J. Micromech. Microeng.* **11** 287 (2001)

Rowell J. M. 'Superconducting thin films, multilayers and devices ' in the *Concise Encyclopedia of Magnetic and Superconducting Materials* ed. Evetts J. E., Pergamon, Oxford (1992)

Ryazanov V. V., Oboznov V. A., Rusanov A. Yu., Veretennikov A. V., Golubov A. A., Aarts J. 'Coupling of two superconductors through a ferromagnet: evidence for a π-junction' *Phys. Rev. Lett.* **86** (11) 2427 (2001)

Schilling A., Catoni M., Jeandupeux O., Cumo J. D., Ott H. R., Rossel C. *Physica C* 235 (1994)

Schneider C. W., Ph.D thesis, University of Cambridge, U. K. (1994)

Schrieffer J. R. *Theory of Superconductivity* (Revised printing, 1993) Addison-Wesley

Schrieffer J. R., Tinkham M. *Rev. Mod. Phys.* **71** 2 S313 (1999)

Shapere A., Wilczek F., eds. *Geometric Phases in Physics* World Scientific, Singapore (1989)

Shapiro S., *Phys. Rev. Letters* **11**, 80 (1963)

Sherrill M. D., Bhushan M. *Phys. Rev. B* **19** (3) 1463 (1979)

Sherrill M. D. *Phys. Lett. A* **82A** (4) 191 (1981)

Skocpol W.J., Beasley M. R., Tinkham M. *J. Appl. Phys.* **45** 4054 (1974)

Stewart W. C. *Appl. Phys. Lett.* **12** 277 (1968)

Tarte E. J., Moseley R. J., Kölbl M. R., Booij W. E., Burnell G., Blamire M. G. 'Asymmetry Modulated SQUIDs' *Supecond. Sci. Technol.* **13** 1 (2000)

Terpstra D., PhD thesis, University of Twente, NL (1994)

Tilley D. R. *Physics Letters* **20** (2) 117 (1966)

Tilley D. R. and Tilley J. *Superfluidity and Superconductivity* 3rd Edition, Institute of Physics, Bristol (1990)

Tinkham 'Effect of fluxoid quantization on transitions of superconducting films', *Phys. Rev.* **129** 2413 (1963)

Tinkham M., *Introduction to Superconductivity* 2nd Ed. *McGraw-Hill* (1996)

Usadel K. D. *Phys. Rev. Lett.* **25** 507 (1970)

Ustinov A.V., Doderer T., Mayer B., Huebener R. P., Golubov A. A., and Oboznov V. A. 'Experimental study of the interaction of fluxons with an Abrikosov vortex in a long Josephson junction'*Phys. Rev. B* **47**, 944 (1993)

Ustinov A. V. *Physica D* 'Solitons in Josephson junctions' **123** 315 (1998)

Ustinov A. V. *Appl. Phys. Lett.* 'Fluxon insertion into annular Josephson junctions' **80** 17 3153 (2002)

van Dover R. B., de Lozanne A., Beasley M. R., *J. Appl. Phys.* **52** 12 7327 (1981)

van Duzer T., Turner C. W. *Principles of Superconductive Devices and Circuits* 2nd Ed. Prentice Hall (1999)

van Wees B., *Physics World* **41** (1996)

Vinen W. F. *Proc. R. Soc. A* **260** 218 (1961)

Vinen W. F. 'The properties of superconductor and superfluid helium' in *Superconductivity* ed. Parks R. D., Marcel Dekker, New York (1969)

Waldram J. R., Pippard A. B., Clarke J., *Phil. Trans. Roy. Soc. Lond. A.* **268** 265-287 (1970)

Waldram J. R. *Superconductivity in Metals and Cuprates* IOP Publishing (1996)

Wallraff A., Ustinov A. V., Kurin V. V., Shereshevshy I. A., Vdovicheva N. K., *Phys. Rev. Lett.* 'Whispering Vortices' **84** 151 (2000a)

Wallraff A., Koval Yu., Levitchev M., Fistul M. V., Ustinov A. V., 'Annular long Josephson junctions in a magnetic field: engineering and probing the fluxon interaction potential', Journal of Low Temperature Physics, Vol. 118, Nos 5/6 543 (2000b)

Wallraff A. *Fluxon Dynamics in Annular Josephson Junctions* Doctoral Thesis, Friedrich-Alexander University, Erlangen-Nuremburg, Germany (2001)

Wang H. B., Wu P. H., Chen J., Maeda K., Yamashita T. *Appl. Phys. Lett.* **80** 9 1604 (2002)

Warburton P. A. 'Quasiparticle trapping in superconducting hetrostructures 'Ph.D thesis, University of Cambridge, 1993

Weber C. 'Phasensynchonisation von Hochtemperatur-Josephson-Kontakten mit Parallelwiderständen unter Mikrowelleneinstralung' Doctoral Thesis, Forschungszentrum Jűlich, Germany (2000)

Wilhelm F. K., Schön G., Zaikin A.D., Golubov A. A., Dubos P., Courtois H., Pannetier B., *Physica B* **284-288** 1836 (2000).

Winkler D., Mros N., Tarte E. J., Yurgens A., Kransnov V. M., Foord D. T., Booij W. E., Blamire M. G. 'Intrinsic Josephson effects in submicrometre Bi2212 mesas fabricated using focused ion beam etching' *Supercond. Sci. Technol.* **12** (1999) 1013-1015

Young R. J. 'Micro-machining using a focused ion beam' *Vacuum* **44** 353 (1993)

Zeng X. *et al* '*in situ* epitaxial MgB2 thin films for superconducting electronics' Nature Materials **1** 35 (2002) – see also commentary by Rowell J. *ibid.*

Zhang Y., Kinion D., Chen J., Hinks D. G., Crabtree G. W., Clarke J. 'MgB2 tunnel junctions and 19 K low-noise dc superconducting quantum interference devices' *App. Phys. Lett.* **79** (24) 3995 (2001)

Zimmerman J. E, Silver A.H. *Phys. Lett* 10 47 (1964)

Zurek W. H. *Phys. Rep.* **276** (4) 177 (1996)